DISSERTATION

INVESTIGATING GROUP-V DOPING LIMITS IN CdSeTe AND POTENTIAL APPLICATION OF CdSe AS TANDEM TOP-CELLS

Submitted by

Taylor Hill

School of Material Sciences and Engineering

In partial fulfillment of the requirements

For the Degree of Doctor of Philosophy

Colorado State University

Fort Collins, Colorado

Summer 2025

Doctoral Committee:

Advisor: James Sites

Walajabad Sampath
Amit Munshi
Justin Sambur
Angus Rockett

ABSTRACT

INVESTIGATING GROUP-V DOPING LIMITS IN CdSeTe AND POTENTIAL APPLICATION OF CdSe AS TANDEM TOP-CELLS

Cadmium selenium tellurium alloys ($CdSe_XTe_{(1-X)}$ known as CST) are a photovoltaic specialist's dream: with ideal single-junction and tandem top-cell bandgaps (based on Se stoichiometry) and large absorption coefficient for all stoichiometries (enabling thin-film applications), CST continues to be a promising material for photovoltaic applications. However, CST is not without its problems. Record efficiency CST devices have demonstrated short-circuit current density (J_{SC}) and fill factor (FF) near their theoretical maximum based on measured bandgaps, but continued improvements to device performance has been limited by the open-circuit voltage (V_{OC}), which has been less than 900mV (< 80% of theoretical maximum) for nearly a decade. Advances in absorber doping for p-type conversion have enabled increased carrier densities, moving from roughly 10^{14} cm^{-3} with group-I doping (copper) to 10^{16} cm^{-3} using group-V doping (arsenic or phosphorus), but increases in V_{OC} have not been reflected by this fact. This is typically attributed to the so-called "dopant activation" problem, which accounts for the density of acceptor states provided per density of dopant incorporated and tends to be less than 10% in polycrystalline CST. This indicates that roughly 9 out of 10 dopant atoms form defects which may compensate p-type conversion and additionally hinder device performance. Meanwhile, the use of Se alloying to reducing the effective absorber bandgap has afforded increased J_{SC}, but the roles in which Se and group-V dopants play in conjunction with typical device processing is not widely appreciated.

In this work, the modern advancements which have allowed for record efficiency CdTe based devices, namely the incorporation of group-V dopants and Se alloying, are examined to address misunderstandings and provide a framework for improving device processing. An investigation into the impact of group-V dopant concentration in CST using optimized device processing con-

ditions reveals that the density of acceptors formed by group-V doping tends to plateau at a point (roughly 1-5 X 10^{16} cm^{-3}) and further incorporation of dopants tends to reduce device performance through increased radiative recombination. Evaluation of a novel process to increase group-V dopant activation, thereby reducing the concentration of nonactive dopant defects, is presented by use of ion implanted oxygen getters. The presence of oxygen in CST devices is inevitable and an oxidated dopant is effectively an inactive dopant. By implanting elements which have a higher affinity for oxidation relative to dopant atoms, the formation of dopant oxides is reduced, and an increased dopant activation is demonstrated. However, this did not improve device performance in practice, indicating that while the methodology of reducing group-V oxides can increase activation, the process of ion implantation itself may introduce additional lattice defects which negate the increased dopant activation. This leads to an examination of the role Se plays in intrinsic CST absorbers independent of group-V doping, revealing an unexpected n-type intrinsic conductivity, which may be a source of defects which compensate the use of group-V dopants. This indicates that work must be done to carefully balance the distribution of Se throughout the absorber bulk, where a concentration gradient, rather than a uniform ternary stoichiometry, is shown to enable the best performance.

Finally, pure CdSe absorbers with a large bandgap of roughly 1.7 eV are examined for potential application in tandem PV devices. CdSe absorbers grown at CSU demonstrate the requisite large bandgap and provide insight into limitations based on absorber thickness. This leads to a discussion on CdSe devices with record V_{OC}. To date, published record efficiency CdSe devices have shown $>$80% of theoretical short circuit current (J_{SC}/J_{SC}^{SQ}) and $>$60% of theoretical fill factor (FF/FF_{SQ}). However, such record devices have achieved $<$50% of the theoretical open circuit voltage (V_{OC}/V_{OC}^{SQ}). The development of CdSe devices using novel transport and contact layer structures involving organic semiconductors and transition metal oxides to achieve $>$60% of V_{OC}^{SQ} (V_{OC} $>$900 mV) is presented. The limitations of CdSe absorbers are addressed through temperature and intensity dependent photoluminescence measurements, indicating that low charge mobility due to intrinsic trap states in CdSe bulk are the primary limiting factor to further increasing V_{OC}.

ACKNOWLEDGEMENTS

I would like to thank my advisor, Professor James Sites, for his infinite wisdom and patience, without which none of my work would be possible. Professor Sites was always an advocate for my best interests and allowed me to grow not only professionally and academically, but personally as well. I would also like to extended my deep appreciation to my committee, Professor W.S. Sampath, Professor Justin Sambur, Dr. Amit Munshi, and Dr. Angus Rockett for their time and deep knowledge of physics, chemistry, materials science, and mechanical engineering. I am thankful to the funding organization NFS I/UCRC (Industry & University Cooperative Research Program) for funding my work and providing the opportunity to work with many wonderful people at First Solar and throughout the solar industry. I would also like to thank the National Renewable Energy Laboratory (NREL), Dr. C. S. Jiang, and Dr. Darius Kuciauskas for providing the opportunity to work with them and the invaluable insight they provided into the world of photovoltaics.

A big shout out to my family, without whom none of this would be possible. I appreciate my mother, Stacey Hill, for always supporting me throughout the years, and my late father, David Hill, for having been foundational in my devlopment. I would also like to thank my brother, Connor Hill, for always keeping it real. Of course my beautiful partner, Sarina Daniels, was always there for me, and helped to maintain my sanity throughout. Her parents, Russ Daniels and Mary Evelyn Daniels, have been a constant source of support and encouragement, and I am grateful for their love and kindness.

I have to give special thanks to everyone at First Solar's California Technical Center in Santa Clara, California for providing me the opportunity to work in an industrial research internship for three years during my PhD alongside them. My work would not possibly be the same without everyone there. I was always surprised by the insight my first manager, Dr. Sachit Grover, provided during our many meetings and am forever grateful for the many research opportunities he fostered for me. I was luckily enough to work under another wonderful manager at First Solar, Dr. Rouin Farshchi, who not only provided his deep knowledge of thin-film processing but many great

memories of fourth of July chili cook offs and The Mars Volta. None of my work at First Solar could have been possible without the many technicians, maintenance, and facilities staff on-site, who's hard work and often needed levity offered during my research was always appreciated.

Of course I have to thank everyone at Colorado State University. I worked alongside many brilliant, inspiring, and generous people during my time there. I am grateful for all the support, advice, and meaningful discussions I had with each and everyone I met. I am especially appreciative of the School of Materials Science and Engineering staff, especially Carolina Banuelos and Annika Sundsten, for believing in me and always supporting my adventures.

DEDICATION

This work is dedicated to my lead bead Sarina Daniels, my short king Blizzard, and the crawling chaos Fish & Chips. Y'all are the light that powers my solar cell.

TABLE OF CONTENTS

ABSTRACT ii
ACKNOWLEDGEMENTS iv
DEDICATION vi
LIST OF FIGURES ix

Chapter 1 Introduction 1
1.1 Photovoltaics for Energy Generation 1
1.2 Physics of Semiconductors 4
1.2.1 Doping Semiconductors 6
1.2.2 Photon Absorption and Charge Generation 8
1.2.3 Quasi-Fermi Level Splitting 11
1.2.4 PN Junctions 13
1.2.5 Charge Transport in Photovoltaic Devices 16
1.2.6 Charge Carrier Recombination Mechanisms 19
1.3 Single Junction Terrestrial PV 20
1.4 Tandem Photovoltaics 22
1.5 Analysis of Photovoltaic Devices 24
1.5.1 Current-Voltage Measurements 24
1.5.2 Capacitance-Voltage Measurements 27
1.5.3 Quantum Efficiency 28
1.5.4 Steady-state Photoluminescence 29
1.6 CdSeTe Solar Cells 30
1.6.1 Fabrication of CdSeTe Devices 32

Chapter 2 Group-V Doping in CdSeTe 38
2.1 Introduction 38
2.2 Processing Group-V Doped CST for High-Efficiency Devices 39
2.2.1 Overview of processing steps 40
2.3 Significant Factors Enabling >20% As-doped Devices 43
2.3.1 Impact of Oxygen Exposure on Dopant Activation 45
2.3.2 Impact of Changing Ex-situ Dopant Concentration 48
2.4 Novel Processing to Increase Dopant Activation 54
2.4.1 Selection of Oxygen Getters for Increased Dopant Activation 55
2.4.2 Introduction of Oxygen Getters to CST 56
2.4.3 Results of Oxygen Getter Study 56
2.5 Conclusions 60

Chapter 3 Intrinsic CdSeTe devices and their properties 63
3.1 Intrinsic Defects in CST 63
3.2 Determining Impact of Intrinsic Defects in CST Devices 65
3.2.1 Results of CST Devices with Various Dopants 67

3.2.2 Spatial Distribution of Elements and Electric Fields in CST 72
3.3 Significant Defects Impacting Type Conversion in CST 77
3.4 Conclusions 84

Chapter 4 Large Bandgap CdSe 87
4.1 Introduction 87
4.2 CdSe Absorbers 88
4.2.1 Deposition of CdSe at Colorado State University 88
4.3 CdSe Device Fabrication 95
4.3.1 General Requirements for CdSe Device Fabrication 96
4.3.2 CdSe Devices with Varied Absorber Thickness 99
4.4 Voltage Losses in CdSe Devices 102
4.4.1 Fundamental Voltage Limits of CdSe 102
4.4.2 Calculated Voltage Losses in CdSe Devices 105
4.4.3 Absolute Photoluminescence of CdSe Absorbers 107
4.4.4 Temperature and Intensity Dependent Measurements of CdSe 109
4.5 Conclusions 114

Chapter 5 Conclusions and Future Work 116
5.1 Group-V Doped CST Summary 116
5.2 Future Work in Group-V Doped CST 119
5.3 CdSe Device Summary 120
5.4 Future Work in CdSe Devices 121

Bibliography 123

LIST OF FIGURES

1.1 Demonstration of anthropomorphic climate change . . . 2
1.2 Energy production trends historically and predicted up to 2050 . . . 3
1.3 Record cell efficiencies tracked by NREL . . . 4
1.4 Absorption coefficient of various materials as a function of wavelength. . . . 9
1.5 Absorption coefficient and generation depth as a function of wavelength for CdTe. . . . 10
1.6 Solar spectrum outside of the atmosphere (AM0) and at AM1.5G. . . . 11
1.7 Blackbody approximation for solar spectrum . . . 12
1.8 NP junction formation . . . 15
1.9 Different types of recombination events are shown here. . . . 19
1.10 Efficiency and main parameters as a function of bandgap . . . 22
1.11 Efficiency contours for a two-terminal tandem device. . . . 23
1.12 Example JV image . . . 24
1.13 Set up of the substrate JV measurements system outside the light tight enclosure. . . . 26
1.14 Example QE curve . . . 29
1.15 Example PL graph . . . 30
1.16 CdSeTe bowing diagram . . . 31
1.17 CdTe deposition methods . . . 33
1.18 Example cell structure used in this work . . . 34
1.19 Tabulated work functions for various metals . . . 36

2.1 Diagram of the as-received bilayer absorbers with ex-situ group-V doping. . . . 40
2.2 $CdCl_2$ processing and annealing steps . . . 41
2.3 Example completed CdSeTe device . . . 42
2.4 Furnace used in this work . . . 42
2.5 JV and CV results for various annealing conditions . . . 44
2.6 Glass-side PL for various annealing conditions . . . 45
2.7 DSIMS results for various annealing conditions . . . 46
2.8 Determination of activation ratios for various annealing conditions . . . 47
2.9 QE results for various annealing conditions . . . 48
2.10 PL for various doping concentrations . . . 49
2.11 TRPL for various doping concentrations . . . 50
2.12 JV results for various doping concentrations . . . 51
2.13 QE and CV for various doping concentrations . . . 52
2.14 JV low and medium doping concentrations . . . 53
2.15 Ellingham digram for oxygen getter selection . . . 55
2.16 Overview of results from oxygen getter implanted devices . . . 57
2.17 Simulation of and SIMS result of oxygen getter implants . . . 58
2.18 SIMS profiles of dopant and oxygen relations . . . 59

3.1 Example of active and nonactive dopants in CdTe . . . 64
3.2 Illustration of superstrate vs substrate measurement configurations . . . 67

3.3 Substrate and superstrate JV measurements of CST with various dopants 68
3.4 QE of CST with various dopants 69
3.5 CV of CST with various dopants 70
3.6 PL of CST with various dopants 71
3.7 TRPL of CST with various dopants 72
3.8 KPFM of CST with various dopants 73
3.9 SIMS data for CST with various dopants 75
3.10 Cross-sectional CL images of intensity and bandgap 76
3.11 CL spectra taken from the cross-sections 77
3.12 Thickness and composition of Se uniterns from XRF 78
3.13 PL of CST uniterns with X = 0, 0.15, and 0.3 compared to graded Se 80
3.14 TRPL of CST uniterns with X = 0, 0.15, and 0.3 compared to graded Se 81
3.15 JV of CST uniterns with X = 0, 0.15, and 0.3 compared to graded Se 81
3.16 QE of CST uniterns with X = 0, 0.15, and 0.3 compared to graded Se 82
3.17 CV of CST uniterns with X = 0, 0.15, and 0.3 compared to graded Se 83
3.18 Absolute PL of CST uniterns with X = 0, 0.15, 0.3, and 0.4 84

4.1 Vapor saturation curve for CdSe 89
4.2 Diagram of ARDS parameters for CdSe 89
4.3 XRF and transmission results for CdSe with various thickness 90
4.4 Grain growth and PL emission increase for CdSe with $CdCl_2$ treatment 91
4.5 Cross-section and plane view SEM of CdSe with dry and wet $CdCl_2$ treatments 92
4.6 Cross-section SEM of CdSe with wet $CdCl_2$ and shunting as result of dry $CdCl_2$ 93
4.7 ToF-SIMS of CdSe after wet $CdCl_2$ process 94
4.8 PL and TRPL of CdSe after wet $CdCl_2$ process 95
4.9 Illustration of solution based oHTL deposition for CdSe 96
4.10 JV results for CdSe with oHTL and TMO combinations 98
4.11 JV results of CdSe devices using absorbers deposited at CSU 100
4.12 QE results of CdSe devices using absorbers deposited at CSU 101
4.13 Simulated effect on V_{OC}^{RAD} for CdSe as function of E_U 104
4.14 JV and QE for example CdSe cell with > 900 mV V_{OC} 105
4.15 Absolute PL for thin CdSe absorber 108
4.16 Absolute PL for thin and thick CdSe absorber 110
4.17 Results of defect emission from temperature dependent PL 111
4.18 Results of bandgap and defect emission from intensity dependent TRPL 112

Chapter 1

Introduction

This thesis is concerned with fabricating and understanding photovoltaic devices based around II-VI chalcogenide technology with a general theme of selenium and its role in CdTe based photovoltaics(PV). This will be broken into three distinct parts; first focusing on p-type cadmium selenium telluride ($CdSe_XTe_{1-X}$ or CST) solar cells with group-V doping, second on intrinsic CST, and third on n-type cadmium selenide (CdSe).

1.1 Photovoltaics for Energy Generation

The past century and a half has witnessed an exponential rise in fossil fuel consumption, which has been strongly correlated with elevated atmospheric CO_2 concentrations and a corresponding increase in global mean temperatures [1]. In contrast, renewable energy sources—such as wind, geothermal, and solar—derive from naturally replenished reservoirs and offer a sustainable alternative. While these sources are continuously available, they are inherently flow-limited, meaning their availability is constrained by natural variability. Unlike fossil fuels, which are finite and require energy-intensive extraction processes, renewable resources present a cleaner and more enduring foundation for future energy systems.

In the United States, the transition from fossil fuels to renewable energy has accelerated notably over the past two decades, driven by both environmental imperatives and economic incentives. According to the U.S Energy Information Administration (EIA), energy generated in the U.S. from photovoltaic (PV) sources reached approximately 58,000 million kilowatthours in 2024, representing a 500-fold increase compared to levels in 2005. Solar energy generation now accounts for nearly 4.8% of total electricity generation in the country. Utility-scale solar, in particular, has benefited from falling levelized costs of electricity, government incentives, and advances in grid integration. Coupled with increased research incentives, the demand for solar energy in the U.S. is

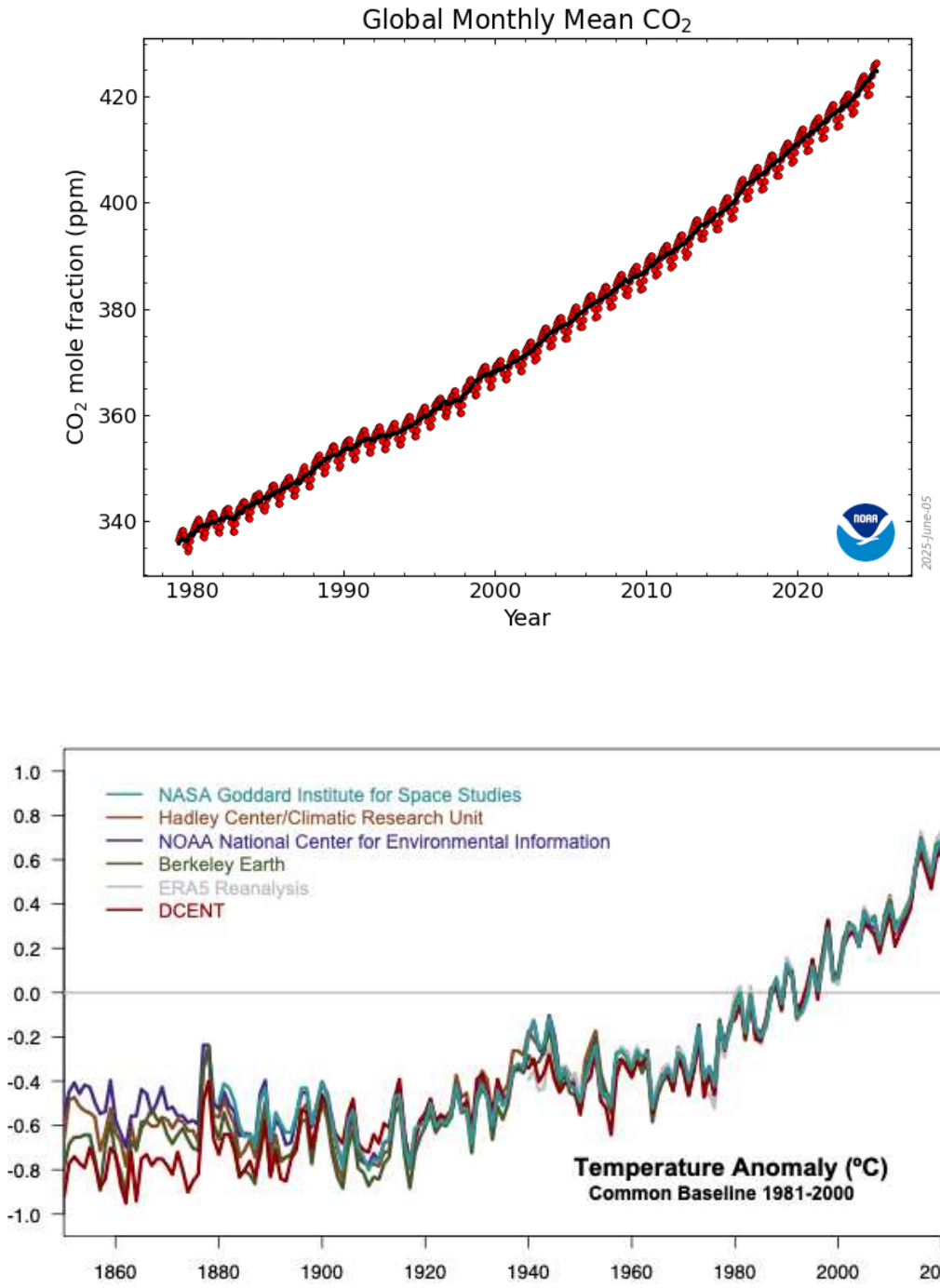

Figure 1.1: These two graphs demonstrate the correlation between global CO_2 emission [1] and average global temperature [2] increases. Temperature scale is normalized such that the mean temperature from 1981 = 0.

projected to continue growing robustly, with the EIA forecasting that solar will become the largest single source of electricity generation in the U.S. by 2050, surpassing both natural gas and coal [3].

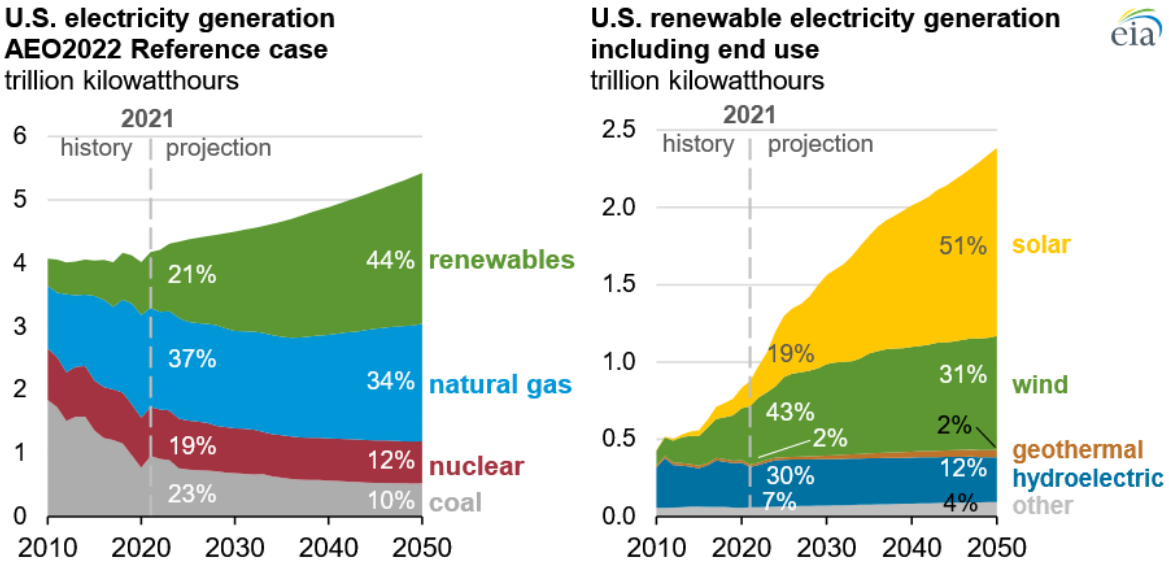

Figure 1.2: U.S. energy generation forecasts indicate that the share of renewable sources will grow from 21% (2021) to 44% in 2050. This would make renewables the primary source of energy generation in the US, with solar projected to account for at least 50% of this, representing more than 1,100 TWh of generation. [3]

As the demand for renewable energy increases, there is a growing focus on developing photovoltaic (PV) materials that are both cost-effective and efficient. Silicon (Si) remains the dominant material in PV technology due to its abundance and mature processing infrastructure. However, Si's indirect bandgap necessitates thick absorber layers (hundreds of microns) and high-temperature, energy-intensive processing to achieve high efficiencies. These limitations have motivated the exploration of alternative PV materials that can be processed more rapidly and with less material.

Thin-film PV technologies have emerged as a promising solution, utilizing direct bandgap semiconductors that efficiently absorb sunlight within just a few microns of material—significantly reducing material usage and enabling lower-cost manufacturing. The best-performing cells from a range of PV technologies are summarized in Figure 1.3 [4].

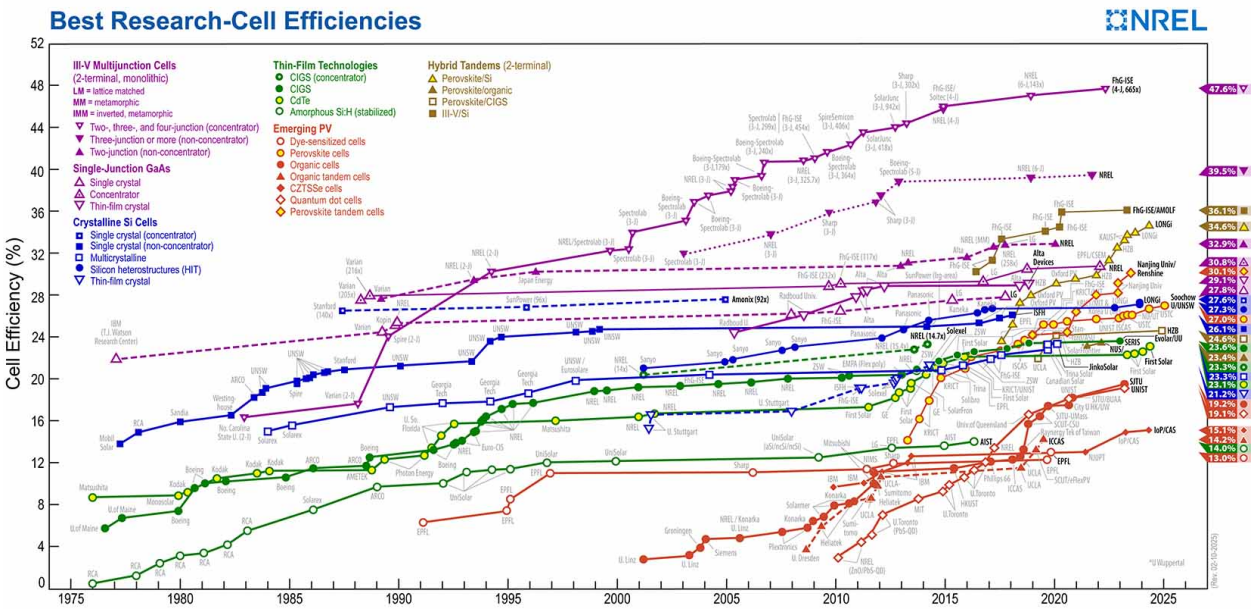

Figure 1.3: Record cell efficiencies tracked by NREL over the past 50 years. Note CdTe in green circles filled with gold recently achieving over 23% efficiency.

1.2 Physics of Semiconductors

The classification of materials into conductors, semiconductors, and insulators is fundamentally determined by their electronic band structure and the energy gap between the valence and conduction bands. In conductors (metals), the valence and conduction bands overlap or are partially filled, allowing electrons to move freely and conduct electricity readily. Insulators possess a large energy gap (typically > 3 eV) between the valence and conduction bands, preventing electron excitation under normal conditions and resulting in negligible electrical conductivity. Semiconductors occupy the intermediate regime, with moderate bandgaps typically ranging from 0.5 to 3.5 eV, allowing for controlled electrical conductivity that can be modulated through temperature, doping, or external fields.

Semiconductors can be classified by their chemical composition and crystal structure. Elemental semiconductors, such as silicon (Si) and germanium (Ge), are composed of a single element arranged in diamond cubic crystal structures. Binary compound semiconductors include II-VI materials like cadmium telluride (CdTe) and zinc sulfide (ZnS), III-V compounds such as gallium arsenide (GaAs) and indium phosphide (InP), and IV-IV compounds like silicon carbide (SiC).

Ternary and quaternary compounds, such as copper indium gallium diselenide (CIGS) and hybrid organic-inorganic perovskites (e.g., methylammonium lead iodide, $MAPbI_3$), offer additional tunability of electronic properties through compositional control.

The crystalline structure further differentiates semiconductors. Single-crystal materials exhibit perfect periodic atomic arrangement, providing optimal electronic properties. While the electrical properties of single crystal compounds are more ideal than that of their polycrystalline counterparts [5], a trade-off between the ease / cost of fabrication, reproducibility, and performance lead to most PV devices being polycrystalline. The major difference between single crystal and polycrystalline semiconductors is the formation of grain boundaries (GB) which occurs crystal growth as crystalites with differing orientation begin to nucleate at various locations on the growth surface and form a discontinuous lattice as they meet, which act as defect sites but allow for lower-cost fabrication.

The electronic band structure of semiconductors arises from the quantum mechanical description of electrons in periodic crystal lattices, governed by Bloch's theorem. When atoms are brought together to form a solid, their discrete atomic energy levels broaden into continuous bands due to orbital hybridization. The highest occupied band (valence band) and the lowest unoccupied band (conduction band) are separated by the fundamental energy gap, which determines the material's optical and electrical properties.

Within the atomic semiconductor, discrete energy states are formed based on electron orbital states, typically referred to as the "nth quantized state". This is what is solved for in the "particle in a box" problem using Schrodinger's equation, which itself is simply a quantization of the law of conservation of energy. Within the bulk solid however, the spacing between atoms is reduced to the point that orbital states between neighboring atoms begin to overlap and a near continuous "band" of allowed energy states begins to form. These allowed band states are separated by an energy known as the "bandgap" (E_g) which separates states which are almost completely occupied by electrons (valence band, E_v) from those which are almost completely unoccupied (conduction band, E_c), where the difference between these two bands defines the bandgap energy ($E_g = E_c$ -

E_v). The absence of the electron can be rather considered to be occupied instead by a "hole" which is a pseudo-particle, in that it does not physically exist, but has a charge state equal and opposite to that of the electron. The distribution of electrons and holes across energy states (E) is defined by the Fermi-Dirac distribution as

$$f(E) = \frac{1}{e^{(E-E_F)/k_BT} + 1} \tag{1.1}$$

where k_B is Boltzmann's constant and T is the temperature in kelvin and E_F is the Fermi energy which is the energy where the probability of electron/hole occupation is 50%. The concentration of electrons (n) and holes (p) within a semiconductor is defined by

$$n = N_C e^{(E_F-E_C)/kT} \tag{1.2}$$

$$p = N_V e^{(E_V-E_F)/kT} \tag{1.3}$$

where N_C and N_V are the effective density of states for conduction and valence bands respectively and are given by

$$N_C = 2\left(\frac{2\pi m_n^* kT}{h^2}\right)^{3/2} \tag{1.4}$$

$$N_V = 2\left(\frac{2\pi m_p^* kT}{h^2}\right)^{3/2} \tag{1.5}$$

where $m_{n,p}^*$ are effective electron and hole masses.

1.2.1 Doping Semiconductors

The position of the Fermi energy level relative to the allowed bands determines the conductivity state of the material. The Fermi energy level can be influenced by impurities within the lattice, which is typically accomplished through the introduction of dopant atoms (extrinsically doped)

the function of which can be simply considered by the change in the number of valance electrons within each atom in the atomic lattice. For example, phosphorus (P) is a group-V element commonly used to n-type dope Si (group-IV) due to the extra valance electron in P relative to Si which results in a net increase in the concentration of electrons within the bulk lattice. Conversely, boron (B) is a group-III element used to p-type dope Si due to the lack of a valance electron relative to Si, resulting in a net increase in the concentration of holes within the bulk lattice.

A more detailed explanation is that dopant atoms introduce defect bands into the lattice due to a perturbation of the wavefunction given by Bloch's function. These are known as either donor or acceptor defects for n- and p-type doping respectively, where N_d and N_a are the density of donor or acceptor states. These defect bands are most useful when they are "shallow", that is to say they are <3kT (100meV at room temp) from either the conduction band (CB) or valance band (VB). Such shallow defect levels are easily ionized into / out of at room temperature, and thus for a shallow acceptor near the VB, electrons can easily be ionized out of the VB, leaving behind a hole and increasing the net concentration of holes while a shallow donor level near the CB allows for electrons to ionize into the CB, recombining with holes, and reducing the net concentration of holes.

Within an intrinsic semiconductor, where n = p, the Fermi energy is essentially in the middle of the bandgap and can be expressed by:

$$E_F = \frac{E_C - E_V}{2} + \frac{kT}{2} \ln\left(\frac{N_V}{N_C}\right) \tag{1.6}$$

When the semiconductor doped n-type, and therefore has $n \approx N_d \gg p$, the Fermi energy changes to

$$E_F = E_C + kTln\left(\frac{N_d}{N_C}\right) \tag{1.7}$$

and similarly for p-type doping with $p \approx N_a \gg n$ where

$$E_F = E_V - kTln\left(\frac{N_a}{N_V}\right) \tag{1.8}$$

which shows that n-type doping leads to a Fermi energy level close to the conduction band while p-type doping leads to a Fermi energy level close to the valence band.

1.2.2 Photon Absorption and Charge Generation

When a semiconductor is excited through an external force, such as an applied bias or under illumination, electrons can be excited from their ground state to a higher state. In the case of photovoltaics, the absorption of photons with energy greater than the bandgap energy ($E_{ph} > E_g$) will excite electrons from the valence band to the conduction band leaving behind a hole in what is referred to as an electron-hole pair (EHP). This process is known as photo-excitation and is the basis for photovoltaic operation. So long as the coulombic potential binding the EHP is overcome, the excited electron and hole are then free to move within the semiconductor, generating an electric current.

The absorptance of a semiconducting film is characterized by its absorption coefficient (α), which quantifies the fraction of incident light absorbed per unit distance within the material and is determined through Beer's law as

$$\alpha(\lambda) = \frac{1}{d}\ln\left(\frac{I_0}{I(d)}\right) \tag{1.9}$$

where d is the thickness of the material, I_0 is the incident light intensity, and $I(d)$ is the transmitted light intensity at depth d within the material. Example of the absorption coefficient for a few materials is shown in Figure 1.4.

The absorption coefficient of a material is inherently tied to it's bandgap, as a material becomes more transparent to photons as their energy approaches and reduces below the bandgap energy. A careful distinction must be made when discussion the transparency of a material though, as the thickness of a material plays an important role in determining the transparency. The depth of

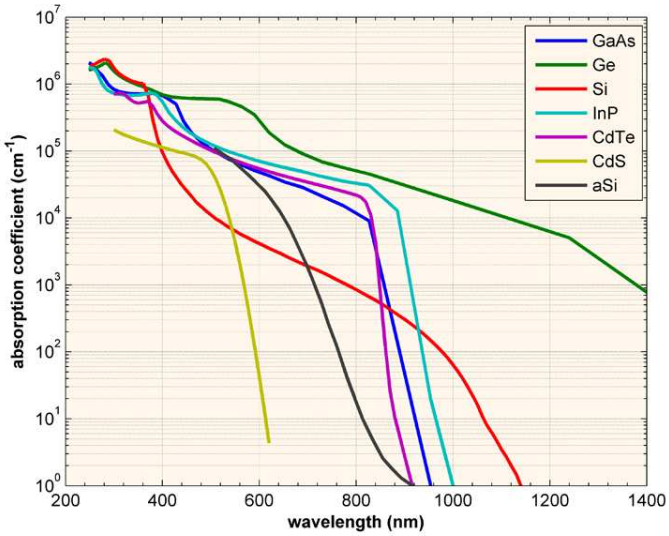

Figure 1.4: Absorption coefficient of various materials as a function of wavelength.

photon absorption is given by the inverse of the absorption coefficient, thus as the absorption coefficient decays exponentially for E<E_g, the depth at which these photons must travel before being absorbed increases exponentially. From this, it can be understood that photons with higher energy are absorbed and generate EHPs close to the incident surface, whereas lower energy photons penetrate deeper into the material before being absorbed and generating EHPs.

Due to the large absorption coefficient (>10^4 cm^{-3}) of CdTe, only a few microns of material are needed to absorb the majority of incident light, as shown in Figure 1.5 as opposed to materials like silicon which required tens to hundreds of microns to absorb the same fraction of incident photons. It is due to this property that CdTe absorbers may be fabricated as "thin-films" and has allowed CdTe to become a prominent material in PV technology.

The generation rate of EHPs ($G(x)$) at a depth x within the semiconductor can be expressed as:

$$G(x) = \alpha(\lambda) I_0 e^{-\alpha(\lambda)x} \tag{1.10}$$

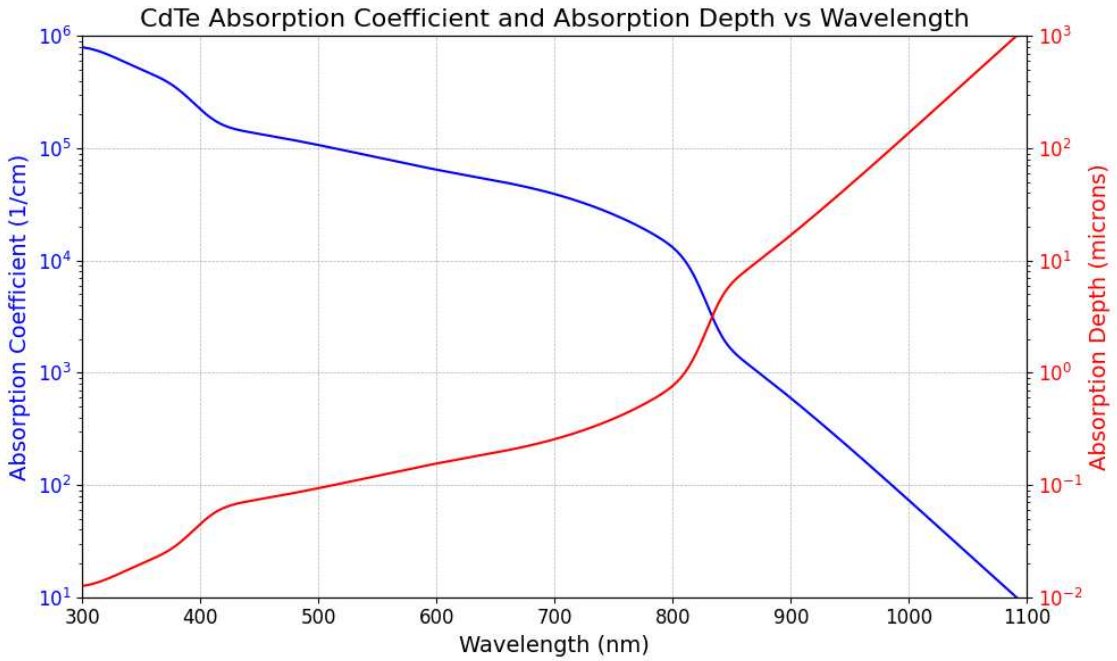

Figure 1.5: Absorption coefficient and generation depth as a function of wavelength for CdTe.

where I_0 is the incident photon flux at the surface, $\alpha(\lambda)$ is the absorption coefficient, and x is the depth of absorption in the semiconductor. This generation profile represent the number of EHPs generated per unit volume per unit time at a given depth within the material.

So how can we generate useful electricity from the sun anyway? The terrestrial spectrum, accounting for absorption from the atmosphere, is known as an air mass spectrum, and variations in solar intensity as a function of latitude are modeled as

$$AM = \frac{1}{\cos\theta} \tag{1.11}$$

where θ is the zenith angle from the equator. The spectrum outside the atmosphere is considered AM0, while AM1 (for $\theta = 0$) is for the equator. In research, the AM1.5 spectrum is most commonly used as it corresponds to a zenith of $\approx 48^\circ$. These spectra are shown below in figure Figure 1.6.

The AM1.5G direct spectrum produces an integrated power density of roughly 100 $\frac{mW}{cm^2}$ which is available for power conversion and what is most typically considered as the incident photon flux

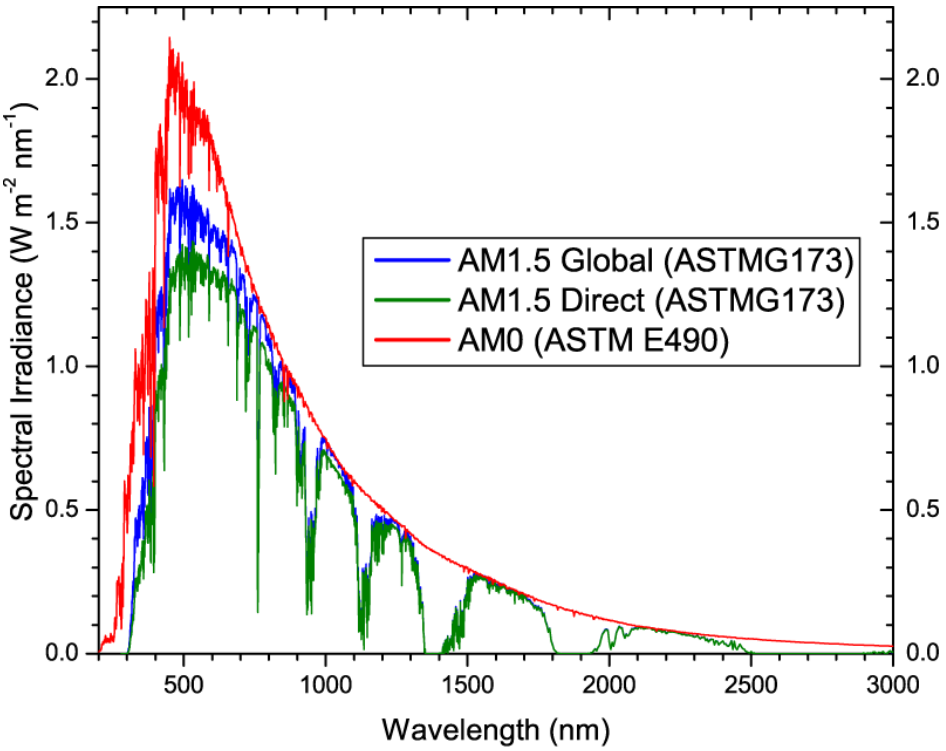

Figure 1.6: Solar spectrum outside of the atmosphere (AM0) and at AM1.5G.

used in photovoltaic modeling. Considering the sun as a blackbody emitter, the solar spectrum can be approximated by Planks law as given by

$$I(\lambda, T) = \frac{2\pi hc^2}{\lambda^5} \frac{1}{e^{\frac{hc}{\lambda k_B T}} - 1} \tag{1.12}$$

where h is planks constants, c is the speed of light, k_B is Boltzmann's constant, and T is the temperature of the emitter, which is considered to be 5800 K for the sun. This approximation is shown in Figure 1.7 as the orange line, which is compared to the AM1.5G spectrum (green) and a 300 K blackbody (blue). The AM1.5G spectrum and its blackbody are given by the right-hand axis, while the 300K blackbody is given by the left-hand axis.

1.2.3 Quasi-Fermi Level Splitting

While the previously described Fermi energies describe the equilibrium state of a semiconductor, this is modulated by the production of EHPs under illumination. As EHPs are generated, the

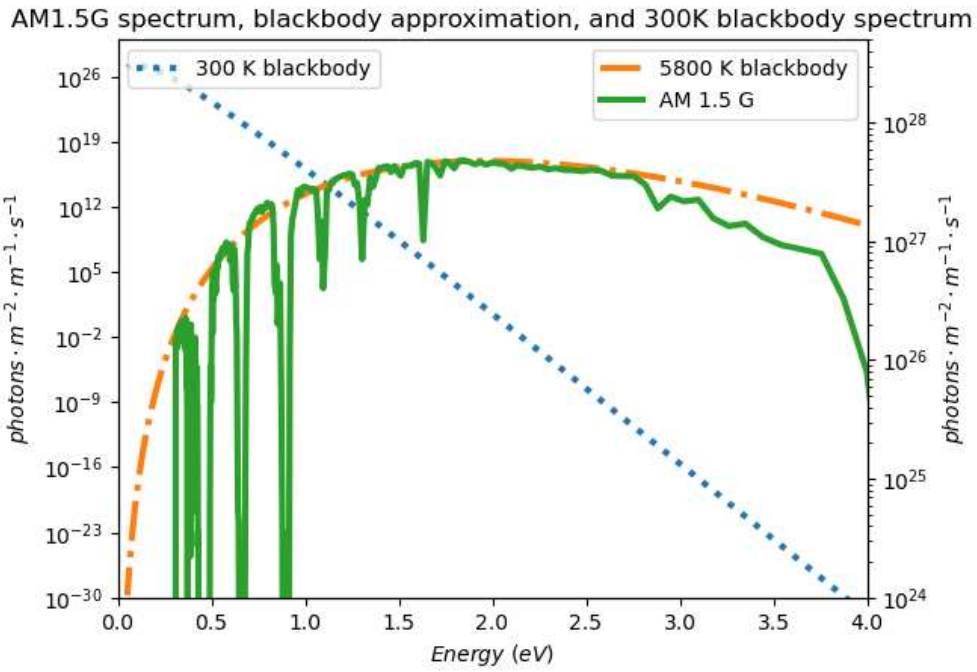

Figure 1.7: AM1.5G spectrum, shown in green, and it's approximated blackbody spectrum at 5800K, shown in orange, with a 300K blackbody spectrum shown in blue. Note the AM1.5G, and its blackbody are the right-hand axis over 5 orders of magnitude, while the 300K blackbody on the left axis extends over 60 orders of magnitude.

concentration of the electrons or hole concentrations (n / p) can no longer be approximated by the density of donor or acceptor states (N_a / N_d). To account for this, the equilibrium Fermi level is considered to "split" into two quasi-Fermi levels for electrons in the conduction band ($E_{F,C}$) and holes in the valance band ($E_{F,V}$) which can be expressed as:

$$E_{F,C} = E_F + kT \ln\left(\frac{n}{N_C}\right) \tag{1.13}$$

$$E_{F,V} = E_F - kT \ln\left(\frac{p}{N_V}\right) \tag{1.14}$$

where N_C and N_V are the effective density of states for the conduction and valance bands as previously described with equations (1.2) and (1.2), but modulated by each quasi-Fermi level. This is what is known as quasi-Fermi level splitting (qFLS) and can be approximated by the difference between the two quasi-Fermi levels by:

$$\text{qFLS} = E_{F,C} - E_{F,V} = E_g + kT \ln\left(\frac{np}{N_C N_V}\right) \tag{1.15}$$

This qFLS represents the potential difference between electrons in the valance band and holes in the conduction band, and thus is a limiting factor in the maximum work that can be done by charges generated within a semiconductor. This shows the importance of doping in semiconductors, which increases the concentration of either electrons or holes, and thus increases the qFLS. Additionally, the rate at which EHPs are generated influences qFLS, which is an important consideration within photovoltaic devices as the generation rate is a function of the incident light intensity.

1.2.4 PN Junctions

While the generation of EHPs and the qFLS within a semiconductor establishes the potential to perform work, this must be realized through extraction of these charges into an external load to performance such work. Within most semiconductor devices, this is achieved through the formation of a pn-junction. Joining together a p-type and n-type semiconductor creates a pn-junction, which is considered a homojunction if both n- and p-type are the same materials or a heterojunction if the n- and p-type are different materials. As the two materials are joined, the difference in concentration of electrons (holes) between the n- and p-type material creates a diffusion gradient for electrons (holes) which allows an initial mobility. As electrons (holes) diffuse toward the p- (n-)type material, the atomic ions will be left with a positive (negative) charge state which establishes an electric field directed towards the p-type material.

In terms of the band states of the two materials, joining together the n- and p-type materials will force the two Fermi levels to shift towards an equilibrium state, which results in band bending at the interface with the conduction band (valance band) of the p-type (n-type) material bending downwards towards the p- (n-) type material. The band bending within the SCR creates a built-in potential defined as

$$V_{bi} = \frac{E_g}{q} - (\phi_n + \phi_p) \tag{1.16}$$

where ϕ_n = E_C - E_F and ϕ_p = E_F - E_V. This can be expressed in terms of the concentration of charges instead as

$$V_{bi} = \frac{kT}{q} \ln \frac{np}{n_i^2} \tag{1.17}$$

where n and p are the majority charge carrier densities in the n-type (electrons) and p-type (holes) materials respectively, and n_i is the intrinsic carrier density of each undoped material.

Thus, the band bending at the pn-junction is equivalent to the strength of the electric field generated from carrier diffusion, as the difference in electric field strength over a distance is related to the difference in charge density through Poisson's equation by

$$\frac{dE}{dx} = \frac{\rho}{\epsilon} \tag{1.18}$$

where ρ is the charge density and ϵ is the permittivity of the material. The charge density can then be expressed in terms of the concentration of free electrons (n), free holes (p), acceptor states (N_a), and donor states (N_d) such that

$$\rho = q\left(p(X) - n(x) - N_a + N_d\right) \tag{1.19}$$

Under illumination, as EHPs are generated and qFLS occurs, electrons will flow from the high potential side of the conduction band (p-type region) to the low potential side of the conduction band (n-type region) as predicated by the conservation of energy. Meanwhile, holes will flow from the low potential side of the valance band (n-type region) to the high potential side of the valance band (p-type region). This can be colloquially be expressed as "electrons sink, holes float". This is shown in Figure 1.8 where the arrows indicate the direction of charge flow.

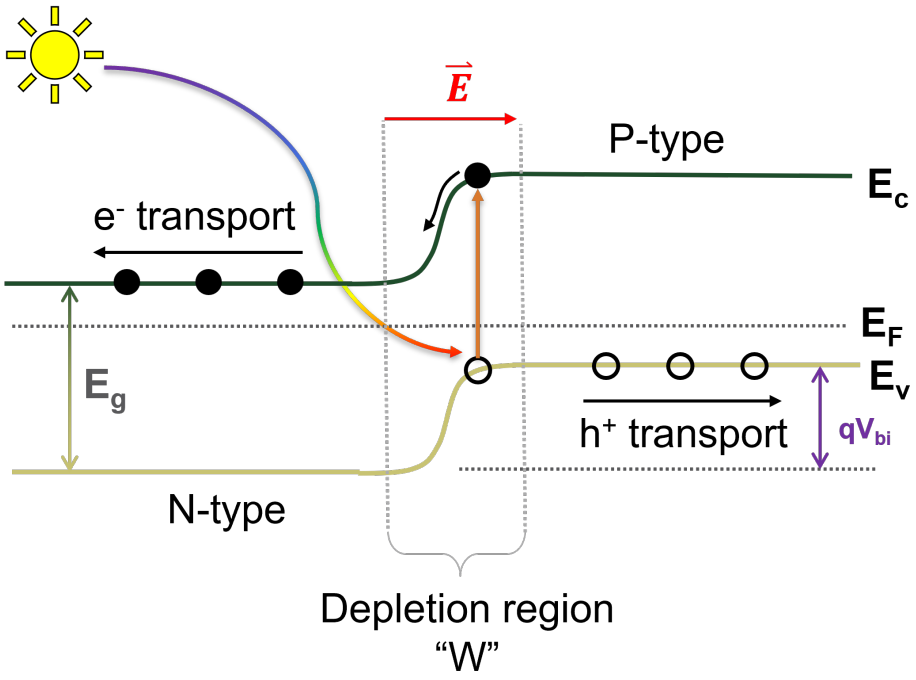

Figure 1.8: Example of PN-junction under illumination.

As generated charges are swept out by the electric field, a region devoid of free carriers is formed known as the "depleted region" or space-charge region (SCR) which has a width (W) defined by

$$W = \sqrt{\frac{2\epsilon\epsilon_0}{q}(V_{bi} - V)\left(\frac{1}{N_a} + \frac{1}{N_d}\right)} \tag{1.20}$$

where ϵ is the relative permittivity of the material, ϵ_0 is the permittivity of free space, V is an externally applied bias, and N_a and N_d are the acceptor and donor densities respectively. The region outside the depleted region is known as the quasi-neutral region (QNR).

In the absence of external illumination, an external bias applied across the PN junction causes charge carriers to be injected into the material, which will produce qFLS for each carrier type that can be modulated by the applied bias strength. At forward bias, when a positive voltage is applied to the p-type region, the width of the depleted region shrinks and the qFLS grows, leading to an exponential increase in current as the applied voltage exceeds the built-in voltage. Applying a

reverse bias causes the depleted region width to grow and qFLS to decrease, thus increasing the probability of EHPs to recombine and decreasing the current to the point of a "saturation current" represented as J_0. This can all expressed by a diode equation as given by

$$J = J_0 \left[e^{\left(\frac{qV}{AkT}\right)} - 1 \right] \tag{1.21}$$

where k is the Boltzmann constant, T is absolute temperature, V is the applied voltage, and A is the ideality factor, which is related to the kinetics of charge recombination. Under illumination, a photocurrent (J_{ph}) will be produced and acts as a current which flows against the current generated by a positive voltage injection. The total current under illumination is given by

$$J = J_0 \left[e^{\left(\frac{qV}{AkT}\right)} - 1 \right] - J_{ph} \tag{1.22}$$

1.2.5 Charge Transport in Photovoltaic Devices

The efficiency of a photovoltaic device is predicated on the extraction of generated charges from the absorbers material. To prevent the charges from stagnating and relaxing back to a lower energy state, resulting in charge recombination, some mobility must be imparted upon the charges. This may be accomplished through simple diffusion due to a carrier concentration gradient, or drift due to an established electric field as previously described. While described separately, these three processes (diffusion, drift, and recombination) occur simultaneously throughout the absorber. Within this section, a more detailed treatment of charge transport will be discussed before reviewing various recombination mechanisms.

In electric field in the depleted region, due to the built-in potential of the pn-junction band bending, imparts a mobility to charge carriers described by a drift velocity ($v_{drift,n/p}$) given by

$$v_{drift,n} = -\mu_n E \tag{1.23}$$

$$v_{drift,p} = \mu_p E \tag{1.24}$$

where μ_n and μ_p are the mobilities of electrons and holes, respectively, and E is the electric field strength. The negative sign for electrons indicates that they move opposite to the direction of the electric field. While the mobility is a material-dependent parameter that quantifies how quickly a charge carrier can move through the semiconductor material in response to an electric field, the velocity can ultimately be reduced due to various scattering events related to impurities within the crystal lattice.

The current density due to drift for electrons and holes $J_{drift,n/p}$ can be expressed as

$$J_{drift,n} = -qnv_{drift,n} \tag{1.25}$$

$$J_{drift,p} = qpv_{drift,p} \tag{1.26}$$

for the given concentration of electrons (n) and holes (p) within the semiconductor. The total current density J_{drift} in the depleted region can then be expressed as:

$$J_{drift} = q\left(n\mu_n + p\mu_p\right)E \tag{1.27}$$

In the quasi-neutral region (QNR) of a photovoltaic device, the concentration of charge carriers (electrons and holes) is relatively uniform, and the primary mechanism for charge transport is diffusion, driven by the concentration gradient of the carriers.

The diffusion current density $J_{diff,n/p}$ for electrons and holes can be described by Fick's first law:

$$J_{diff,n} = qD_n\nabla n \tag{1.28}$$

$$J_{diff,p} = qD_p \nabla p \tag{1.29}$$

where q is the elementary charge, $D_{n,p}$ is the diffusion coefficient for electrons or holes, and $\nabla n, p$ is the concentration gradient of electrons or holes within the QNR. The diffusion coefficient is a material-dependent parameter that quantifies how quickly charge carriers can diffuse through the semiconductor material and is related to the mobility of the carriers by the Einstein relation:

$$D_n = \frac{kT}{q}\mu_n \tag{1.30}$$

$$D_p = \frac{kT}{q}\mu_p \tag{1.31}$$

Given that the net current through the semiconductor device is a combination of both drift and diffusion currents, the regions in which these individual current processes dominates is relevant. As diffusion occurs outside the junction field, the diffusion length L is a critical parameter, defined as the average distance a carrier can travel before recombining. It is given by:

$$L_n = \sqrt{D_n \tau_n} \tag{1.32}$$

$$L_p = \sqrt{D_p \tau_p} \tag{1.33}$$

where $\tau_{n,p}$ is the lifetimes of electrons or holes and is also a material-dependent property. It is ideal for the diffusion length to be at least on the order of the thickness of the QNR, or put otherwise greater than the distance between the generation point and the junction. This is important as it allows for the generated EHPs to diffuse to the junction before recombining, thus increasing the efficiency of the device.

1.2.6 Charge Carrier Recombination Mechanisms

Once EHPs are generated, they are either be separated and (ideally) collected at an electrode to produce useful energy, or they will ultimately recombine. Recombination of generated EHPs fundamentally limits the performance of a PV devices as it reduces the net concentration of charges used for conversion of light to electricity. There are three primary recombination mechanisms which should be discussed in this work: radiative, non-radiative, and surface/interface recombination. These evens are shown in Figure 1.9.

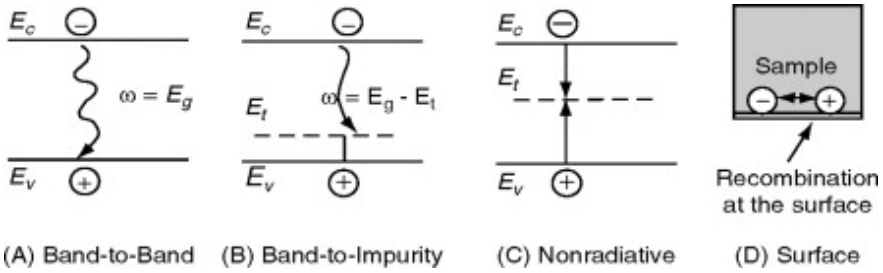

Figure 1.9: Different types of recombination events are shown here.

Unwanted recombination within absorbers is predicated by the presence of so-called trap states within the bandgap, formed due to various impurities / defects within the atomic lattice. These defects form trap states due to a perturbation of the Bloch wave which describes the periodic potential arising from a repeating crystal lattice. This understanding makes clear why grain boundaries are recombination prone sites, as they are abrupt boundaries of the grain periodicity.

Radiative recombination can simply be considered as the reciprocal of absorption. That is, an electron in the conduction band relaxes to a lower energy states and emits a photon with energy equal to the difference in energy states. The rate (R_{rad}) at which this occurs is characteristic concentration of charge carriers in the valance and conduction bands, and can be expressed as:

$$R_{rad} = Bnp \tag{1.34}$$

where B is the radiative recombination coefficient which tends to be on the order of 10^{-10} cm^3 s^{-1} in CdTe [6].

Nonradiative recombination involves the dissipation of energy through mechanisms other than photon emission. The primary nonradiative recombination mechanisms are Auger recombination and Shockley-Read-Hall (SRH) recombination. Auger recombination occurs when a photon with energy greater than the bandgap is absorbed, resulting in excitation above the conduction band, or otherwise if any absorbed photon excites an electron already residing within the conduction band. As the electron relaxes back to the conduction band, excess energy will be dissipated as heat (thermalization) through phonon propagation (lattice vibrations) resulting in wasted energy. This process is more pronounced in materials with high carrier concentrations, as the probability of Auger recombination increases with the density of charge carriers and is not so significant within CdTe.

SRH recombination occurs via defect states or traps within the bandgap of the semiconductor. Electrons excited into the conduction band may relax back into unoccupied trap states within the bandgap, becoming "trapped" before being released back into the valance band. This processes results in the initial energy from photon absorption being split between two lower energy processes that and thus results in a net loss of energy.

1.3 Single Junction Terrestrial PV

Now that the generation and seperation of charges for PV operation has been established, the simple case of producing energy on earth's surface using a single junction PV device is considered. The definition of power conversion efficiency is simply

$$\eta = \frac{P_{out}}{P_{in}} \tag{1.35}$$

where P_{in} is the power input from the sun, given by the integrated AM1.5G spectrum (≈ 100 $\frac{mW}{cm^2}$). For an electrical device, P_{out} is determined by the product of current (I) and voltage (V). The current density (J) is typically used in place of I to account for a devices active area.

The maximum current density available from any given PV device can be determined through a few assumptions known as the detailed balance limit as originally detailed by Shockley and Quessier [7]. First, every photon with energy greater than the bandgap of the material will be absorbed and generate a charge pair ($\alpha(E > E_g) = 1$). Second, every charge pair will be collected and converted into useful electrical energy. This ideal case is known as the detailed balance limit, and provides the maximum current density which can be photogenerated in the absence of an applied bias, know as the Shockley-Quessier (SQ) short circuit current density (J_{SC}^{SQ}). This is given by

$$J_{SC}^{SQ} = q \int \alpha(E)\Phi(\lambda)d\lambda \tag{1.36}$$

where q is the elementary charge, $\alpha(\lambda)$ is the absorptance spectrum, and Φ_λ is the incident photon flux.

The maximum voltage available from a PV devices is then determined by the open circuit condition where the current is zero, and thus all generated charges are either recombined within the absorber or at interfaces/surfaces without extraction. This will result in the limiting saturation current discussed previously where these recombination events emit energy blackbody emitter at the devices temperature and can be described as:

$$J_{0,RAD} = q \int \alpha(\lambda)\Phi_{BB,T_{device}}(\lambda)d\lambda \tag{1.37}$$

The maximum open circuit voltage (V_{OC}^{SQ}) is then determined as:

$$V_{OC}^{SQ} = \frac{kT}{q} \ln\left(\frac{J_{SC}^{SQ}}{J_{0,RAD}}\right) \tag{1.38}$$

$$= \frac{kT}{q} \ln\left(\frac{\int \alpha(E)\Phi(\lambda)d\lambda}{\int \alpha(\lambda)\Phi_{BB,T_{device}}(\lambda)d\lambda}\right) \tag{1.39}$$

Considering the AM1.5G spectrum, the solution for these equations considering a step function absorptance at the bandgap of a given material is show in Figure 1.10. This shows that the ideal bandgap for single junction PV conversion is $\approx$ 1.4 eV where semiconductor with this bandgap could in theory convert roughly 34% of incident solar energy into useful electrical energy, ie. 34 $\frac{mW}{cm^2}$.

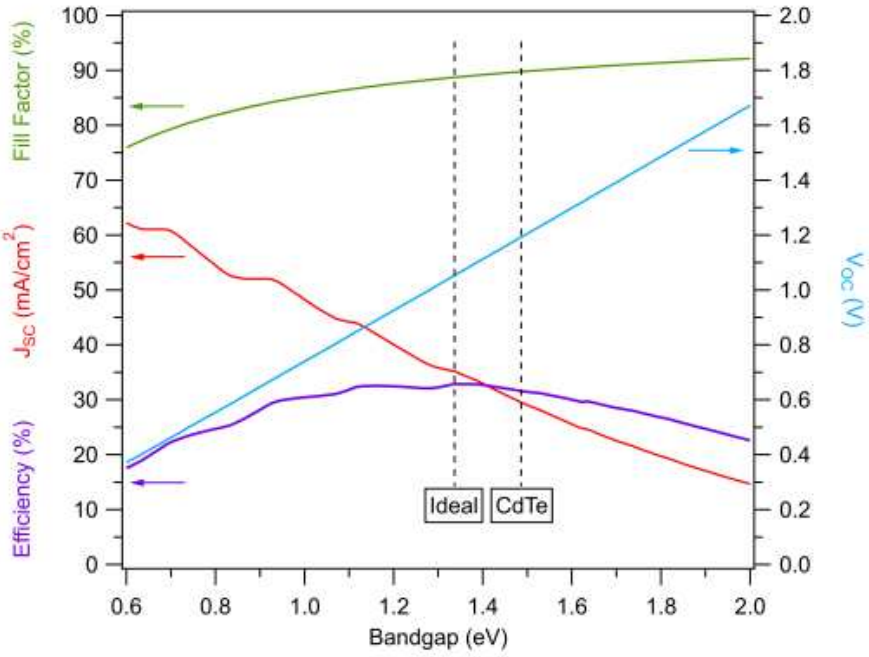

Figure 1.10: This graph shows the maximum theoretical short circuit current, open circuit voltage, fill factor, and resultant efficiency over a range of bandgap energies. Lines for CdTe and ideal solar cell are referenced in black.

1.4 Tandem Photovoltaics

One way to exceed the single junction SQ limit is to stack multiple single junction devices on top of each other, known as a tandem devices. Through a careful balance of the bandgaps of each device in the tandem stack, the top most cell can absorber high energy photons while being transparent to lower energy photons which can then be absorbed by the lower bandgap cell. As illustrated in Figure 1.11, the theoretical maximum efficiency for an ideal two-junction tandem

cell is approximately 46%, significantly higher than the 33% limit for single-junction devices. This optimal efficiency occurs when the bandgaps of the top and bottom cells are tuned to around 1.7 eV and 1.1 eV, respectively. Such pairing allows for near-complete harvesting of the solar spectrum, making tandem photovoltaics a leading candidate for next-generation high-efficiency solar technologies.

Among candidate materials for tandem top cells, cadmium selenide (CdSe) is a promising wide-bandgap absorber due to its direct bandgap of approximately 1.7 eV, making it well-matched for pairing with bottom cells such as silicon or CdTe in a two-terminal tandem configuration. CdSe can be deposited using established low-cost techniques such as close-space sublimation (CSS) and benefits from compatibility with existing CdTe processing infrastructure, reducing fabrication complexity.

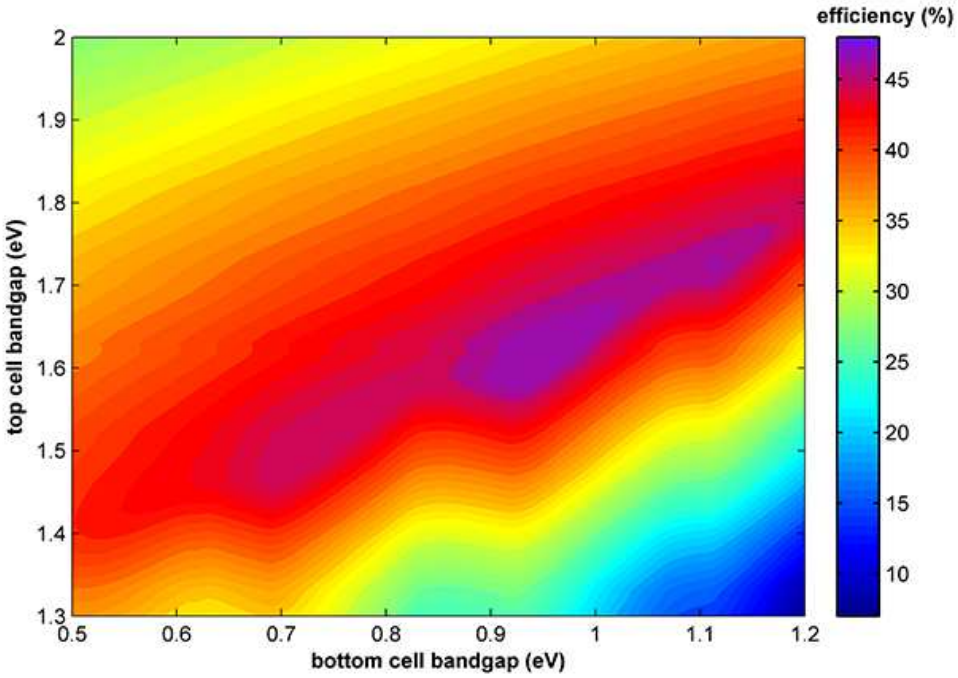

Figure 1.11: Efficiency contours for a two-terminal tandem device.

1.5 Analysis of Photovoltaic Devices

1.5.1 Current-Voltage Measurements

Current-voltage (JV) measurements are the primary method for evaluating photovoltaic device performance. By measuring current density as a function of applied voltage, key parameters are extracted: short-circuit current density (J_{SC}), open-circuit voltage (V_{OC}), and fill factor (FF). These parameters determine the power conversion efficiency (η) of the device.

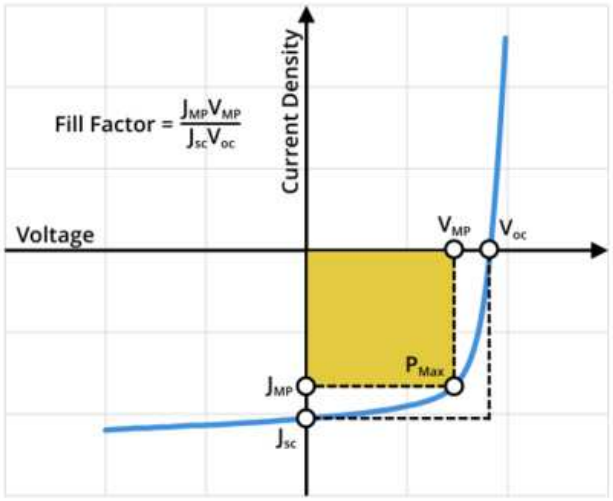

Figure 1.12: Example JV showing J_{SC}, V_{OC}, J_{MPP}, V_{MPP}, and P_{MAX}.

The short-circuit current (J_{SC}) is the current measured under illumination at zero applied voltage, reflecting the maximum photocurrent. The open-circuit voltage (V_{OC}) is the voltage at which the current drops to zero, limited by recombination losses. It can be expressed as:

$$V_{OC} = \frac{AkT}{q} \ln \frac{J_{ph}}{J_0} \tag{1.40}$$

The fill factor (FF) quantifies the "squareness" of the JV curve and is defined by:

$$FF = \frac{V_{MP}J_{MP}}{V_{OC}J_{SC}} \tag{1.41}$$

The overall efficiency is given by:

$$\eta = \frac{V_{OC} J_{SC} FF}{P_{in}} \tag{1.42}$$

A photovoltaic device can be modeled by an equivalent circuit including a diode with series resistance (R_S) and shunt resistance (R_{sh}). R_S represents resistive losses in the device and appears in both the exponential term (modifying the voltage across the diode) and the shunt resistance term of the full diode equation, while R_{sh} accounts for leakage paths parallel to the junction. Ideally, R_S is minimized to reduce voltage drops and R_{sh} is maximized to minimize leakage currents. Including these resistances, the diode equation becomes:

$$J = J_0 \left[e^{\left(\frac{q(V - JR_S)}{AkT}\right)} - 1 \right] + \frac{V + JR_S}{R_{sh}} - J_{ph} \tag{1.43}$$

JV is done under two conditions, when the cell in the dark and when the cell is exposed to light. The light curve is measured while the cell is under Air Mass 1.5 (AM1.5) intensity, which is the standard spectrum used for profiling PV performance for terrestrial applications and corresponds to a spectral intensity of 100 mW/cm^2. JV measurements presented in this work were performed at First Solar's California Technical Center (CTC) in Santa Clara, California using two different custom-built systems for superstrate and substrate excitation, where superstrate measurements were performed using standard methods.

The substrate system was developed by the author at CTC for the purposes of this thesis work. The system is composed of a xenon arc lamp solar simulator which provides the AM1.5G spectrum and a source-measure unit to supply a working bias and measured output current. Measurement consistency and speed was increased by integrating three single-axis linear motors where the x- and y-axis motors position the cell of interest under illumination and the z-axis motors houses the contact probes. Stage movement, data collection, and analysis are all handled by a LabView program written by the author. The sample stage and solar simulator are housed within a light-tight enclosure to prevent ambient light from interfering with the measurements. The system is shown in Figure 1.13.

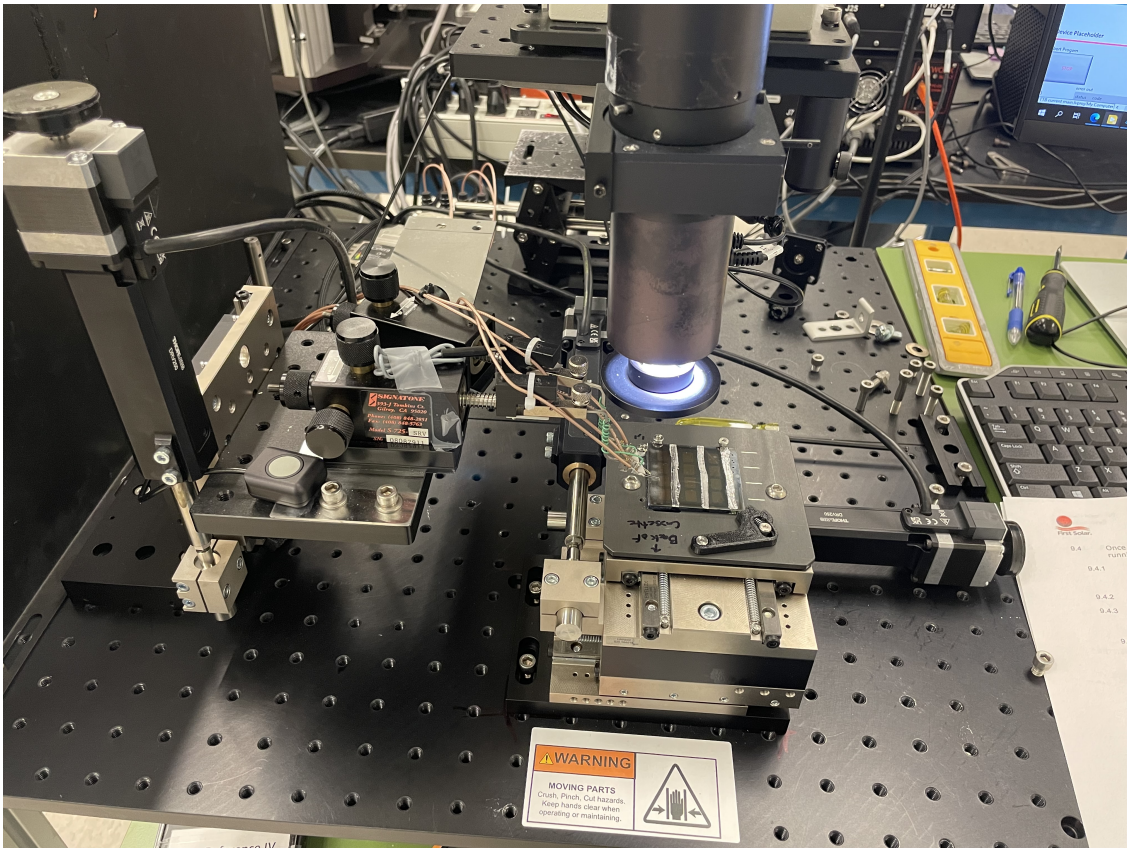

Figure 1.13: Set up of the substrate JV measurements system outside the light tight enclosure.

Basic operation was simplified down to loading the sample on the x-y stage and running the LabView program. When the program is started, the x-y stage moves into it's "home" position, which was defined such that the first cell within the 12 cell device is under illumination (this considers that the sample has the standard layout defined through the laser scribe process) and the probe stage drops to hover the contacts roughly 10mm above the sample surface. A prompt asks the user the ensure alignment is correct, where the stage can be controlled by the user to ensure the probes are aligned with the cell. Once the user is satisfied, the program will begin measurements, first by lowering the probe stage to make contact to the cell, measuring JV, then lifting the probe stage and moving the x-y stage a distance defined by the spacing of each cell before lowering the probe stage again and repeating this. Dark and light measurements were done in the same manner, with the only difference being that a shutter was used within the light path for dark measurements.

1.5.2 Capacitance-Voltage Measurements

CV profiling is a useful technique of modeling the active region on our solar cell as a parallel plate capacitor. This model allows the extraction of carrier density across the depletion width of the absorber and assumes we have a one-sided junction, that our depletion width is less that of our film's thickness, that our material only has shallow defect states, and that our back contact barrier is negligible. CV profiling gives an accurate order of magnitude for our carrier concentration and a good overall estimate of depletion width. Our model begins by assuming charges residing on the depletion edges, with a capacitance given by

$$C = \frac{\epsilon\epsilon_0 A}{W} \tag{1.44}$$

where ϵ is the dielectric constant of the material, ϵ_0 is the permittivity of free space, A is the area of the device, and W is the depletion width, itself given by

$$W = \left[\frac{2\epsilon\epsilon_0(V_{bi} - V)}{qN_{dp}}\right]^{1/2} \tag{1.45}$$

where q is the elementary charge, V is the bias voltage, and N_{dp} is the carrier density within the depletion width.

1.5.3 Quantum Efficiency

The quantum efficiency (QE) of a solar cell is defined as the ratio between the number of collected electrons to the number of incident photons as a function of wavelength. Spectral QE provides insight into losses in short circuit current as well as quantitatively providing the short-circuit current by the formula

$$J_{sc}(QE) = q \int_0^{\text{inf}} (QE) N_{ph}(\lambda) d\lambda \tag{1.46}$$

where QE is the measured ratio, usually between zero and one, and $N_{ph} = \frac{\lambda P(\lambda)}{hc}$ is the spectral photon flux density is dependent on the solar spectral irradiance density P(λ). This measurement can provide critical information on current losses due to absorption issues for specified wavelengths. Losses can occur due to reflections off of the front glass interface, absorption within the front glass plane, TCO, or emitter layers before reaching the active layer, incomplete absorption within the active layer, and finally due to recombination of photo-generated charge pairs within the active layer, all of which would result in decreased QE intensity at specific wavelengths. The bandgap can also be estimated based on the tail end of the QE curve, where higher wavelengths, and thus lower energy photons, are not able to excite electrons across the bandgap. This is formalized by observing at which wavelength dQE/dλ is maximized as shown in Figure 1.14

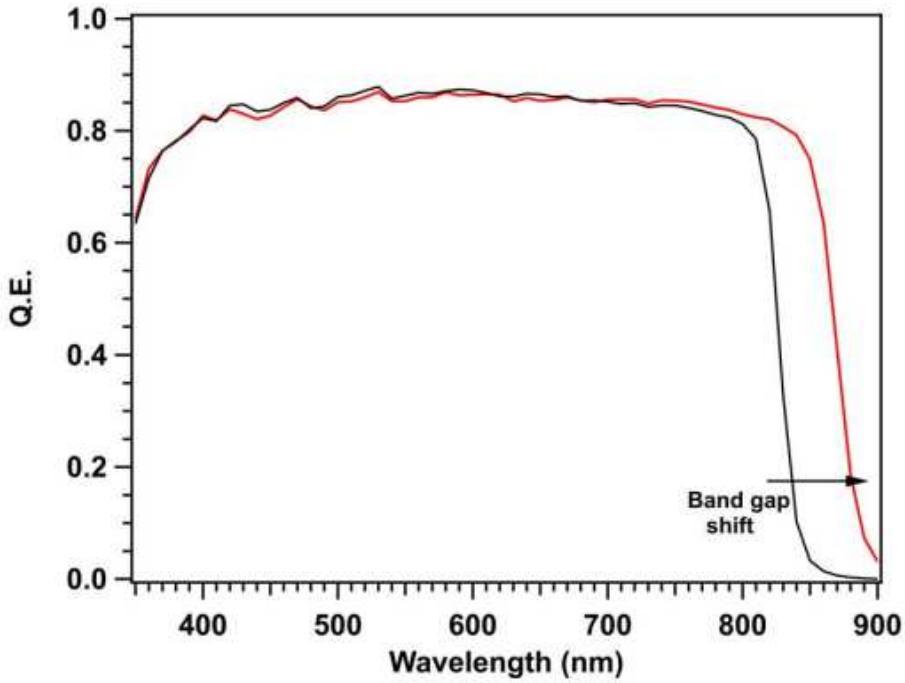

Figure 1.14: Example QE demonstrating the differences in bandgaps.

1.5.4 Steady-state Photoluminescence

PL is focused on the spectral analysis of the emitted light from the device resulting from photo induced radiative recombination. This spectral profile will consist of mainly band-to-band radiative recombination, in addition to conduction-band-to-acceptor-state, donor-state-to-valance-band, and donor-state-to-acceptor-state transitions. The resulting spectral image with be a broad Gaussian peaking at the band gap with a peak intensity proportional to the number of charge carries radiatively recombining across the bandgap. Other peaks within the PL spectrum are representative of other transition energies, with their peak intensities also correlating to the number of charge carries recombining across that transition state. The choice of probe is determined by the material you wish to probe, with larger wavelengths penetrating deeper into the material.

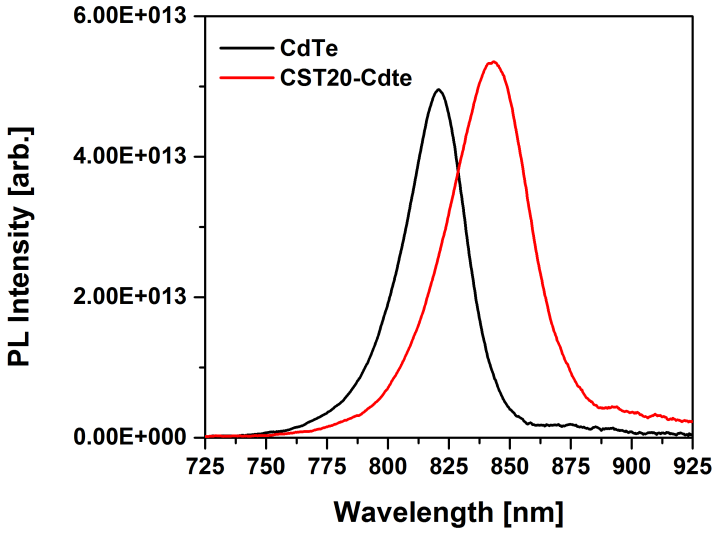

Figure 1.15: Example of a typical PL graph from CSU. Note the difference in bandgap, as given by peak location, for the CdTe absorber versus that with the graded CST20-CdTe absorber.

1.6 CdSeTe Solar Cells

Throughout this section, the terms CdTe and CdSeTe may be used interchanably, with an understanding that processes historically developed for use in binary CdTe absorbers and devices translates adequately to the ternary CdSeTe system. This section will review the typical fabrication processes and devices structures used in modern CdTe PV devices.

The primary reasons for CdTe's success is due to its near ideal bandgap (E_g) and high absorption coefficient (>1 X 10^4 cm^{-1}) which allows for the absorption of >99% of photons with energy E>E_g within a few microns of material. This allows fabrication of "thin-film" photovoltaics which are much cheaper and faster to manufacture than their crystalline counterparts.

Additionally, the bandgap of CST can be modified as a function of the concentration of Se in the lattice, conventionally determined using a bandgap bowing formula as

$$E_g(x) = (1-x)E_g(CdSe) + xE_g(CdTe) - bx(1-x) \tag{1.47}$$

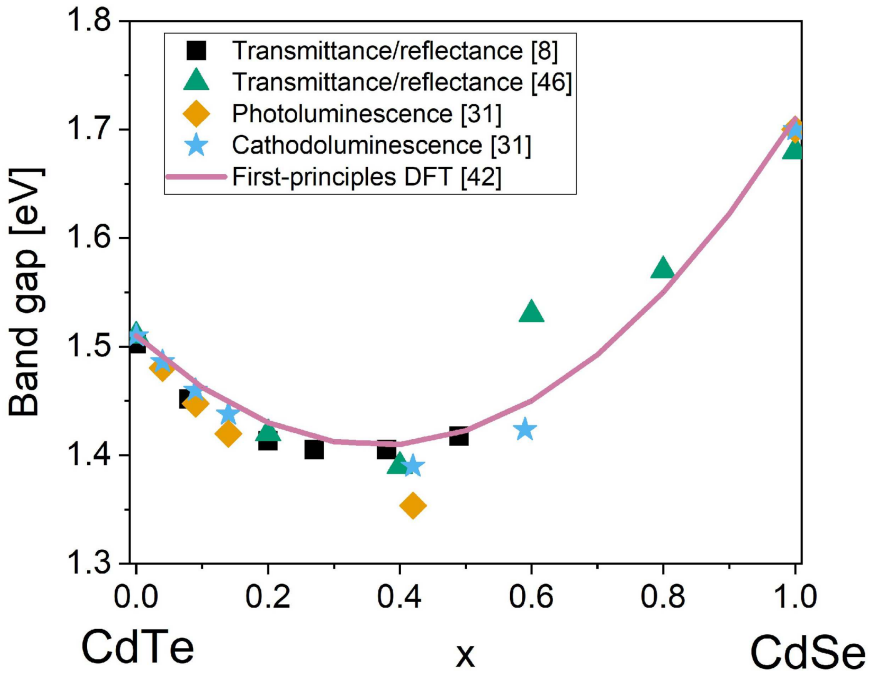

Figure 1.16: Bandgap for various compositions of $CdSe_xTe_{(1-x)}$ based on the bowing equation.

where b is the bowing coefficient (determined through a fit of the equation to empirical data, typically 0.75 - 1.25) x is the compositional fraction, $E_g(x)$ is the band gap of the alloy with stoichiometry x, and E_g(CdTe/CdSe) is the bandgap of pure CdTe ($\approx$ 1.50 eV) and CdSe ($\approx$ 1.72 eV). This results in a bandgap of $\approx$ 1.40 eV for a composition of x = 0.3, which is ideal for single junction devices, as shown in Figure 1.16.

This reduced bandgap allows for the absorption of lower energy photons near the front interface, which would otherwise be transmitted through the device, thus increasing the short circuit current (J_{sc}). This increase in J_{sc} more than compensates for the small losses in open circuit voltage (V_{oc}) and fill factor (FF) associated with decreasing the bandgap, as shown in Figure 1.10. Additionally, the use of Se alloying has shown to increase the carrier lifetime and thus the diffusion length of carriers with CdSeTe, which is critical for improving the overall efficiency of the device.

Doping of CdTe and CdSeTe has historically been accomplished with group-I elements such as copper (Cu) where p-type conversion was achieved through substitution with Cd (Cu_{Cu}) acting as an acceptor defect. However, Cu is known to be highly mobile within the CdTe lattice, resulting in diffusion from the back contact region where a large density of holes is desired, and leading to the

formation of Cu_i interstitial defects which act as donor states in the bulk, thus reducing the overall p-type conductivity and potentially forming unwanted junctions within the bulk. Additionally, use of copper doping appeared to result in a limited acceptor density on the order of 10^{14}.

More recently, group-V doping with elements such as arsenic (Ar), phosphorus (P), and antimony (Sb), has been shown to have better stability and produce higher acceptor concentrations on the order of 10^{16} in CdTe and CdSeTe. In this case the acceptor defect is a result of a group-V substitution for the group-VI Te site (group-V_{Te}). Despite the increased acceptor density however, increases in the open-circuit voltage (V_{OC}) has not been commiserate with this fact. The reasons for this remain debated and is an active area of research which will be discussed in more detail in Chapter 2 and Chapter 3.

1.6.1 Fabrication of CdSeTe Devices

Modern CdSeTe absorbers make use of a selenium gradient, rather than a uniform ternary (unitern) stoichiometry throughout the bulk. A majority of the Se is desired to be near the front contact (glass side), where initial absorption and photogeneration occurs, with a decreasing concentration, and thus an increasing bandgap, towards the back contact. One function of this gradient is to reduce nonradiative recombination at the front contact by creating a built-in potential which can help to separate holes towards the back contact. Additionally, it has been recently appreciated that CST tends to be n-type conductive with a greater Se stoichiometry, which will be discussed more thoroughly in Chapter 3, thereby strengthening the np-junction near the TCO/window interface with CST.

The formation of a graded Se profile is typically achieved through a two-step process. First, a thin layer of CST (x = 0.3–1) is deposited, followed then by a thicker CdTe layer. The Se near the front interface is then allowed to diffuse into the bulk of the absorber, creating a graded bandgap profile.

CdSeTe thin-films can be fabricated in a variety of methods, with a few example fabrication techniques shown below in Figure 1.17. Within this work, most CdTe samples were fabricated

by First Solar using vapor transport deposition (VTD). VTD, a form of physical vapor deposition, operates by heating of the constituent materials (CdTe and any in-situ dopants desired) to a vapor phase which is then transported to the substrate of choice by an inert carrier gas. VTD techniques allow rapid fabrication of thin-films along a linear path, even in open air. At Colorado State University, close-space sublimation (CSS) is the primary method of fabricating CdTe thin-films. In CSS deposition, the CdTe material is housed within a container, typically graphite, which is heated above the vapor pressure point for a given operating pressure and referred to as the source. The substrate for deposition is positioned above the source and held at a temperature below the source, allowing the sublimed CdTe material to recondense and form a thin-film.

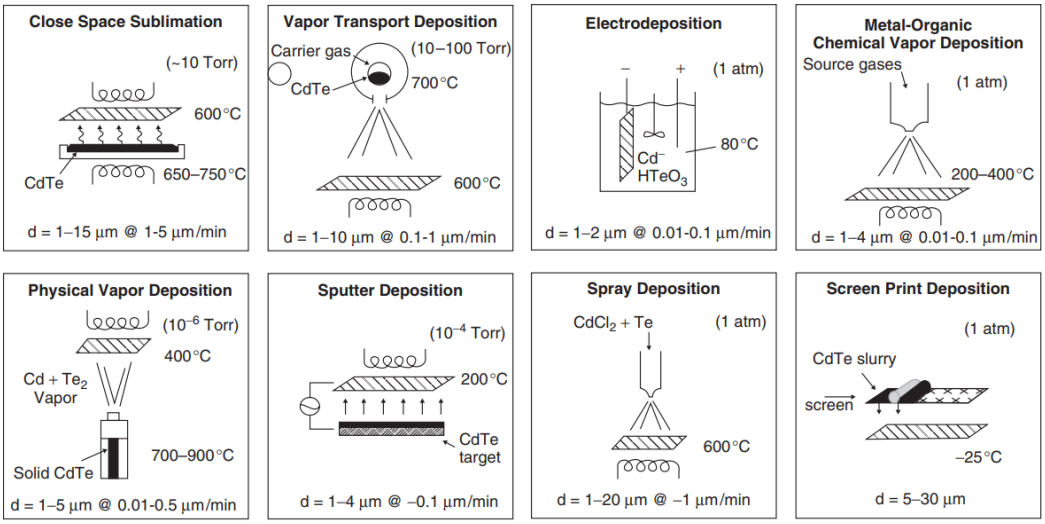

Figure 1.17: This graphic demonstrates 8 different fabrication techniques for depositing thin-film cdTe. The typical deposition thickness and deposition rates are listed at the bottom of each technique. CSS is one of the quickest methods for deposition.

CdTe is typically deposited onto glass which contains a thin film of optically transparent fluorine doped tin oxide (FTO) as a polycrystalline material. FTO operates as a front contact as it is a high bandgap oxide and thus optically transparent, as well as being highly conductive, making it a transparent conductive oxide (TCO). Most photogenerated carriers are created close to the front contact, where light is initial absorbed, thus it is critical for the front contact region to have a low

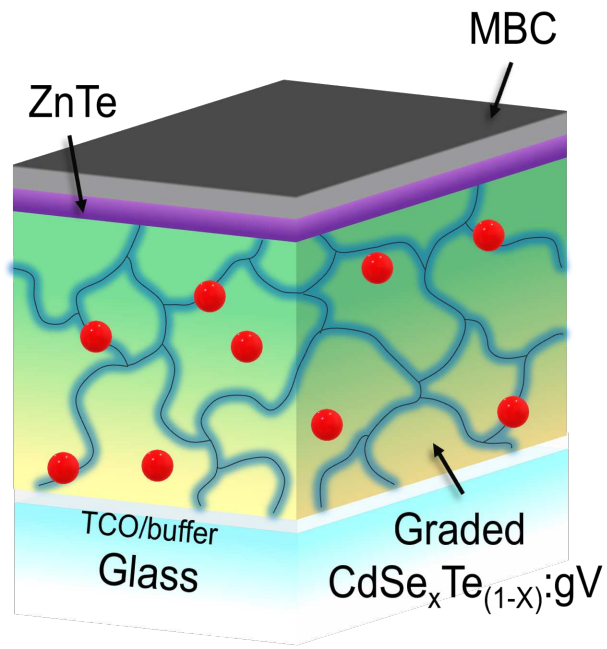

Figure 1.18: Representation of a completed CdSeTe device used within this work. The device is composed of a glass substrate, TCO/buffer layer, a graded Se CdSeTe absorber, a p-type ZnTe transport layer, and metallic back contact.

recombination rate, yet be ohmic to electrons. This is typically done by deposition of an n-type semiconductor to create a built-in potential, which is the emitter layer in the case of CdTe.

An ideal emitter layer in thin-film CdTe would be highly n-doped, optically transparent, and easily fabricated. $Mg_xZn_{1-x}O$ (MZO) has a large bandgap (E_g > 3.3 eV) which allows a large portion of the solar spectrum to be transmitted while being energetically compatible with CdTe. MZO has a tunable bandgap which can be modified by shifting the alloy's elemental content, similar to CST [8–10]. MZO is typically deposited using radio frequency (RF) sputtering, which allows for the deposition of high quality thin-films with a high degree of control over the stoichiometry and thickness. The use of MZO as an emitter layer has been shown to improve the overall efficiency of CdTe solar cells by reducing recombination losses at the front contact and enhancing charge collection.

Post-deposition passivation is essential for achieving high-performance CdSeTe devices [11]. The polycrystalline nature of vapor-deposited CdSeTe films results in grain boundaries that act

as recombination centers, limiting device efficiency. Chlorine passivation, achieved through heat treatment with $CdCl_2$, serves multiple critical functions: it reduces stacking faults, promotes grain growth and reorientation [12], and provides thermal budget for selenium diffusion from the front interface into the bulk CdTe region. This thermal process creates the desired graded bandgap profile while simultaneously improving the electronic quality of the absorber through grain boundary passivation.

Chlorine passivation, referred to as a chlorine heat treatment (CHT), can be achieved in a variety of manners. At CSU, CHT is achieved through CSS of $CdCl_2$ onto the CdTe free surface immediately following CdTe deposition without breaking vacuum. After allowing the plate to rest and cool to room temperature, the residual $CdCl_2$ film is removed with a deionized water rinse. Within this work, a majority of the CHT was done using a wet method, whereby $CdCl_2$ is dissolved in water and the solution is spin-coated onto the surface of the CdTe. This is then followed by annealing to diffuse Cl into the CdTe and finished by rinsing of residual $CdCl_2$ on the surface.

While CdTe has many ideal properties for use as an absorber, it is not without its drawbacks. The most notable of these is the fact that CdTe is a p-type semiconductor, meaning that the majority carriers are holes. Extraction of these holes from the can be problematic, as it is understood that CdTe has a relatively large work function (Φ = 5.7 eV), and the formation of an ohmic metallic contact with p-type semiconductors typically requires a metal with a larger workfunction (electrons(holes) will flow from(into) the metal into(from) the semiconductor). As such, a metal with a very large work function is required to avoid creation of a Schottky barrier [13]. A number of metals of interest are listed with their tabulated work functions in Figure 1.19.

Material	Work function (eV)
Au (gold)	5.1
Cu (copper)	4.7
Cr (chromium)	4.5
Al (aluminum)	4.0–4.28
Ni (nickel)	4.1–5.0
Ti (titanium)	3.84
Pt (platinum)	5.65

Figure 1.19: Tabulated work functions for various metals. Note that Au and Pt, the two metals which are closest to forming ohmic contacts, are also the most scarce and expensive metals.

As is seen, metals with sufficient work function are nonexistent, and those with work functions which approach the required energy (>5 eV) are scarce and expensive rare earth metals (Au and Pt). We thus expect a Schottky barrier to form at the back contact with a barrier potential energy defined by

$$\Phi_B = \frac{E_g}{q} + \chi - \Phi_m \tag{1.48}$$

where Φ_B is the barrier height, E_g is the bandgap of the semiconductor, χ is the electron affinity of the semiconductor, and Φ_m is the work function of the metal. For example, when contacted with Au (Φ_m = 5.1 eV), we find a barrier height of 0.6 eV, which is large enough to prevent the flow of holes into the metal contact.

In order to reduce this barrier height and facilitate efficient hole transport, a hole transporting layer (HTL) can be employed. HTLs used in CST have typically consisted of a p-type zinc telluride (p-ZnTe) which is well latticed matched to CdTe with a work function of roughly 5.3eV and a bandgap of 2.26 eV. Using p-ZnTe at the back interface of CdTe promotes upward band bending, facilitating transport of holes out of CdTe, and creates a large conduction band offset (CBO) which functions to prevent the flow of electrons and thus reduce back surface recombination. In this work, p-ZnTe is deposited at First Solar by sputter coating onto the CdTe surface.

Following the formation of the HTL, a metallic back contact is deposited. Within this work, two varieties of back contacts are explored. A metallic back contact (MBC), which is fully opaque but highly conductive, is composed of a nickel alloy and deposited by thermal evaporation. A novel transparent back contact (TBC), which is less conductive but optically transparent, is composed of a multilayered TCO stack (engineered by First Solar) and evaporated by sputter coating.

Chapter 2

Group-V Doping in CdSeTe

2.1 Introduction

Group-V doping in CdSeTe is a critical area of research aimed at improving the p-type conductivity of this material. Group-V elements, such as nitrogen (N), arsenic (As), phosphorus (P), antimony (Sb), and bismuth (Bi), are known to act as p-type dopants by substituting group-VI elements (Se and Te) in the lattice. This substitution creates acceptor states that can increase the hole concentration in the material (referred to as "active" dopants), thereby improving p-type conductivity.

The motivation for investigating group-V doping in CdSeTe stems from the need to overcome the limitations of current p-type doping methods. Other p-type dopants, such as group-I elements (e.g., copper), often result in low hole concentrations on the order of 10^{14} cm^{-3} due to poor solid solubility and demonstrate poor stability due to the high mobility of Cu in CdTe [14]. Group-V elements, on the other hand, have been shown to form shallow acceptor levels and achieve hole density on the order of 10^{16} cm^{-3}, which is sufficient for high efficiency devices [15, 16]. Group-V doped devices have also demonstrated greater long term stability, which is critical for field deployment [17].

However, substitution of group-V dopants for Se or Te ($\mathrm{gV}^{+}_{Se/Te}$) is not guaranteed simply through the incorporation of the dopant into the lattice. The formation of various point and complex defects may act to compensate active dopants, thereby reducing the overall hole density [18–20]. The formation of these "inactive" defects all contribute to the low activation of group-V dopants, resulting in only a small fraction of the incorporated dopants contributing to the desired p-type conductivity. This is typically defined by a dopant activation ratio as

$$\text{activation ratio} = \frac{\text{[Acceptor defects]} - \text{[Donor defects]}}{\text{[Dopants in lattice]}} \tag{2.1}$$

where the difference between acceptor and donor defects should be greater than one for p-type conversion. This ratio is typically less than 10% for group-V dopants in polycrystalline (px-) CST [15,21], which is significantly lower than the >50% activation ratios observed in single crystal CdTe [20]. While the exact mechanism for this low activation is still debated, it is clear that the formation of defect complexes and the presence of other impurities in the lattice play a significant role.

This chapter will focus on the use of group-V doping in CST absorbers for p-type conversion. First, processing conditions required to fabricate high efficicny (>15%) devices will be reviewed, providing information on potential limiting factors in group-V doping. Following this, the impact of overdoping will be examined through comparative studies of identical devices with various levels of group-V dopant incorporation. Finally, a novel method intended to increase dopant activation through physiochemical modification of the lattice reorganization will be reviewed.

2.2 Processing Group-V Doped CST for High-Efficiency Devices

Before examining novel processes intended to increase group-V activation, a review of the "baseline" processing conditions required to achieve high efficiency (>20%) devices is presented. The purpose of baselining is to establish conditions under which high efficincy group-V doped devices can be achieved, which will be used to compare the impact of novel processes intended to increase group-V activation.

This chapter will focus on arsenic (As) and phosphorus (P) as the group-V dopants. Arsenic is first used to establish the baseline processing conditions as it has been more well studied within the community and remains an important dopant. Following the establishment of baseline conditions for >20% devices, the focus will shift to phosphorus. The reason for switching to phosphorus is due to the fact that the most recent record efficincy device from First Solar used phosphorus as the group-V dopant [4] and the factors which limit phosphorus activation are less well understood.

2.2.1 Overview of processing steps

Absorbers used in this study, supplied by Fist Solar, are composed of a bialyer of thin CdSe (0.3 μm) and CdTe (3 μm) deposited by vapor transport deposition (VTD) onto a TCO/buffer coated glass. Absorbers are ex-situ doped with group-V dopants on the CdTe surface prior to a post-deposition anneal in chlorine similarly as has been reported before [22], shown schematically in Figure 2.1.

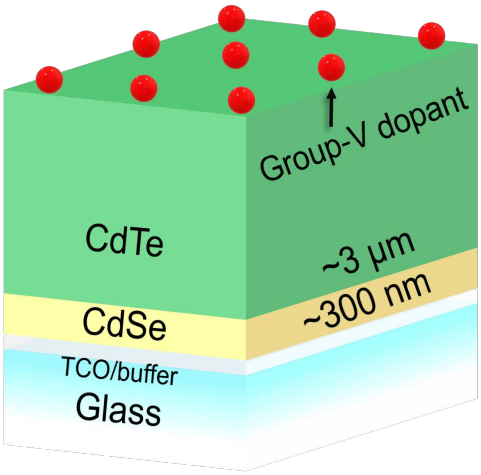

Figure 2.1: Diagram of the as-received bilayer absorbers with ex-situ group-V doping.

In order to diffuse Se and group-V dopants to form a graded bandgap with uniform distribution of dopants during recrystallization, absorbers are given a post-deposition chlorine treatment, referred to as the chlorine heat treatment (CHT). The absorber is coated with an aqueous solution of $CdCl_2$ and heated to 400-500°C for 5–60 minutes. This creates a eutectic point in the Cd-Te-Se-Cl system which lowers the melting point, resulting in a recrystallization. During this recrystallization, defects can be reduced, and Se and Cl are driven into the absorber and grain boundaries (GB) respectively. The Se diffusion results in a graded stoichiometry of $CdSe_XTe_{(1-X)}$, which creates a bandgap gradient increasing from the CdSe to the CdTe side. This process is depicted in Figure 2.2.

Ex-situ group-V dopant diffusion and activation occurs during the CHT step as well. The As or P is incorporated into the surface of the as-deposited CST layer prior to CHT and then diffused throughout the absorber during CHT, as depicted in Figure 2.2. Dopant activation is promoted

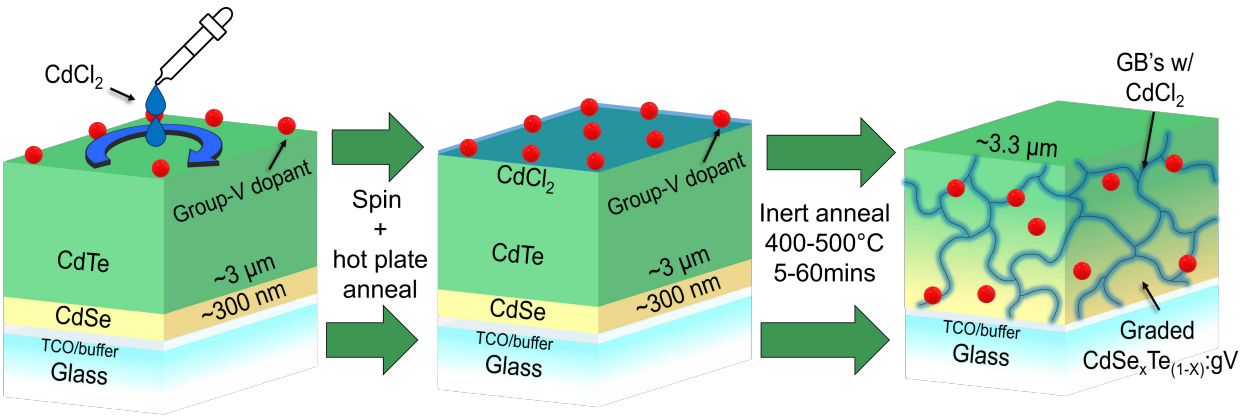

Figure 2.2: $CdCl_2$ is spin-coated onto the CdTe surface with an aqueous solution and then annealed in open air on a hot plate to remove residual solvents. The absorber is then placed in a crucible and annealed in a linear tube furnace. This results in the recrystallization of the absorber, the diffusion of Se, Cl, and group-V dopants, and the formation of a graded bandgap. The preferential diffusion of Cl along grain boundaries is represented by the colored grain boundries, and group-V dopants are thought to diffuse throughout the absorber.

during this diffusion, where dopant atoms may fill Se or Te vacancies ($V_{Se/Te}$) or outright substitute such sites, resulting in active arsenic or phosphrous in Se/Te sites ($As/P_{Se/Te}$). This methodology, as opposed to an in-situ doping during absorber deposition, allows flexibility to explore significant factors contributing to higher dopant activation ratios, such as changing the annealing temperature and/or time to increase species diffusivity, creating an overpressure of Cd to further promote Se or Te vacancies, or changing the annealing environment to alter the surface chemistry during reflux.

Following the CHT/dopant activation step, absorbers are integrated into PV devices by the formation of a hole transporting layer (HTL) of p-type ZnTe and completed by contact metallization, typically using an opaque back contact, referred to as the metallic back contact (MBC), or a semi-transparent back contact stack, known as the transparent back contact (TBC). A representation of a completed device using MBC and its operation under excitation is shown Figure 2.3.

The CHT and group-V dopant activation steps discussed in this work are performed within a linear tube furnace, which will be referred to as the "furnace" and is shown in figure Figure 2.4. Optimization is explored through variations in the processing gasses, pressure, the annealing temperature and time, and the annealing crucible itself. The critical processing changes which resulted in >20% efficient devices are now reviewed.

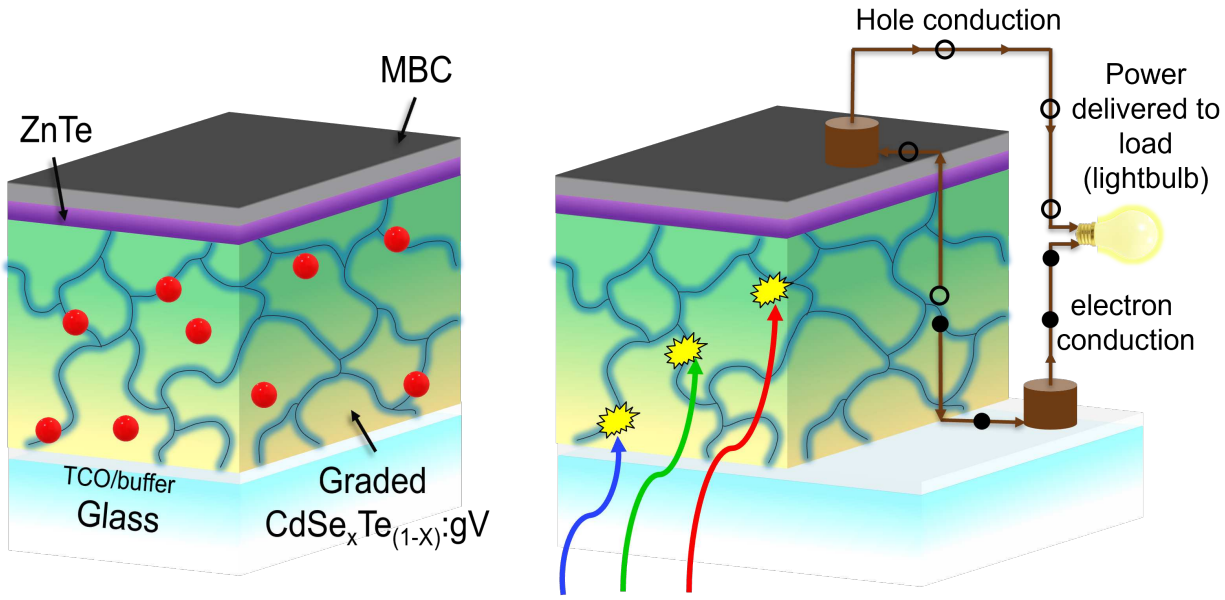

Figure 2.3: Example of completed CST devices discussed here. Operation occurs in superstrate configuration (glass side illumination) where a majority of charge pairs are generated near the glass side where the built-in field exists. Electrons (solid circles) are conducted along the TCO while holes (open circles) are conducted through the ZnTe and MBC to be delivered to a load (represented by lightbulb) for useful work.

Figure 2.4: Furnace used in CHT and group-V activation steps showing the magnetic transfer arm, load lock, and processing chamber. Interior of load lock showing graphite crucible sitting on end effector of the MTA.

2.3 Significant Factors Enabling >20% As-doped Devices

This section will be focused on the factors which significantly alter arsenic doped device performance. This begins by using conditions informed from prior experience, initally holding the $CdCl_2$ coating and arsenic doping constant (both arbitrarily referred to as "high" dose in this case) and varying the annealing parameters. Initial tests made use of the best known method (BKM) for CHT of CdSe devices, which consists of a 20-minute anneal at 475°C with a mixture of 80% oxygen (O_2) and 20% nitrogen (N_2) at 500 Torr within a quartz crucible which was used for CdSe work. Following the post-deposition chlorine anneal, absorbers were integrated into identical devices as described in Section 2.2.1. These samples were compared to a control device using an absorber which was in-situ As-doped during VTD growth by First Solar and recieved a CHT in a separate system than the furnace used here.

This initial condition was quickly found to be problematic for these absorbers, and subsequent work to reduce oxygen exposure during CHT enabled devices with upward of 16% efficiency. The variables which resulted in the most significant changes in device performance were the annealing environment and the crucible used, both of which are potential sources of oxygen during CHT. As the oxygen content was removed from the annealing environment and the quartz crucible was switched for a graphite crucible with less historic oxygen exposure (and further cleaned and seasoned) devices steadily improved. The trends in device performance along with examples JV and CV results for these devices are shown below in Figure 2.5. Device performance improved for each step intended to reduce the oxygen exposure during CHT. V_{OC} and J_{SC} both steadily improve, with J_{SC} for the device from the cleaned graphite crucible nearly reaching its theoretical limit. CV trends provide insight into the consequence of oxygen exposure, where N_a is less than $1x10^{16}$ cm^{-3} before work was done to scrub the oxygen.

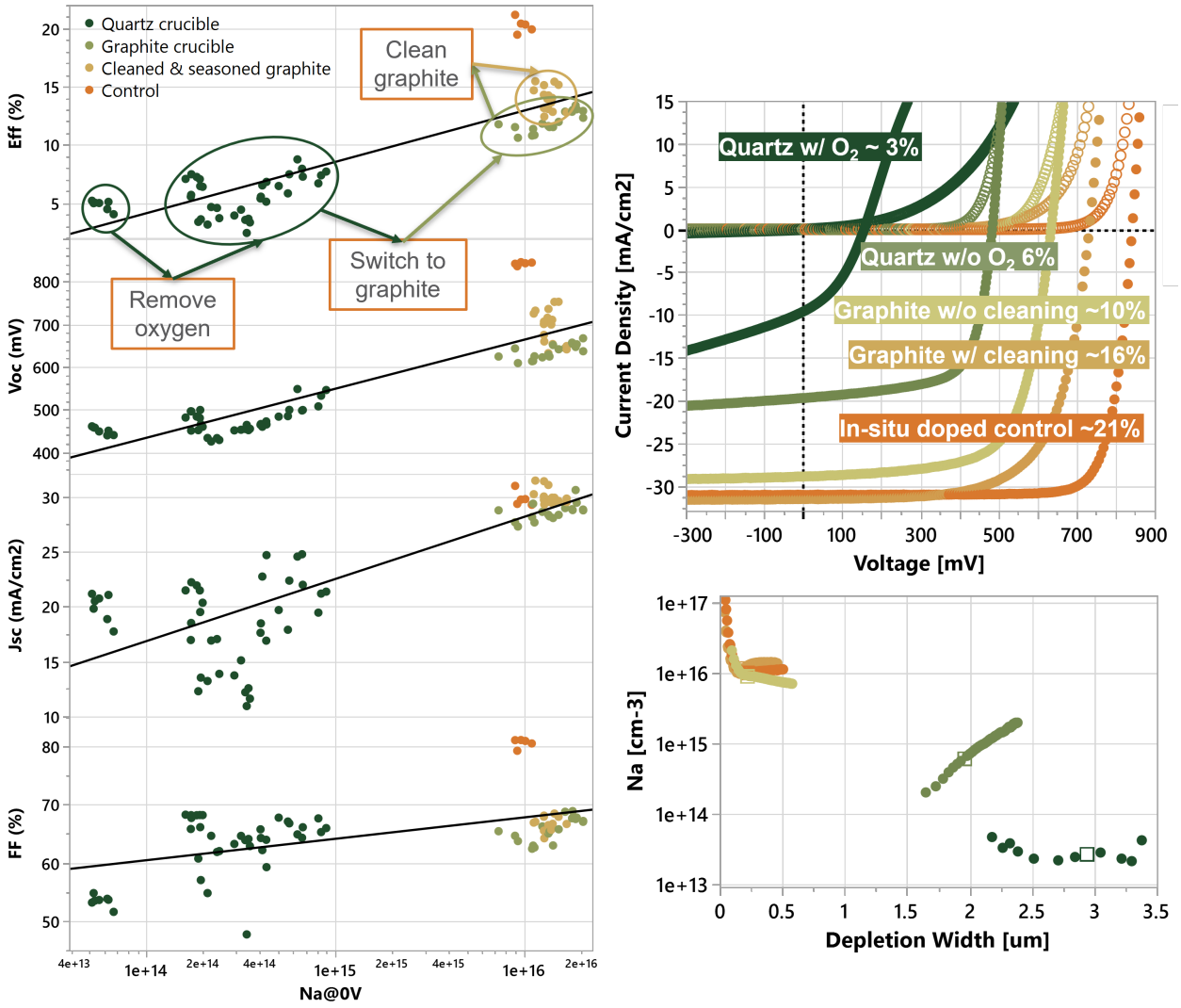

Figure 2.5: JV parameters alongside example JV and CV curves for devices with absorbers annealed under various conditions. A control device, using an in-situ As-doped absorber from First Solar in dark orange, is shown for comparison.

Additional insight is gained from the photoluminescence (PL) spectrum for these devices, shown in Figure 2.6. For the initial condition, the PL peak emission of 1.42 eV is slightly higher than the desired 1.4 eV, likely due to poor Se diffusion during CHT, in addition to a distinct defect emission near 1.25 eV, likely due to poor arsenic incorporation into the CST lattice or possibly an oxygen related defect. By switching to a graphite crucible which had minimal exposure to oxygen and using the same processing conditions as the previous 0% oxygen anneal, the PL peak emission was reduced to 1.4 eV and a broad shoulder defect on the low energy side, characteristic of As_{Se}

defects, is observed. The graphite crucible was then cleaned of debris and annealed in an inert environment with 0% oxygen at 500°C for 3 hours with $CdCl_2$ coated CST dummy samples, a process refered to as "seasoning" the crucible. Absorbers from the cleaned and seasoned graphite show a further reduction in the peak bandgap to below that of the control. This may be due to an excessive incorporation of As into the lattice, which would increase the magnitude of the subgap defect emission. This indicates that the initial "high" dose of As may be excessive.

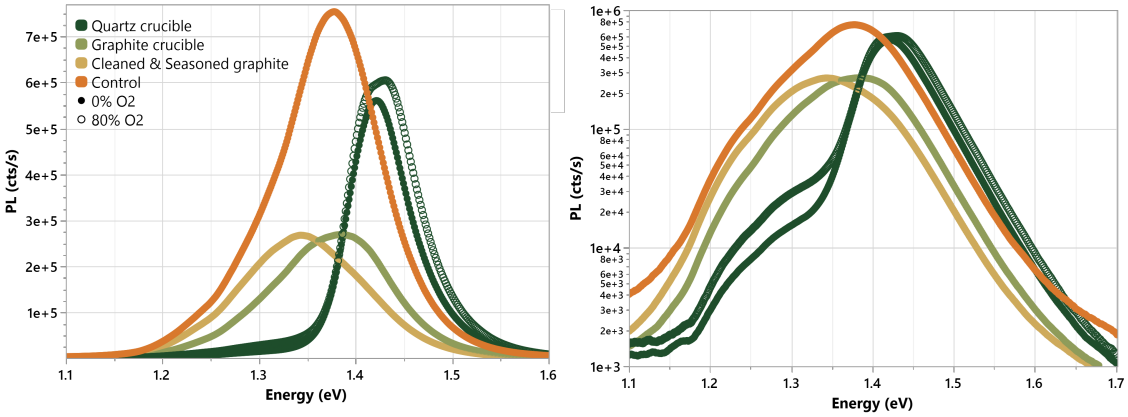

Figure 2.6: Glass side photoluminescence (PL) spectra of absorbers from each of the anneal conditions discussed.

These intial results indicate that oxygen exposure during CHT is a significant factor in limiting performance, particularly in the ionic incorporation of As into the CST lattice. The impact of oxygen exposure on group-V dopant activation will be further explored in the following section.

2.3.1 Impact of Oxygen Exposure on Dopant Activation

Secondary ion mass spectroscopy (SIMS) was used to quantify the concentration of arsenic, oxygen, selenium, and chlorine present in the devices with >5% efficiency from above, with results shown in Figure 2.7. From this we see that device performance tends to increase along with the concentration of As incorporated in each device. The concentration of oxygen appears larger in the initial graphite annealed sample, but this may be a result of the exact region being sampled, and additional measurements need to be made to confirm this. Se distribution is seen to increase

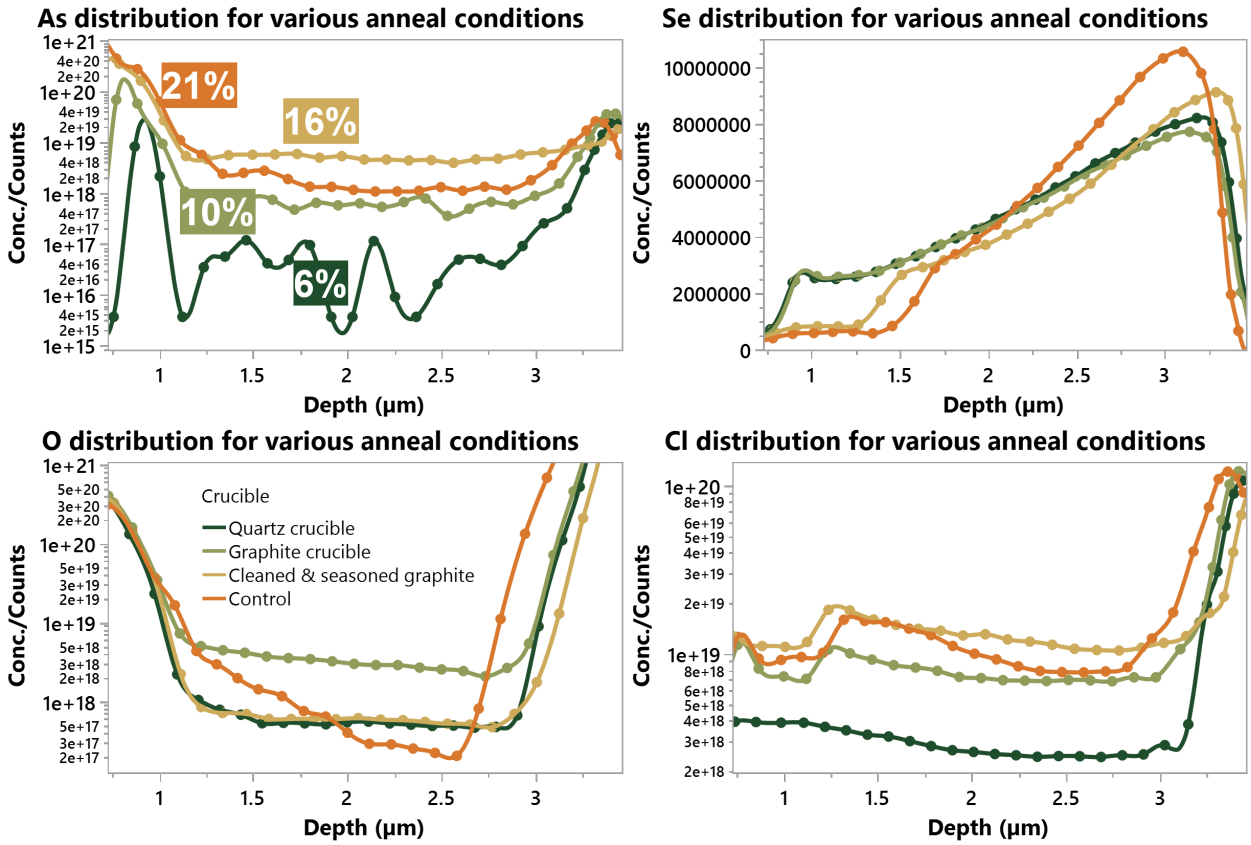

Figure 2.7: DSIMS of arsenic, oxygen, selenium, and chlorine profiles for absorbers with various annealing conditions compared to in-situ doped control device in dark orange. Depths indicated here increase from the back to the front (towards TCO) of devices.

towards the front of the device for all annealing conditions as expected for a diffused Se bilayer device. However, the two lower performance devices show a much higher fraction of Se near the back surface, whereas the higher performance device shows a similar drop in Se as the in-situ doped control device. Additionally, Cl distribution appears uniform throughout the bulk and has the lowest concentration for the lowest performance device. These results indicate that the incorporation of both As and Cl, in addition to the diffusion of Se near the exposed back surface during CHT annealing is sensitive to the crucible used and potentially to its history of oxygen exposure.

Using the As data from SIMS and the acceptor concentration from CV measurements, an estimate of the activation energy for each device shown above can be determined. This is shown in a bar chart in Figure 2.8, where the ratio of As to oxygen from SIMS is also included for each

crucible condition. The trends in activation may seem misleading at first, where the highest activation is seen for the 10% rather than the 16% device, but the As/O ratio may reveal why this is. By reducing the residual oxygen levels in the annealing crucible, the incorporation of ionic arsenic becomes more effective, as seen by the roughly 2 orders of magnitude increase in acceptor density from the first device to the second and third. Given that each of these three devices received the same dose of arsenic doping, the low ratio of arsenic to oxygen in graphite vs the cleaned and season graphite device suggests that a significant fraction may be coordinating with oxygen, resulting in a reduced concentration measured in SIMS and thus an inflated activation ratio calculation.

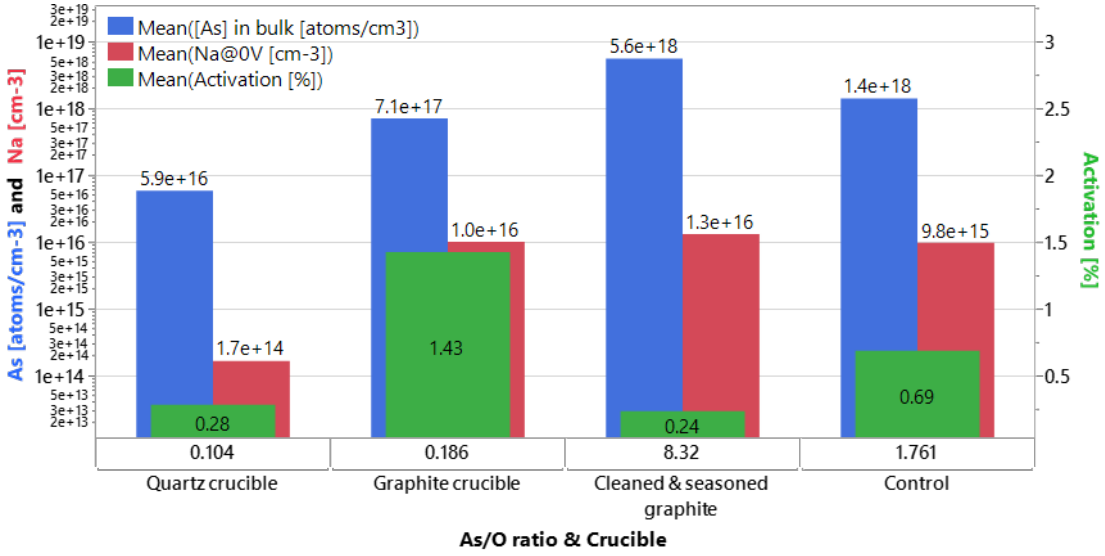

Figure 2.8: Activation ratio for each device as determined by the acceptor concentration at 0V bias from CV and the bulk concentration of arsenic from DSIMS.

While devices with 16% efficiency have been demonstrated through optimizing the annealing process, the doping activation remains quite low. This suggests that the arbitrarily chosen "high" dose of arsenic doping may be excessive, whereby there is a greater concentration of arsenic being incorporated than can effectively substitute Se or Te, leading to an overdoping effect. This is further supported by the quantum efficiency (QE) spectrum for these devices, shown in Figure 2.9. The 16% device shows a larger negative QE gradient towards the bandgap than the control device, symptomatic of overdoping. Examining the Urbach energy from sub-bandgap emission also indi-

cates overdoping, where the Urbach energy is seen to increase for devices as the As concentration from SIMS increases. This is likely the source of the approximately 100 meV V_{OC} loss in the 16% device relative to the control.

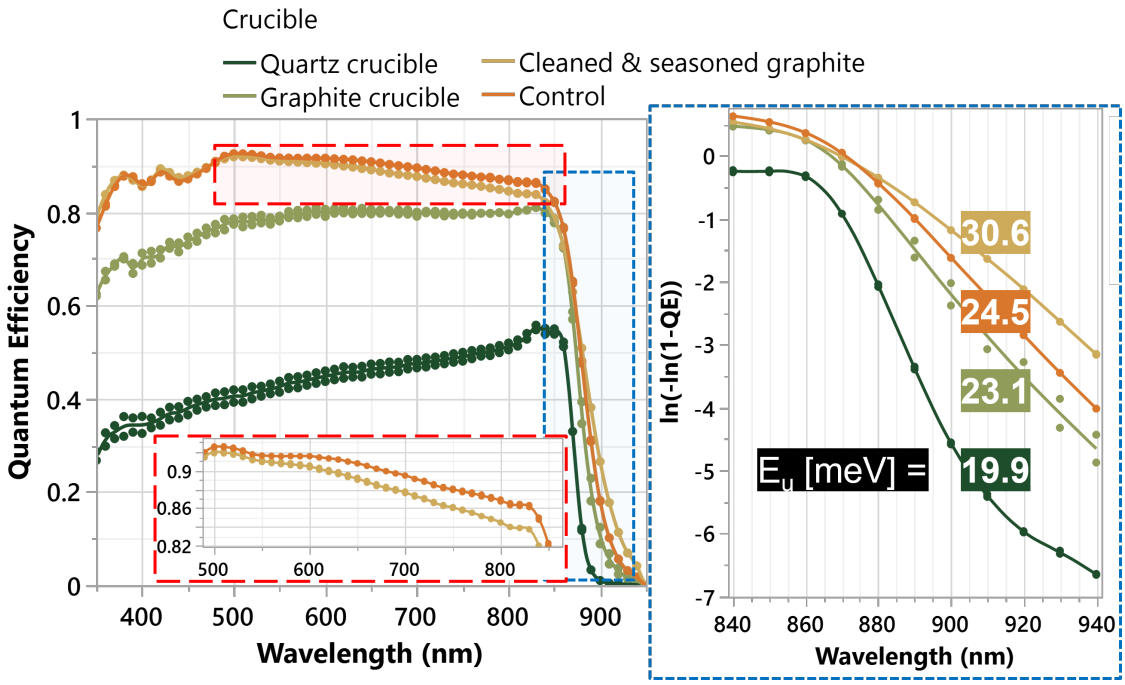

Figure 2.9: QE spectrum for each device with an inset figure focusing on the differences between the 16% device and the control. Figure to the right focuses on the sub gap emission with the Urbach energy for each listed.

2.3.2 Impact of Changing Ex-situ Dopant Concentration

Considering the apparent increase in nonactive dopants and their impact on increased lattice disorder seen for the best devices previously, an evaluation of reducing the concentration of ex-situ doping was performed. The same dopant concentration used previously, referred to as the "high" dose, is compared to absorbers with a "low", "medium", or "none" (intrinsic CST) dose of As. Dopant diffusion is achieved with the same CHT process as devices with >15% efficiency from above, that is by spin-coating aqueous $CdCl_2$ onto the absorber surface and annealing inside a graphite crucible at 475°C in an inert atmosphere at 500 torr for 20 minutes, followed by rinsing with water to remove residual $CdCl_2$.

Photoluminescence of each absorber, measured with either film-side or glass-side injection, provides insight into the impact of changing the dose of As incorporated into each device. The bandgap from peak PL emission is expected to be near 1.5 eV on the film side where CdTe dominates and 1.4 eV on the glass side where a majority of $CdSe_XTe_{1-X}$ is thought to reside with X around 0.15. However, samples with As doping all show a decrease in peak emission from the film side and an even greater deviation on the glass side as shown in Figure 2.10.

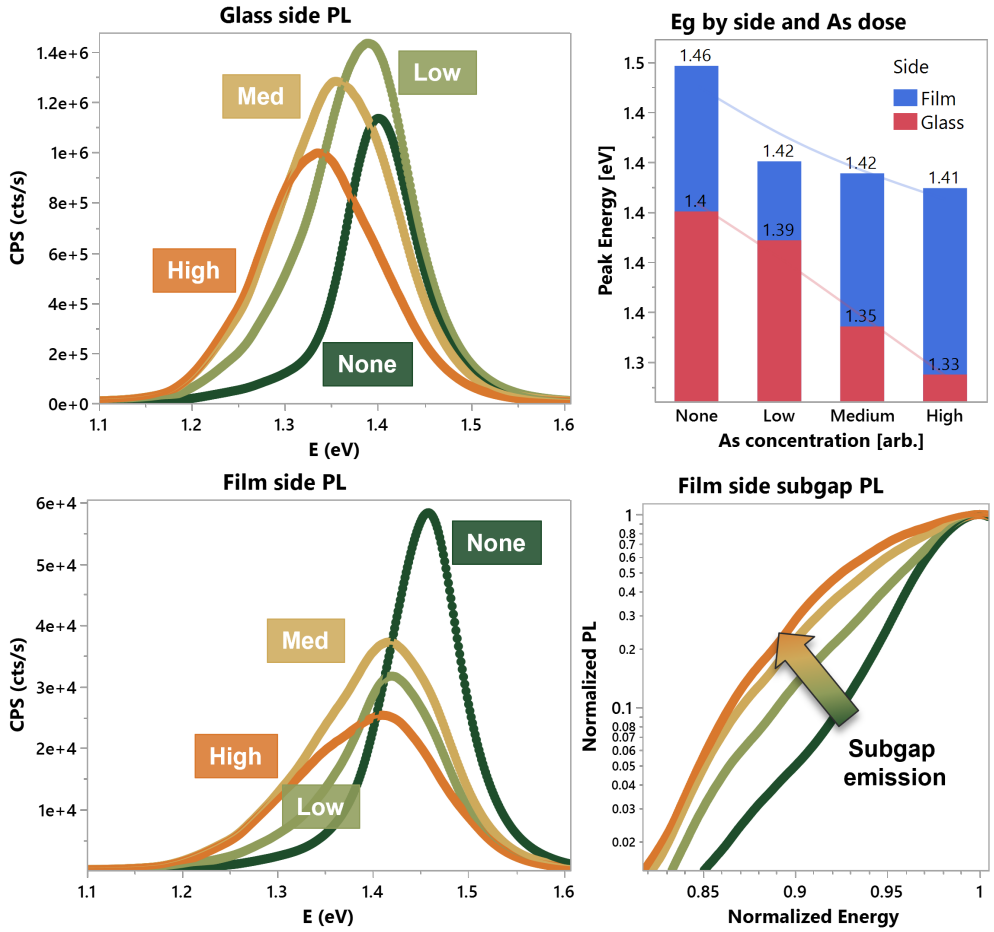

Figure 2.10: PL measured from film-side and glass-side of CST absorbers with various concentrations of As dopant. Peak energy location is shown for each curve, with the film side peak energy shown in blue and the glass side peak energy shown in red. The extent of subgap emission is focused on for the film side emission.

This shift may be a consequence of the increased concentration of non-active As defects, which act to increase the Urbach energy and thus reduce the effective bandgap. By normalizing each

curve to intensity and peak energy location from the film side, it is seen that the emission for subgap states increases with the concentration of As.

TRPL for each absorber is shown in Figure 2.11. The lifetime of carriers is seen to increase linearly from none to medium As incorporation, but dynamics change when we go to the high As dose. Initial decay is seen to be slower, but the long time decay is much faster, indicating that the majority of the carriers are recombining non-radiatively. Ultimately, the medium dose of As absorber shows the longest average lifetime close to 2.5 ns.

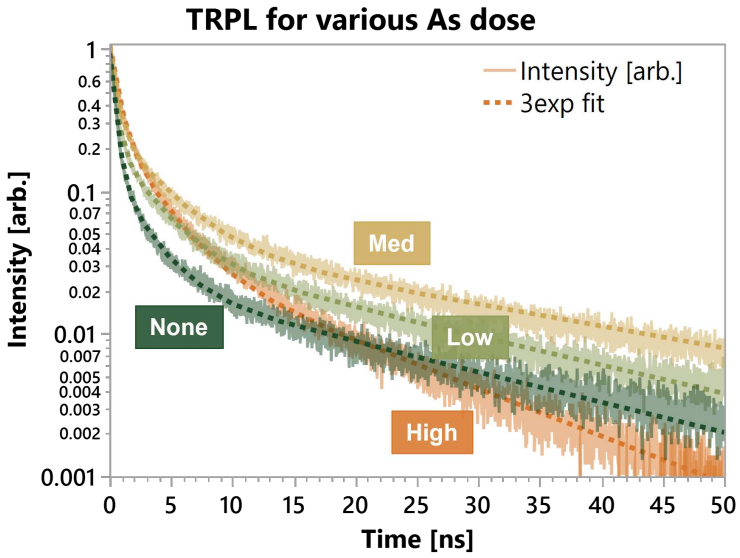

Figure 2.11: Measured TRPL for each absorber with three exponential decay fits. The average lifetime is calculated from the fit parameters and is shown in Table 2.1.

Table 2.1: TRPL parameters fit using $I_{PL} = \Sigma\, A_i e^{-t/\tau_i}$. Average lifetime calculated as $\tau_{ave} = \Sigma \frac{(A_i \tau_i)}{(A_i)}$.

Dose	A_1	τ_1 [ns]	A_2	τ_2 [ns]	A_3	τ_3 [ns]	τ_{ave}
None	0.79	0.41	0.12	2.46	0.02	20.6	1.17
Low	0.72	0.46	0.18	3.01	0.04	21.8	1.81
Medium	0.74	0.55	0.22	3.66	0.05	28.6	2.51
High	0.76	0.63	0.26	2.79	0.04	13.1	1.63

All absorbers were then integrated into devices using identical device structure and processing conditions as described in Section 2.2.1. The devices were then tested for JV, QE, and CV performance with example JV results shown in Figure 2.12. The intrinsic CST device (none dose) shows the worst performance with extermely low J_{SC} and V_{OC} <500 mV, but this is expected based on the understanding of the intrinsic n-type conductivty of CST absorbers, which is explored further in Chapter 3.

High As dose device shows similar performance to what was previously seen, with high J_{SC} near 30 mA/cm^2, but low V_{OC} <700 mV and fill factors <70%, both symptomatic of overdoping. The low dose device shows a similar J_{SC} with an increased V_{OC} near 750 mV and fill factor of 79%. The medium dose device shows the best performance with a V_{OC} near 840 mV, J_{SC} near 30 mA/cm^2 and fill factor of 78%.

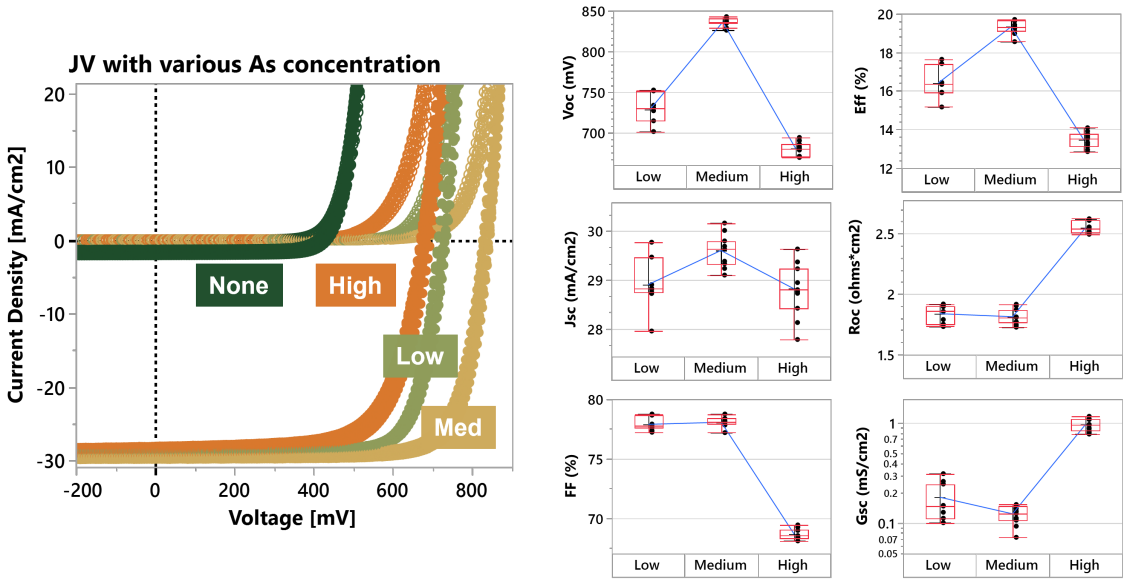

Figure 2.12: JV curves for each concentration of As dopant, with the parameters shown to the right.

To understand what factors may be limiting the performance based on each dopant dose, CV and QE analysis was performed on each device. QE and CV measurements for these devices are shown in Figure 2.13. This shows that the carrier concentration increases with increasing As doping, from roughly 1 x 10^{16} cm^{-3} for the low dose to 3 x 10^{16} cm^{-3} for the high dose

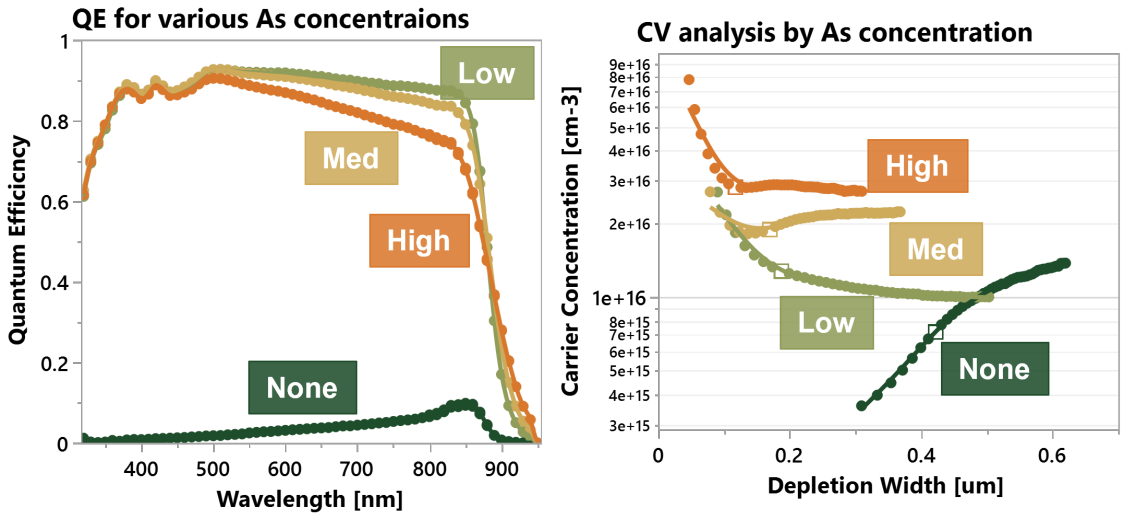

Figure 2.13: Example QE and CV curves for each device with various concentrations of As dopant. Differences in the measured acceptor density for each doping level is neglgibly different, indicating a reduced dopant activation in these devices.

device. However, it should be noted that the high dose is not simply 3x the dose of the low dose. Rather, the high dose is at least 10x the concentration of the low dose, indicating that the increased concentration of As in this device is leading to an increased concentration of non-active dopant related defects.

From QE, it is apparent that the high energy shoulder decreases with increasing As dosage while the extent of band tailing increases, where the calculated Urbach energy is significantly higher (36.5 meV) than that of the low (23.6 meV) and medium (28.5 meV) doses. Both of these observations reinforce the notion of overdoping in the high As dose devices. Of all extrinsically doped devices, the low As dose is the only one to demonstrate $E_u < kT$ ($\approx$ 26 meV), indicating minimal disorder introduced through nonactive defects [23, 24]. The intrinsic device also shows a very low Urbach energy ($\approx$ 18.0 meV), which is close to the expected values for single crystal absorbers and indicates that the increased band tailing seen in group-V doped devices is a consequence of dopant related defects.

Additionally, the bandgap seen in QE is roughly the same for each extrinsically doped device (E_g(Absorption) $\approx$ 1.4 eV), which is at odds with the band gap calculated from PL emission. This is likely due to the fact that the PL emission is dominated by the subgap emission, where charges

may be relaxing into defect states before transitioning to the conduction band radiatively. This results in a stokes shift [25] between the emission and absorption spectrum of ≈ 17 meV, 47 meV, and 62 meV for the low, medium, and high As doses respectively, consistent with the increased Urbach energy measured in QE.

All of this put together indicates that the low As dose should be optimal, despite initially showing lower performance that the medium dose. However, it was later seen in repeat tests that the low and medium As doses can achieve similar V_{OC} greater than 80 mV, J_{SC} greater than 29 mA/cm^2, and FF above 75% (>80% in case of low As) as shown in Figure 2.14. The lower V_{OC} initially seen may be due various factors including the exact absorber used in such device or any unnoticed deviations in the device integration and scribing processes. QE, CV, and PL for these repeat tests are in line with those seen prior, where low dose As device shows lower Urbach energies, high dopant activation ratios, and reduced radiative recombination compared to the medium dose device.

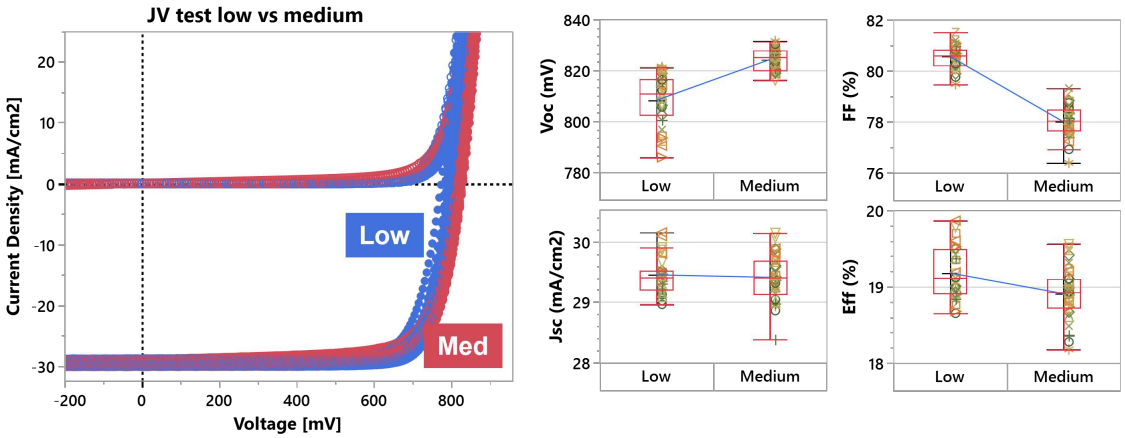

Figure 2.14: Repeat tests of the low vs medium dose of As in devices shows that the low dose can achieve a slightly efficiency approaching 20%.

This demonstrates the influence of device performance with respect to the concentration of group-V dopants used. All devices tend to show the same range of acceptor concentration–around 10^{16} cm^{-3}–with minimal gains seen for increasing the dopant concentration. Indeed, further increases to dopant concentration tends to reduce device performance by increasing radiative recom-

bination. So, while the acceptor concentration is high, there are still potential drawbacks related to incorporation of As even at the "low" level (As $\approx 10^{17}$ cm^{-3} indicates <5% activation). In the next section, a novel process intended to increase group-V dopant activation will be explored. The intent of this is to allow further reduction in the concentration of group-V dopants required to achieve high acceptor density by reducing the concentration of nonactive defects which may be related to oxidation of the dopant.

2.4 Novel Processing to Increase Dopant Activation

The presence of oxygen in CST devices is ubiquitous due to the use of transparent conductive oxides (TCOs) and buffer layers such as magnesium zinc oxide (MZO). However, the role of oxygen and the extent to which it diffuses in CdTe and CST has a complicated history. First generation CdTe devices, using a CdS buffer layer without Se alloying, appeared to benefit from oxygen exposure in-situ during growth [26, 27]. Recent advances in techniques to study the front interface, where oxygen is more likely to be present, have shown that the formation of oxidized nanolayers at the front interface may indeed be beneficial to device performance through the formation of a passivated interface, but this remains an active area of research [28]. In the same study, it was seen that group-V dopants also experience oxidation at the front interface, but again the consequence of this is debated. However, this observation raises the question whether group-V dopants are being oxidized within the bulk under certain processing conditions, and to what extent this oxidation may play a role in the low activations observed.

This thesis proposes a method to prevent or reduce group-V oxidation by introducing "oxygen getters" to the CST system. In this context, oxygen getters are elements which have a higher affinity for oxidation relative to the dopant atom (arsenic in this case), and thus "get" the oxygen rather than the dopant. Oxygen getters may also act as reducing agents if in proximity to As-O complexes, stripping the oxygen from As. The effectiveness of any given oxygen getter is dependent on the relative concentrations of oxygen and dopant atoms, their proximity to each other and oxygen

within the system, and various processing conditions such as the annealing temperature and time and ambient composition and pressure.

2.4.1 Selection of Oxygen Getters for Increased Dopant Activation

To determine appropriate elements to act as oxygen getters, an Ellingham diagram is consulted. The Ellingham diagram, shown below in Figure 2.15, displays the required partial pressure for oxidation of a given element to occur. Under a given environment, elements with a lower required partial pressure will oxidize first, thereby preventing the oxidation of other elements such as the group-V dopant. This informs the selection of various getter elements including zinc (Zn), silicon (Si), aluminum (Al), and magnesium (Mg) used here for reduction of As or P oxides.

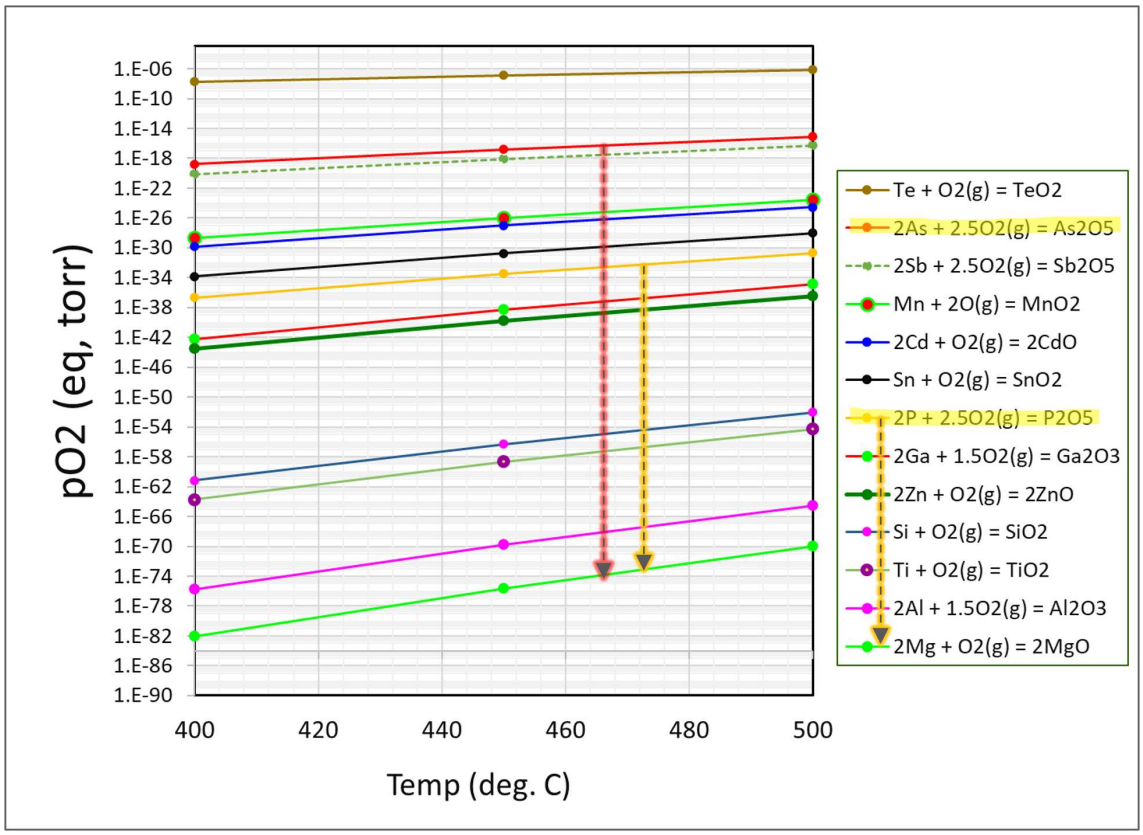

Figure 2.15: Ellingham diagram of required partial pressure of oxygen for oxidation to occur for a given temperature. The lower an element is on the chart, and thus a lower required partial pressure is for oxidation, the more likely they are to oxidize relative to elements above.

2.4.2 Introduction of Oxygen Getters to CST

Given that the role of oxygen getters is to oxidize preferentially to group-V dopants, their incorporation into the CST lattice as unbound elements is important. This is achieved through ion implantation, through which clusters of the target elements bombard the CST surface. This forces Cd-Se-Te bonds to break and allows implanted ions to penetrate into the bulk. The depth which ions implant into the bulk is a function of the ion's mass and the energy and angle respective to the surface normal at which bombardment occurs.

Following implantation, the same CHT process described above is performed. In addition to the typical benefits from CHT (grain growth, species diffusion, passivation, etc.) it is expected that the surface lattice damage induced by implantation can be repaired and that the implanted oxygen getters can diffuse through the bulk and react with oxygen.

2.4.3 Results of Oxygen Getter Study

In this section, the group-V dopant used is phosphorus (P) instead of arsenic. This selection is based on the higher propensity for phosphorus to oxidate relative to arsenic, and therefore it is reasonable that the principles of interactions between phosphorus and oxygen may be applied to arsenic. The reproducibility of P-doped devices with >20% efficiency using the same CHT conditions in the furnace as described above was confirmed prior to the study of oxygen getter use.

Following implantation and CHT, all absorber were made into identical devices as described previously. A summarization of results from various getter implantation experiments is presented here. Example JV, QE, and CV curves with the distribution of primary parameters are shown in Figure 2.16.

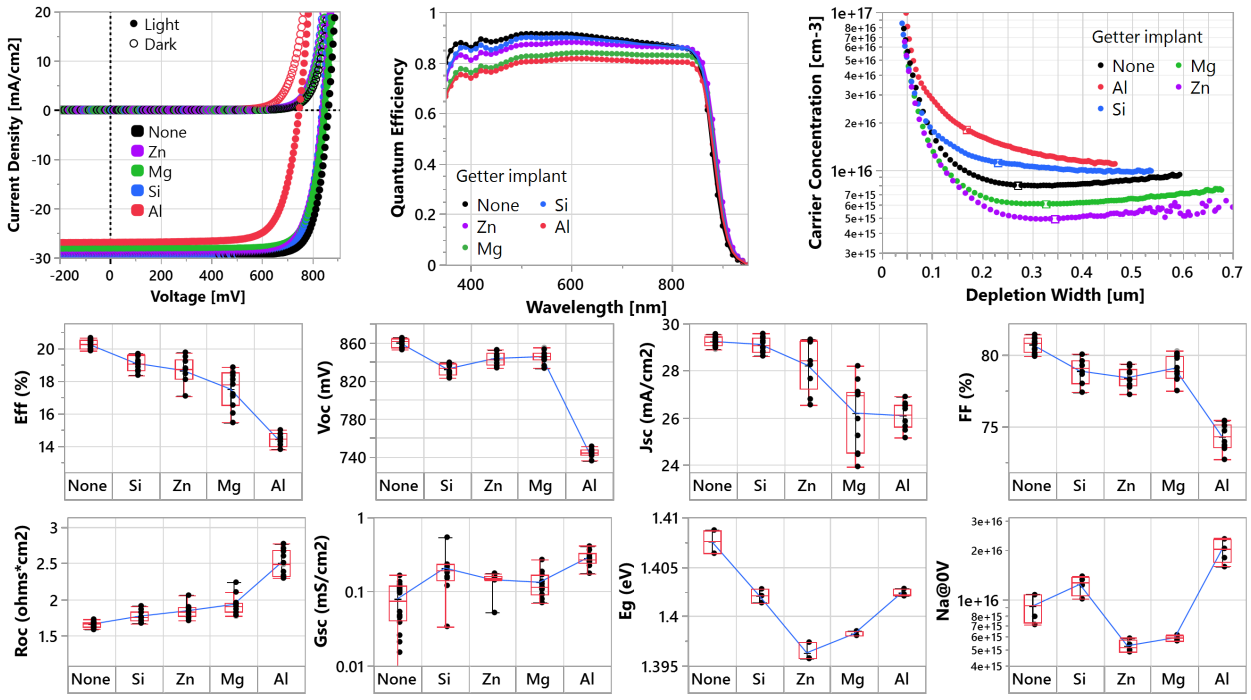

Figure 2.16: Representative JV, QE, and CV for each getter implant compared to a standared control sample. The distribution of main parameters for each device is shown below.

Of all getter implants, Al stands out as a detriment to device performance, particularly due to a reduction of V_{OC}. One possible explanation for this is the formation of Al_{Cd} defects, which may act as donor defects in CdTe, albeit this sample also shows the largest carrier concentration from CV. Beyond this, there is an increased resistance for all getter implanted devices, seen in both the series resistance (R_{OC} here) and the shunt conductance (G_{SC} here). This suggests that additional disorder introduced through the implantation process may not be fully repaired during the CHT process. However, all devices show quite low Urbach energies ($E_u \approx 21.4 \pm 0.48$ meV), indicating that the majority of the defects are benign and do not significantly impact the optoelectronic properties of the absorber.

Taking the best and worst performing oxygen getter samples (Si and Al implantations respectively) can help to understand the impact of these processes. SIMS data of relative Al and Si counts for each device following implantation, alongside a control example, is shown in Figure 2.17. This shows that the ion implantation process was successful in incorporating getter elements near the

surface, at a depth roughly 200±100nm from the back surface of CdTe, as expected based on simulations [29]. Given that Al is a lighter element than Si, it is expected to implant slightly deeper than Si, as is found to be true.

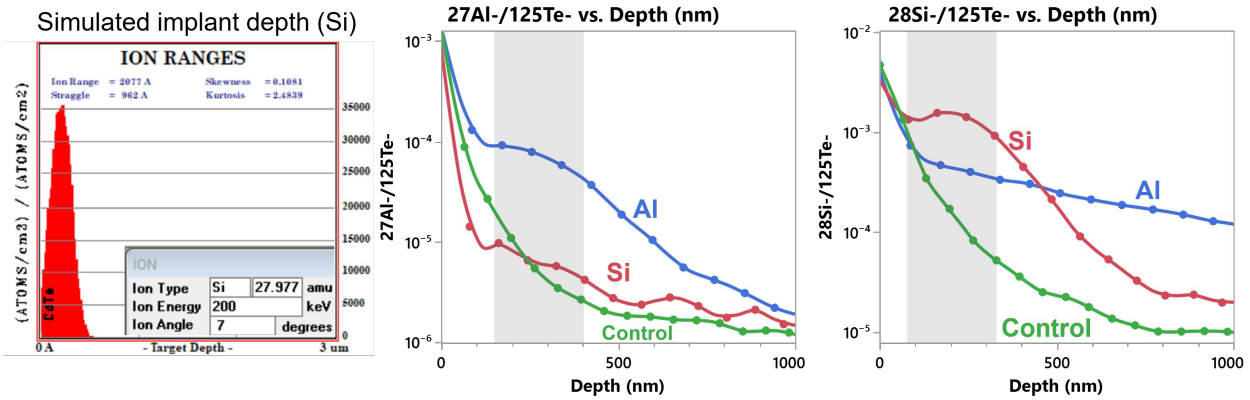

Figure 2.17: Simulation of Si ion implantation, calculated using SRIM (Stopping Range of Ion Motion) software, indicates an expected implantation depth of 200±100 nm from the CdTe surface. SIMS analysis for Si and Al implanted devices, compared to an unimplanted control (green), indicate that each getter implant was successfully incorporated at the expected depth.

Following CHT and device integration, completed devices were again analyzed with SIMS to determine how the oxygen getters impacted the distribution of oxygen and phosphorus used as the group-V dopant. Additionally, a relative count of phosphorous oxide was determined using PO_3 signal, for which a unique charge to mass ratio was identified. Example SIMS of P and O concentration for each Si and Al getter implanted device (best and worst performers) and their respective control devices is shown in Figure 2.18.

Si and Al getter devices show a distinct increase in [P] near the back interface, which is where implantation occurred, with a subsequent reduction in [P] near the front interface, where the depletion region is expected to exist. This is likely due to an interaction between the implanted getter and the P dopant, which may have reduced the diffusivity of P during the CHT. Oxygen getter implanted devices show a semi-Gaussian distribution of [O] at the back interface which is not seen in the control devices. This seems to indicate that Si and Al do in fact act as getters during CHT. This

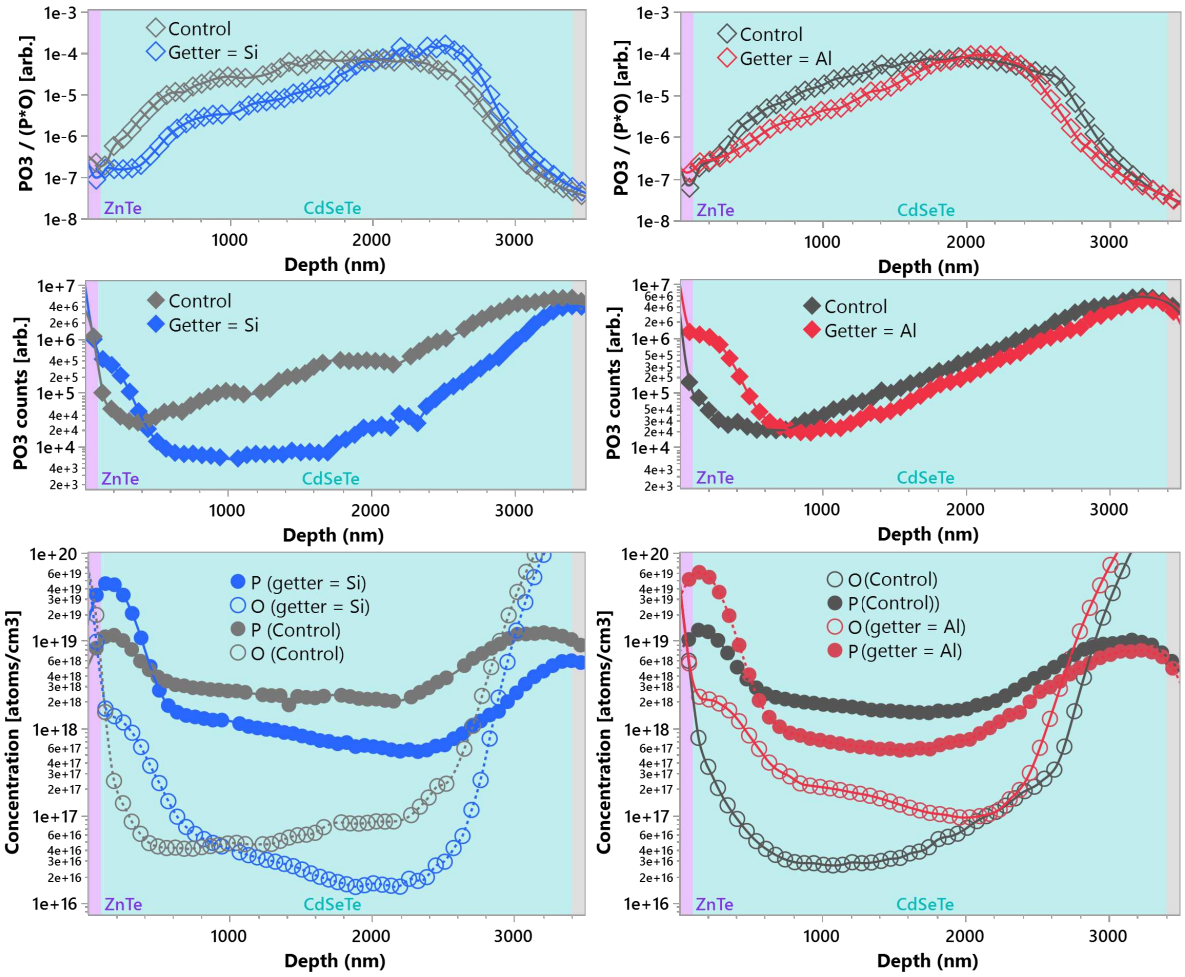

Figure 2.18: DSIMS profiles of [P] and [O] for Si or Al implantated devices compared to their control devices. The raw and normalized counts of PO_3 are shown above.

is further supported by an increased [O] profile throughout the bulk for the Al getter compared to the Si getter, where Al is expected to be a stronger getter than Si according to Figure 2.15.

The increase in [P] and [O] at the front interface of getter devices is reflected in the PO_3 profile, as would be expected. However, when normalized to the counts of P and O, both Si and Al appear to be more effective at reducing the formation of PO_3 relative to the control devices throughout the bulk. The increased concentration of constituent atoms at the front interface did not result in a proportional increase in PO_3 formation. The increased [O] at the front for both Si and Al, and throughout the bulk in Al case, may be due to a result of oxidation of the getters themselves. However, measurements of AlO_2 or SiO_2 were inconclusive, and further analysis is needed to confirm this.

2.5 Conclusions

Optimization of the CHT process for group-V doped devices demonstrated that oxygen exposure during device processing may present an unexpected hindrance to group-V doping activation. Additionally, the use of excessive doping was shown to reduce device performance due to an increased presence of nonactive defects which are prone to radiative recombination. By optimizing the processing conditions for CST devices, a baseline performance of $\approx$20% efficiency with dopant activation ratios 3±1% was established. The use of oxygen getters was shown to reduce the concentration of free oxygen measured in SIMS and appeared to reduce the formation of group-V oxides relative to the availability of constituent components. A summary of the activations for each getter implanted device is shown in Table 2.2. The activation ratio is calculated from the SIMS data of [P] and the CV data of N_a averaged for each device.

The activation ratio for Si and Al getter devices is significantly higher than their respective control devices, indicating that the use of getters has indeed increased the activation of group-V dopants. However, Zn and Mg getter devices appear to have a lower activation than their respective control, which itself had a larger activation ratio than the other two control devices. More work using Mg or Zn as oxygen getters is required to understand this. Furthermore, while devices

Table 2.2: Mean phosphorus concentration, acceptor density, and activation ratio for various devices

Device	[P] in depleted region (atoms cm^{-3})	Mean N_a (cm^{-3})	Mean Activation (%)
Control 1	2.2×10^{18}	9.1×10^{15}	0.4
Si implant	5.9×10^{17}	9.1×10^{15}	2.1
Control 2	1.6×10^{18}	1.5×10^{16}	0.6
Al implant	6.0×10^{17}	2.1×10^{16}	3.5
Control 3	4.9×10^{17}	9.1×10^{16}	1.8
Mg implant	5.1×10^{17}	5.8×10^{15}	1.1
Zn implant	8.4×10^{17}	5.1×10^{15}	0.6

using Al as an oxygen getter appeared to show the largest activation ratio, they also show the lowest device performance, indicating that the way in which the activation ratio is determined needs greater scrutiny. Moreover, increasing activation ratios did not always translate to an increase in device efficiency. This may be due to formation of additional defects such as non-radiative trap states, which offset the benefits of increased dopant activation. Additional questions remain with regard to implanted oxygen getters' role in hindering the diffusion of group-V dopants into the absorber bulk, which may have contributed to the calculation of an increased activation ratio.

Future work in this area should focus on the spatial distribution of the implanted oxygen getters and the group-V dopants in conjunction with oxygen to determine the probability of interacting with dopants. However, this type of analysis will require high sensitivity ToF-SIMS or the use of atom probe tomography to determine the spatial concentration of impurities within the bulk. XANES (x-ray absorption near edge structure) and EXAFS (extended x-ray absorption fine structure) can be used to determine the chemical state of the implanted oxygen getters and the group-V dopants, which may provide insights into the formation of defect complexes. Additionally, advanced characterization techniques, such as positron annihilation spectroscopy (PAS) and electron paramagnetic resonance (EPR), can be used to identify and quantify the presence of specific defects and defect complexes in the absorber.

Theoretical modeling of the interactions between oxygen and dopants in different proportions and at different locations within the absorber may also provide valuable insights into the factors

that limit group-V activation. This information can then be used to guide the optimization of the doping process and improve the overall performance of p-type devices.

Chapter 3

Intrinsic CdSeTe devices and their properties

This chapter will begin by providing context and motivation behind n-type doping of CdTe and CdSeTe, including a brief review of extrinsically n-type CdTe (mainly single crystal work) where high V_{OC} greater than 1 V has been demonstrated with indium (In) doped single crystal CdTe grown through molecular beam epitaxy [30] and recent observations on intrinsic n-type conductivity in polycrystalline CdSeTe absorbers [31]. Motivation is established by the observation that $CdCl_2$ processing conditions have a significant impact on group-V dopant activation and that the distribution of Se throughout the bulk of CdSeTe can have a large influence on the optoelectronic properties of absorbers and the resulting devices [32–34]. Understanding the interactions between dopants and intrinsic defects in CdSeTe can provide a framework for optimizing group-V dopant activation by tailoring the absorber to reduce compensating donor defect formation.

The core of this chapter will review processing variations used to determine significant factors impacting donor defect formation. This section will be broken into two parts: 1) use of extrinsic n-type dopants and 2) significant processing conditions impacting donor defect formation. This section will start by establishing the intrinsic n-type nature of CST absorbers through comparison with extrinsic n- and p-type doped CST films. The second part of this section will focus on the impact of ubiquitous processing steps in high efficiency CST absorbers (namely the Se alloying and $CdCl_2$ annealing steps) in the formation of donor defects. The impact of having a graded Se composition (from bilayer CdSe/CdTe films) vs a uniform ternary composition (uniterns) is also examined. The core result established is that Se, or the lack thereof, is the most significant factor in donor defect formation.

3.1 Intrinsic Defects in CST

$CdSe_XTe_{(1-X)}$ (CST) is a ternary compound semiconductor formed through alloying CdTe with Se. This results in an absorber whose bandgap can be tailored through the stoichiometry of

Se within the bulk. While this has led to increases in the short circuit current (J_{SC}) and fill factor (FF) while retaining similar voltage, continued improvements in the open circuit voltage (V_{OC}) have been slow.

Successful activation of a group-V dopant is predicated on its substitution for a group-VI site within CST, creating an acceptor defect which decreases the net concentration of free electrons within the unit lattice. However, if the group-V atom is not incorporated into the proper lattice site, instead sitting on an interstitial or anti-site, it may act as a donor defect, increasing net electron density and thereby compensating any acceptor defects formed from the group-V dopant. These types of lattice defects are represented in Figure 3.1.

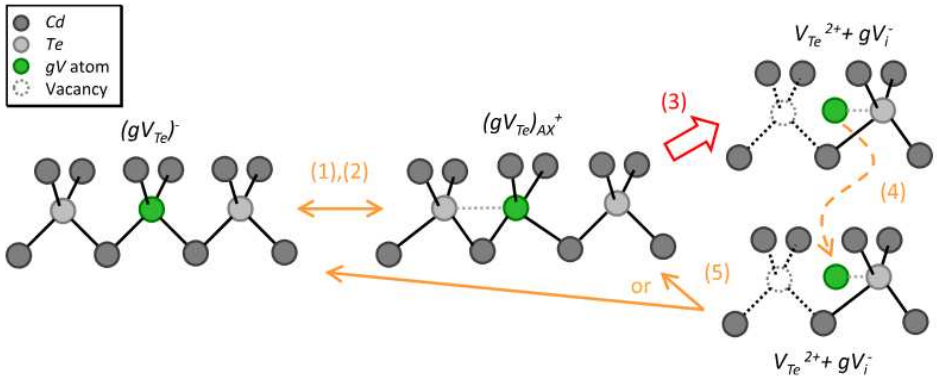

Figure 3.1: Diagram showing proper group-V substitution and the formation of compensating defects through dopant migration [16].

While much effort has been paid to engineering dopant incorporation within CdTe and CST, less effort has been put into understanding intrinsic defects which may exist in CST, how they may interact with dopant related defects, and how this may ultimately impact device performance.

The formation of defects in polycrystalline CST absorbers may occur during various steps in the absorber and device fabrication process. The use of $CdCl_2$ heat treatments (CHT), Se alloying, and group-V doping is ubiquitous in state-of-the-art CdTe devices. However, the roles that Se and Cl play in conjunction with group-V doping (N, As, P, & Sb) for p-type conversion are not well understood. Record level CdTe devices are primarily limited by a voltage deficit of roughly

200 mV (ΔV_{OC} = V_{OC}^{RAD} - $V_{OC}^{measured}$ $\approx$ 1100 – 900 = 200 mV) which typically is attributed to a combination of radiative and nonradiative recombination. These recombination processes are in part due to the low activation of group-V dopants, bandgap tailing, and potential fluctuations induced by group-V doping and/or Se alloying [35, 36].

Meanwhile, single crystal CdTe devices–without the use of Se alloying or need for a $CdCl_2$ anneal–have shown high activation ratios and demonstrated large V_{OC} greater than one volt through n-type doping with the group-III donor indium (In) [30]. This indicates that the low dopant activations and large voltage deficits seen in polycrystalline CdTe based devices are not intrinsic to CdTe material itself, but rather a consequence of the group-V doping and Se alloying processes.

This following section seeks to understand the intrinsic defect nature of $CdSe_XTe_{(1-X)}$ (CST) absorbers by decoupling the impact of group-V dopant activation in CST absorbers. Devices with p-type group-V doping (As or P) or n-type group-III doping (Al) are compared against intrinsic CST devices to gain insight into the intrinsic behavior of CST absorbers and how it may impact devices.

3.2 Determining Impact of Intrinsic Defects in CST Devices

To understand the impact that intrinsic defects in CST absorbers have on device performance, CST absorbers without any doping are compared to identical absorbers that are extrinsically doped. CST absorbers used in this study, provided by First Solar, are composed of a graded Se stoichiometry which is formed by the standard two-step process: first, a thin CdSe (0.3 μm) layer is deposited followed by a thicker CdTe (3.0 μm) layer. This bilayer structure is then annealed in a chlorine environment, known as a chlorine heat treatment (CHT), to form the polycrystalline CST absorber with a graded Se stoichiometry and thus bandgap.

Extrinsic dopants are introduced to absorbers ex-situ, prior to the CHT step. The p-type acceptors (As or P) are incorporated in a similar method to what has been published previously [22] through introduction to the CdTe surface and diffused into the bulk during a post-deposition anneal. The n-type donor (Al) however, is implanted into the exposed surface of the CdTe layer prior

to CHT. Provided the simple purpose of forming an extrinsic n-type CST absorber is to compare it to intrinsic CST, the method of ion implantation was selected to ensure incorporation of Al into the absorber without concern for potential damage induced through ion bombardment. Al implantation was performed commercially by Coherent Corporation with an implant dose of $\approx$ 2x10^{15} cm^{-2} at an energy of 200 keV. This results in a projected range of 0.3 μm, with a straggle of 0.1 μm, as calculated through the SRIM software [29]. The Al dopant is expected to act as a donor defect if incorporated into Cd substitutional sites within the CdTe lattice.

Following dopant introduction, a CHT step is performed by coating absorbers with an aqueous solution of $CdCl_2$ and annealing at 400-500°C under an inert environment. This process induces grain growth through recrystallization while providing thermal energy to promote dopant diffusion into substitutional sites, Cl diffusion along grain boundaries for passivation, and Se diffusion to form the graded Se profile. Absorbers were integrated into identical devices using a p-type zinc telluride (ZnTe) and transparent back contact (TBC) structure. Devices were measured for JV and QE performance in both superstrate (glass-side (GS) excitation) and substrate (film-side (FS) excitation) configurations using standard instrumentation under 1 sun illumination with a standard AM1.5G spectrum. This structure and the measurements configurations are shown schematically in Figure 3.2.

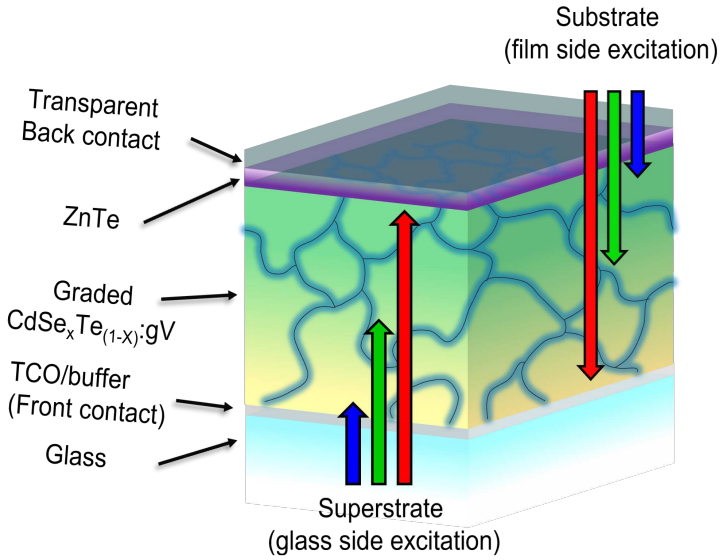

Figure 3.2: Illustration of device architecture and measurement configurations. Devices in this study are composed of a CST absorbers, deposited onto TCO coated glass, completed by deposition of a p-type ZnTe and transparent back contact. The device is measured in both superstrate (glass side) and substrate (film side) configurations.

3.2.1 Results of CST Devices with Various Dopants

These devices were analyzed with current-voltage (JV), quantum efficiency (QE), capacitance-voltage (CV), and steady state / time-resolved photoluminescence (PL/TRPL). JV results are shown for an example cell from each doping type in figure Figure 3.3. The intrinsic CST device (black curve) has behavior similar to the Al-doped device (red curve),with low currents when measured using standard glass-side illumination and a large increase in J_{SC} when illuminated from the film-side. Box plots of the main parameters for N=48 solar cells per doping type–shown below each example JV curve–demonstrate the trend in behavior between undoped and Al doped devices, which is contrasted by the p-type As- or P-doped devices. This provides a clear indication that the undoped CST devices exhibit n-type conductivity.

However, it is also clear that the undoped devices are outperforming the devices which are extrinsically n-type doped with Al, particularly in terms of J_{SC}. This is primarily due to the Al-doped devices having an overall lower external quantum efficiency (QE), as shown in Figure 3.4, in addition to having a negative QE gradient as photon energies decrease, indicating lower diffusion

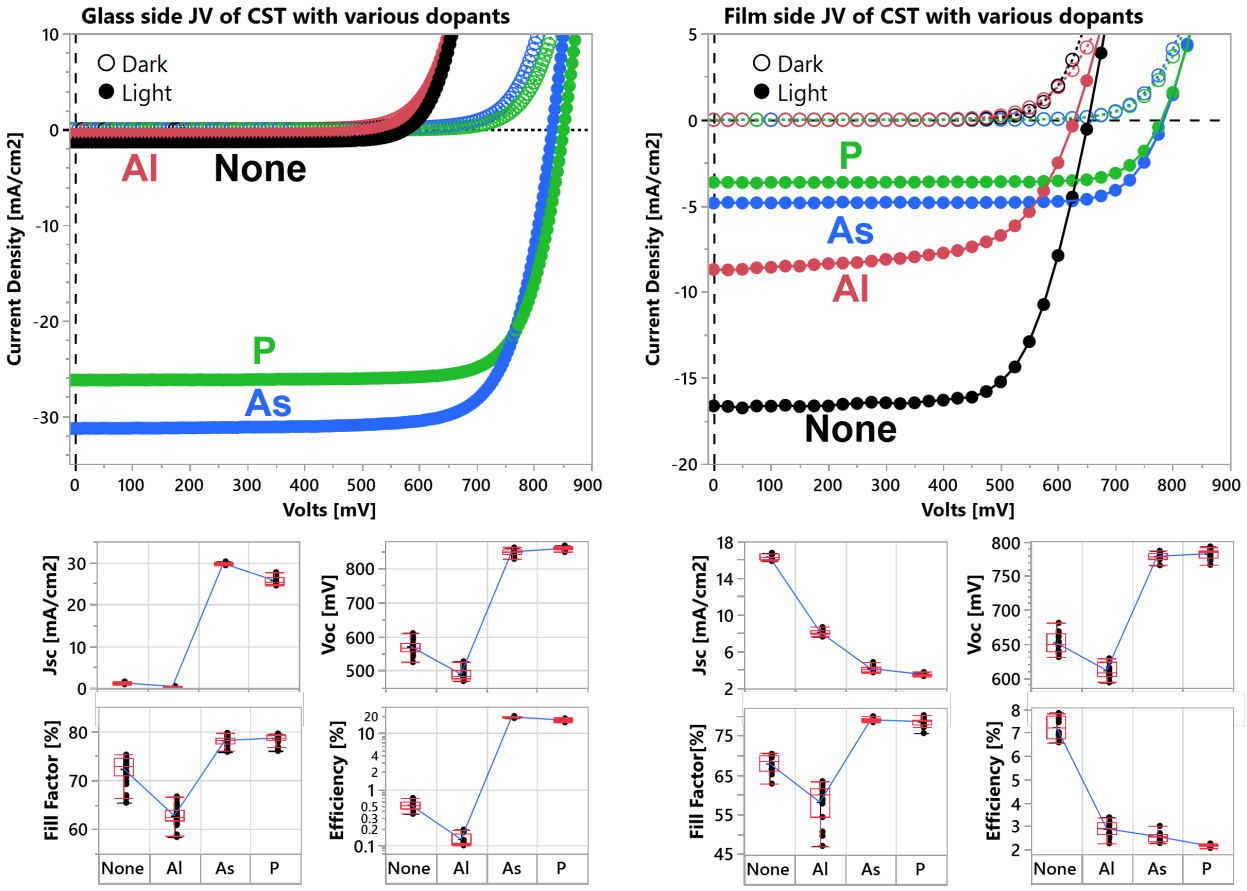

Figure 3.3: JV response of CST devices with different dopants. Glass side excitation is shown on left and film side excitation on right.

lengths for the extrinsic n-type device compared to the intrinsic n-type device. The V_{OC} and FF losses may also be attributed to this, as the dark saturation current in Al-doped devices is much larger than that of the undoped devices.

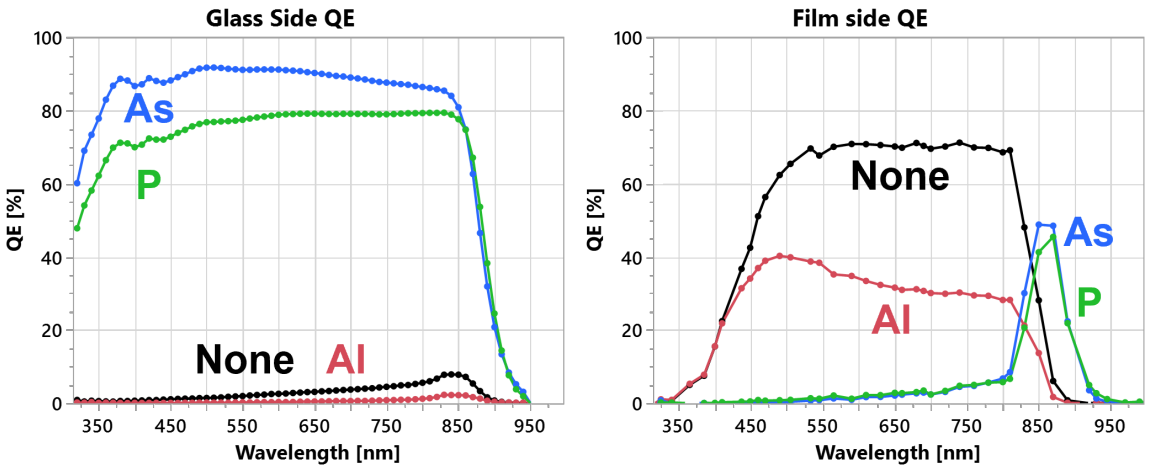

Figure 3.4: External quantum efficiency of devices with illumination from glass side on the left and film side on the right.

Devices with typical p-type doping (As in blue and P in green) show the expected behavior of >75% QE for photons with energy above the bandgap when excited from the glass side. This is opposed to the extrinsically n-type (Al in red) and the intrinsic control (black) which have better collection probability when excited from the film side. The small rise in EQE near the bandgap, seen for undoped or Al devices from glass-side and As or P devices from film-side, is associated with the "buried junction" effect, indicating the formation of a np-junction at the back of Al-doped or intrinsic devices, a result of the p-type ZnTe deposited onto n-type CST. The reduction in QE for Al-doped devices in comparison to undoped devices is likely due to diffusion limited recombination, indicated by the negative slope of EQE from high to low energy. Charges generated farther from the interface have a lower collection probability in Al-doped than in intrinsic devices which results in the reduction of J_{SC} and the increase in dark current observed through JV.

All devices, including the undoped absorbers, demonstrate carrier concentrations (CC) $\approx$ 1x10^{16} cm^{-3} with the Al and intrinsic devices exhibiting similar behavior, as shown by the CV plots in

Figure 3.5. This indicates that the Al dopant is not significantly increasing the carrier concentration and that the majority of donors formed in both the Al and undoped devices may simply be due to intrinsic defects within the CST lattice.

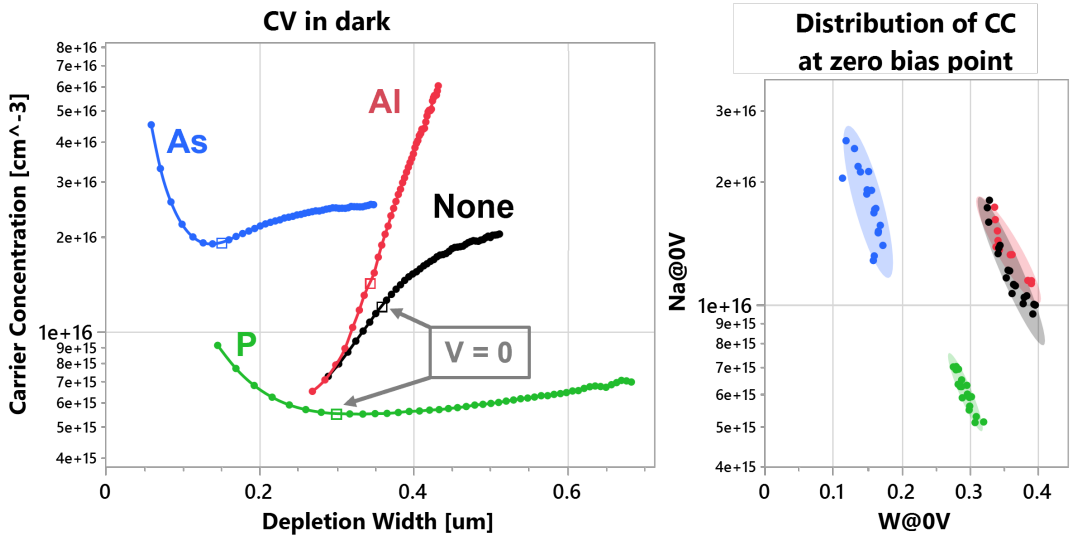

Figure 3.5: Calculated carrier concentration (CC) as a function of depletion width (W) determined from capacitance-voltage measurements for each doping type. A chart of the CC vs W at zero bias for 24 solar cells per doping type is shown to the right.

This analysis helps to understand the QE and J_{SC} relationships between the various dopants. Considering the large absorption coefficient of CST (α (E > E_g) >10^4 cm^{-1}) we expect a large majority of incident photons to be absorbed and generate charge pairs within the first half micron of the absorber. CV analysis of the Al doped and undoped devices implies the existence of a field over about 400 nm for the CST/ZnTe interface. As such, these devices, which have a field within this range, can rely on drift currents to collect a majority of charges under film side illumination.

Conversely, p-type absorbers should have field generation near the np-junction of the TCO/CST interface, which is buried at a depth of the measured depletion width (W) subtracted from the absorber thickness (d). Given that W is at most 600 nm from the junction, the minimum generation depth for drift current separation is defined as $G_{min}(J_{drift})$ = d - W $\approx$ 3.5 μm – 0.6 μm = 2.9 μm. Considering that the generation depth can be taken as the inverse of absorption coefficient, which is 1 μm for α = 10^4 cm^{-1}, only a small fraction of photons close to the band gap will generate

charges within the buried junction. This is exemplified by the spike in QE near the bandgap for p-type devices with film-side excitation, and similarly for n-type devices with glass-side excitation.

The photoluminescence (PL) for each device is measured with film-side or glass-side injection using a 645 nm laser. The PL spectra for each device is shown in Figure 3.6. The reduction in bandgap energy (E_g) from film-side to glass-side injection is expected due to the graded Se profile, where the most Se resides near the glass side and E_g is expected to be near 1.4 eV. The reduction in E_g seen for As- or P-doped devices relative to the Al-doped or intrinsic devices is likely due to the formation of donor-acceptor pairs (DAP) or bandgap tailing in these p-type devices, both of which would produce sub-bandgap states and result in a lower effective bandgap. Additionally, the intensity of the P- or As-doped devices are roughly the same for all cells, but P-doped devices have a reduced full width at half maximum (FWHM) compared to As-doped devices as a result of a sharper low energy side decay, indicative of reduced radiative recombination and a reason why P-doped devices have been able to achieve V_{OC} greater than 900 mV, historically in single crystal samples [37] some of which have even broken the 1 V barrier [38] and even more recently in record level polycrystalline samples [4], which As-doped samples have struggled to achieve even in single crystal samples [39].

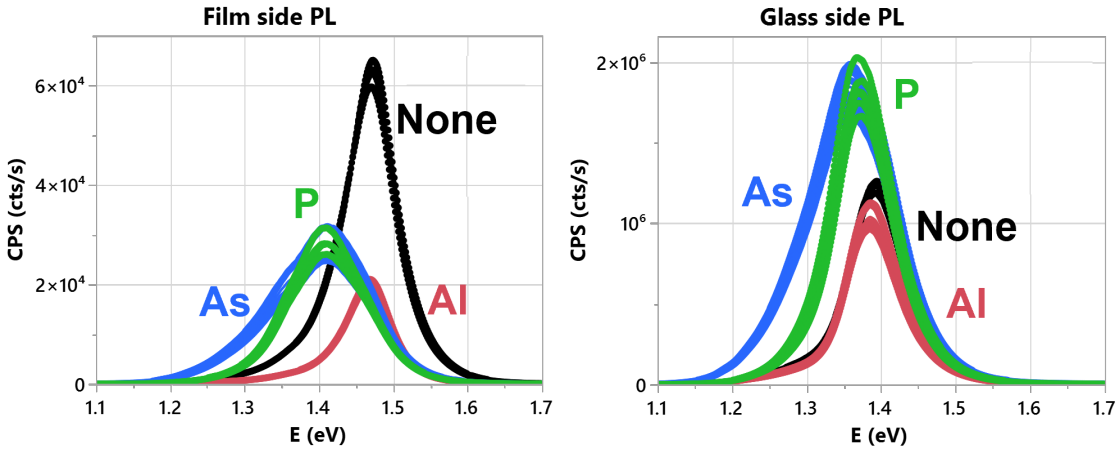

Figure 3.6: Steady state and of CST devices with various dopants with film-side or glass-side excitation.

The lifetime of charges in these devices is measured through time-resolved photoluminescence (TRPL) and is shown in Figure 3.7. The lifetime of the undoped devices is similar to that of Al-doped devices, indicating that the recombination mechanisms are similar. The difference between lifetime from the glass-side and film-side for the As- and P-doped devices is understood to be due to the difference between Se composition on each side. The film side of the device is expected to be dominated by CdTe, rather than by CdSeTe on the glass side, and it is appreciated that CdTe tends to have a lower lifetime than CdSeTe in general [40].

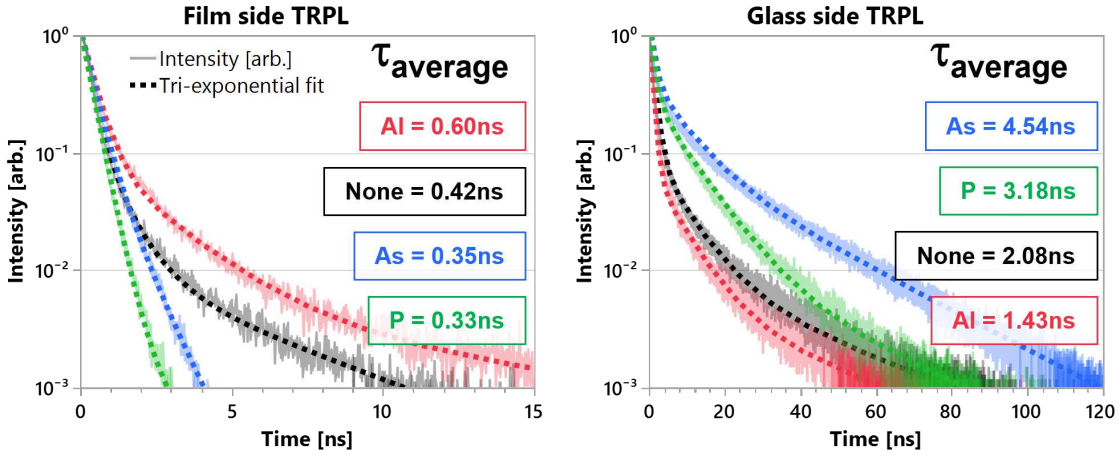

Figure 3.7: Time-resolved photoluminescence of CST devices with various dopants with film-side or glass-side excitation.

3.2.2 Spatial Distribution of Elements and Electric Fields in CST

To gain further insight into the results of JV and QE measurements, the spatial distribution and concentration of elements is measured with dynamic secondary ion mass spectroscopy (dSIMS) and the distribution of electric fields is examined through Kelvin probe force microscopy (KPFM).

Undoped and Al-doped samples show field generation near the back contact interface, while As- or P-doped samples have field generation near the front TCO interface. Thus, KPFM measurements of each film confirm the n-type nature of CST films when doped with Al or when intrinsic. These samples show that the diode field is nearly exclusively at the back of the device stack near the CST/ZnTe interface as indicated by the dashed red line. This is opposed to the p-type As- or

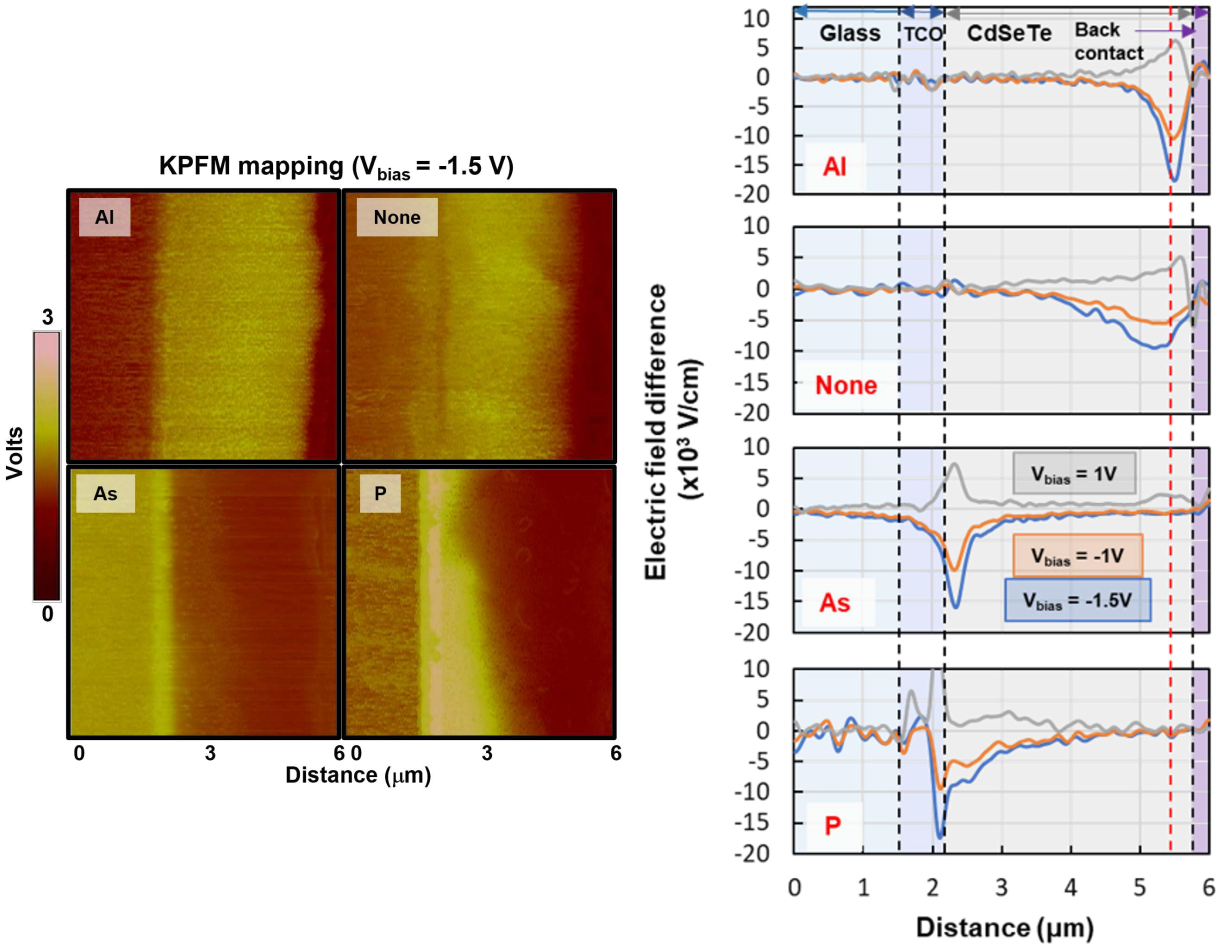

Figure 3.8: Kelvin probe force microscopy scans for each doping type. Confirms np-junction location and doping type.

P-doped devices which demonstrate a field generated near the TCO/CST interface. The intrinsic sample exhibits a weaker and smeared out field, possibly due to the donor defect nature of Se vacancies which may cause bandgap fluctuations with Se grading.

While both the Al-doped and intrinsic devices demonstrate n-type behavior, the Al-doped device has reduced performance primarily due to a drop in J_{SC}. This reduction in current may be due to diffusion limited recombination as characterized by the loss in QE at larger wavelengths, i.e. for photons which are absorbed and generate charge pairs deeper and thus farther from the junction field. Additionally, extrinsic doping has relatively little impact on the carrier concentration measured in CV (both Al-doped and intrinsic samples have $N_d \approx 1\text{x}10^{16}$ cm^{-3}), bringing to question the role which extrinsic donors play in this n-type behavior. It is also noted that these absorbers were annealed in a chamber previously used for group-V doping work, indicating that intrinsic samples may have some background As and P concentrations.

To evaluate this, SIMS data shown in Figure 3.9, demonstrates that the intrinsic device had minimal background levels of p-type dopants. Se and Cl profiles for all samples are essentially the same. The Al-implanted sample shows similarly low background As and P levels but is not shown as it was measured at a separate time.

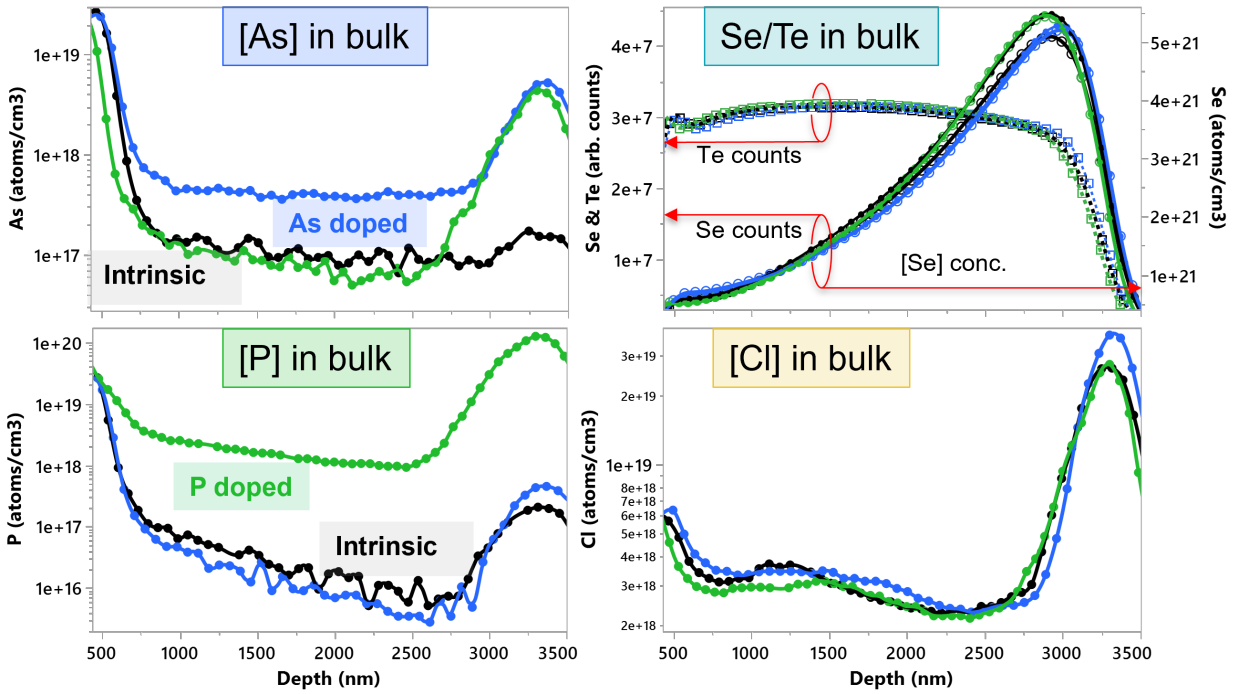

Figure 3.9: SIMS data for As, P, Cl, and Se concentrations in CST absorbers with various extrinsic dopants compared to intrinsic (none in black).

The Se profiles shown above are correlated to a bandgap gradient seen through cathodoluminescence imaging of sample cross-sections in Figure 3.10. The absorber bandgap decreases from roughly 1.5 to 1.4 eV from the back to front interfaces. The hyperspectral CL image contains the emission spectrum for each pixel, which is shown for values of x=100 and a sample of y-values along the cross-section, shown in Figure 3.11. Subgap emission, roughly 150±50 meV from the primary peak, is seen for the intrinsic, Al-doped, and As-doped devices and appears to grow more pronounced as the Se content within the graded absorbers increases.

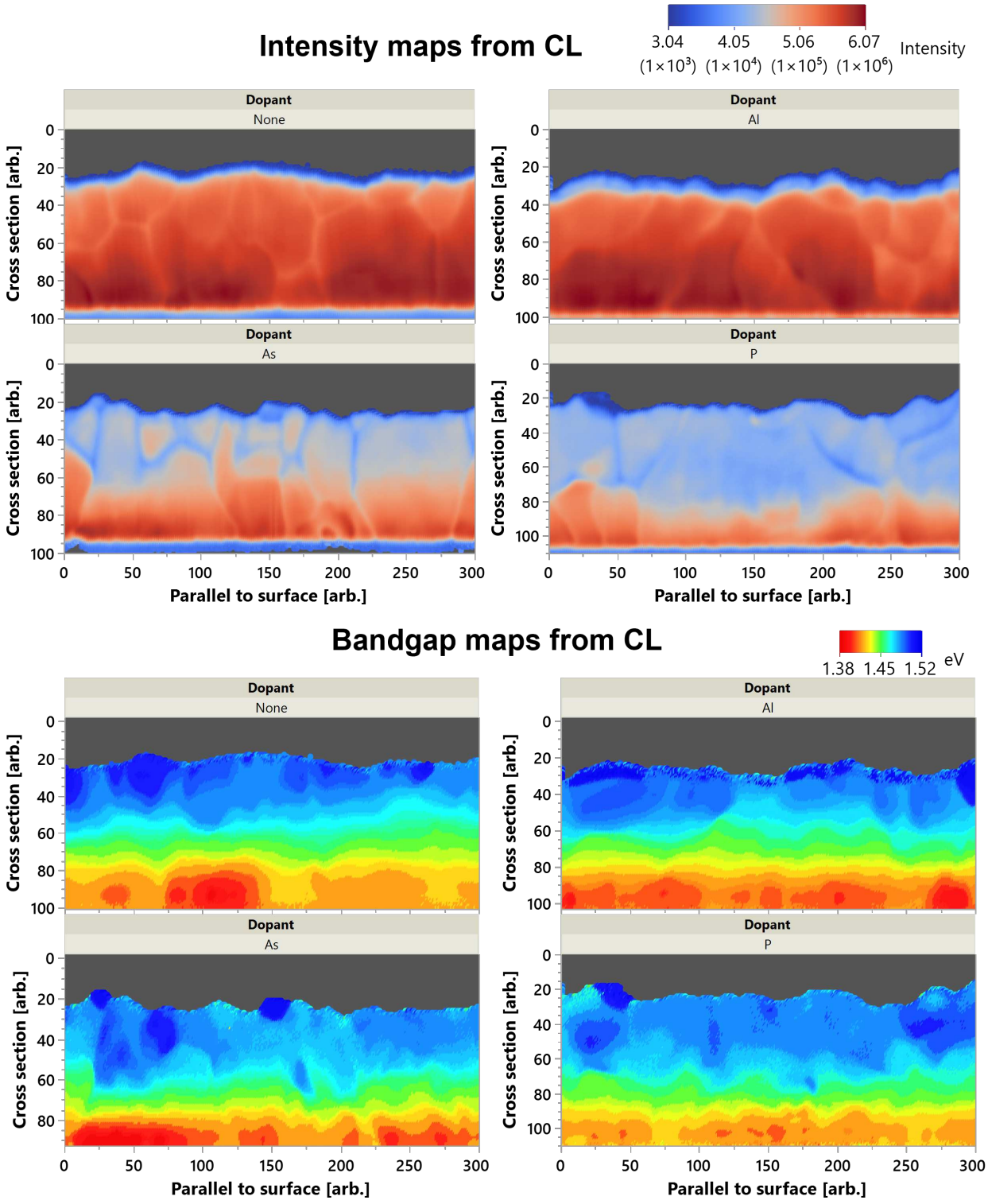

Figure 3.10: Cross-sectional SEM images colored by peak intensity or bandgap. Intensity of n-type absorbers (intrinsic or Al-doped) is uniformly high through the cross-section while p-type absorbers (As- or P-doped) show an increasing peak intensity from back (CdTe dominated) to front (CdSeTe dominated). Lighter colors at grains indicates reduced recombination from Cl passivation. Bandgap gradient seen is consistent with the Se profile from SIMS, decreasing from the 1.5 eV at the back to 1.4 eV at the front.

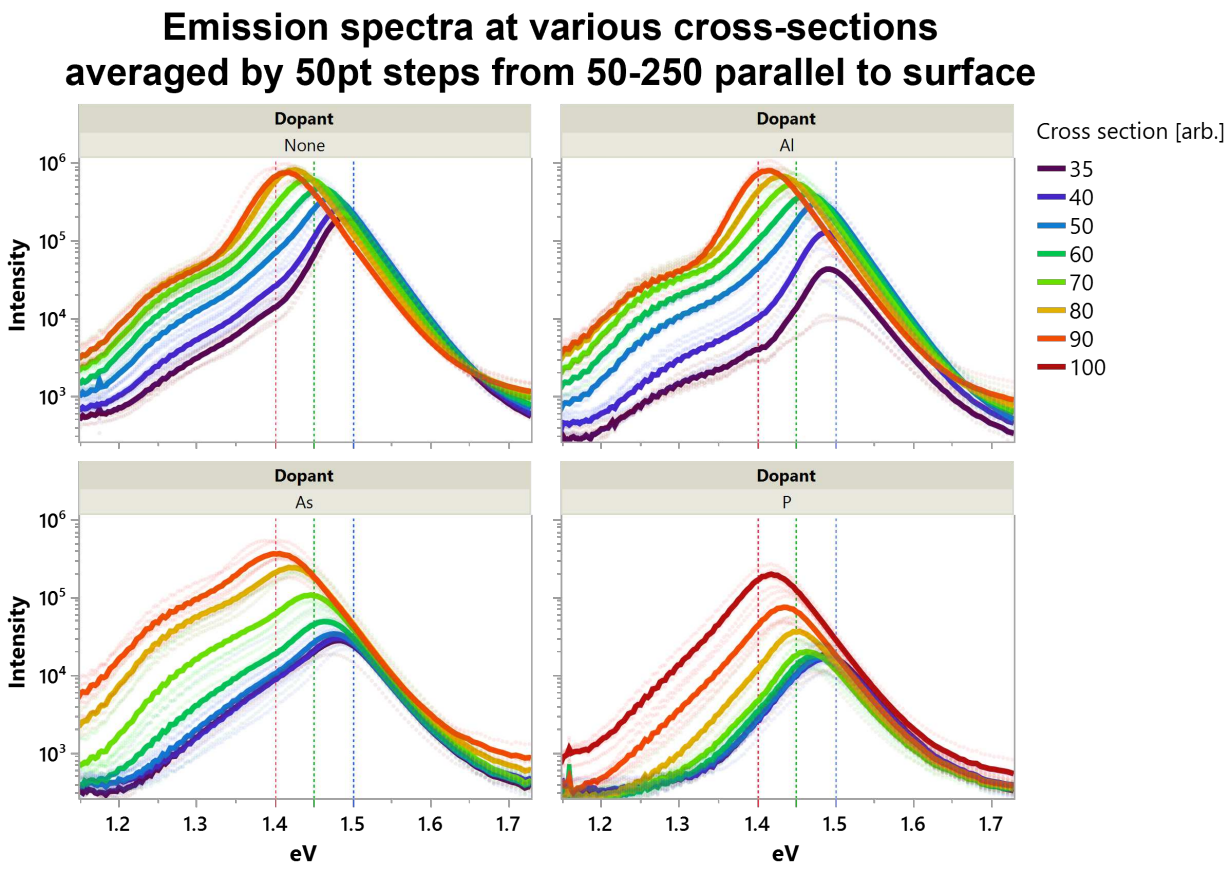

Figure 3.11: PL spectrum over the depth of the each device from the hyperspectral CL image. The PL peak energy is shown to shift with the calculated Se composition as expected from the bandgap bowing curve for CST. P-doped devices show much less subgap emission than As-doped devices, indicating that the P-doped devices have reduced band tailing.

3.3 Significant Defects Impacting Type Conversion in CST

Undoped CST absorbers with a graded stoichiometry of Se were shown to exhibit intrinsic n-type characteristics with behavior similar to absorbers extrinsically doped to form donor with aluminum (Al). However, the Al-doped devices had a lower J_{SC} and EQE than the intrinsic devices despite having roughly the same carrier concentrations. This leads to the question of what factors are most significant to the formation of donor defects in CST absorbers?

This section will evaluate the significant factors impacting donor defect formation in CST by examining $CdSe_XTe_{(1-X)}$ absorbers with a uniform concentration of Se (X(depth) = constant)

compared to an absorber with the typical graded Se stoichiometry (X(depth) = variable) as discussed in the previous section. The primary difference between the absorbers presented in this section is therefore the Se profile as a function of the absorber depth (X(depth)). Devices with a constant Se concentration throughout the CST bulk are considered to have a "uniform ternary" stoichiometry and are referred to as "uniterns" – a portmanteau of **uni**form **tern**ary.

These absorbers were grown at First Solar's California Technical Center using close space sublimation (CSS) to a target thickness of 3μm. In this study, CST absorbers were left undoped (intrinsic) or extrinsically doped with indium (In) in attempt to replicate high V_{OC} demonstrated for In doped sx-CdTe [30]. Ex-situ doping with indium was performed in the same manner as Al above, that is through post-deposition ion implantation. Following dopant introduction, all absorbers were given the same CHT and then integrated into devices identical to those described above.

Following CHT and prior to device integration, the Se composition and thickness of absorbers is evaluated with x-ray fluorescence (XRF) from the film side of absorbers, as shown in Figure 3.12. This confirms that Se composition of uniterns is as expected and the thickness of each absorber is within 10% of the target thickness. The reported composition of the graded Se absorber is also consistent with expected Se profiles where a majority of Se will reside near the glass side and only a small fraction diffuses to the film side, such as is seen from the CL scans in Figure 3.10.

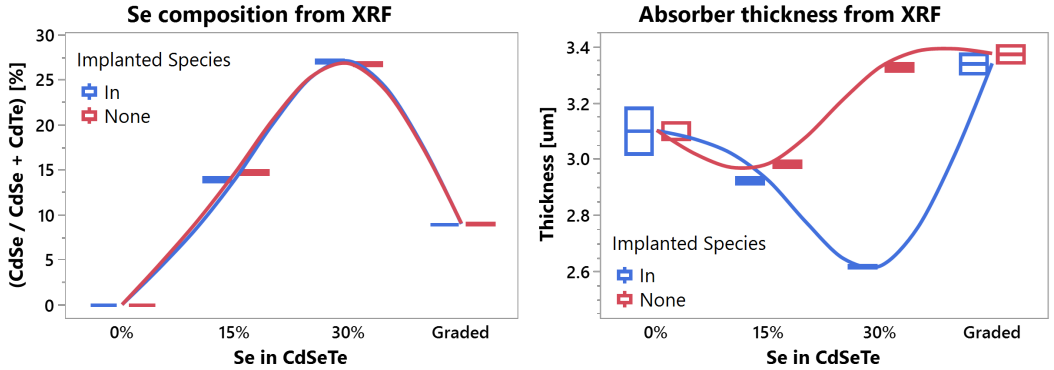

Figure 3.12: X-ray fluorescence (XRF) measurements of Se composition and thickness of CST absorbers. Unitern absorbers show slightly less Se than expected, indicating some loss of Se during growth. Extrinsic In doping appears to have minimal impact to Se content.

Steady-state and time-resolved photoluminescence are used to determine the bandgap of each absorber and potential impacts of changing Se compositions, as shown in Figure 3.13 and Figure 3.14. The PL peak energy when excited from the film-side is shown to shift with the calculated Se composition as expected from the bandgap bowing curve for CST. The PL peak height is also shown to increase with Se composition, which may be an indication of increased radiative recombination. TRPL of absorbers, measured with excitation from the film-side, demonstrates a similar correlation in lifetime to Se composition as was seen in the PL intensity. That is, as the concentration of Se increases, so does the lifetime of the charge carriers. The similar lifetimes measured for 15% and 30% Se intrinsic devices may be due to various processing conditions. Additionally, the generally low lifetimes seen here is typical for film-side excitation in graded Se devices, where CdTe is expected to dominate on the film side. As for the unitern devices which should have a uniform concentration of Se through the device, further evaluations are needed to understand what the reasons for such low lifetimes are, but appear consistent with what has been reported for intrinsic uniterns in the past [41].

All absorbers were then integrated into the standard device structure and measured for JV and QE performance in substrate (film-side) configuration, as this showed the best performance for intrinsic devices previously, and CV measured in the dark. Example JV curves for each device type is shown below in Figure 3.15. The impact of changing dopant dose, for either Al or In dopant, had little significance to changing device parameters. This is also generally true for changing the concentration of $CdCl_2$ used during CHT. While In-doping afforded a greater J_{SC} than comparable Al-doped samples, it had little impact on V_{OC} or fill factor, and all significant device differences can be attributed to the changing Se composition.

The intrinsic devices show an unexpected rollover in forward bias, even for the graded Se device which was previously seen to behave well under film-side excitation. The reasons behind this are not clear, and follow-up studies of similar devices are required to rule this out as a measurement artifact. Nonetheless, a trend in decreasing V_{OC} and J_{SC} are seen to increase with Se composition, while the fill factor (FF) is seen to decrease with Se composition. This is likely due to the increased

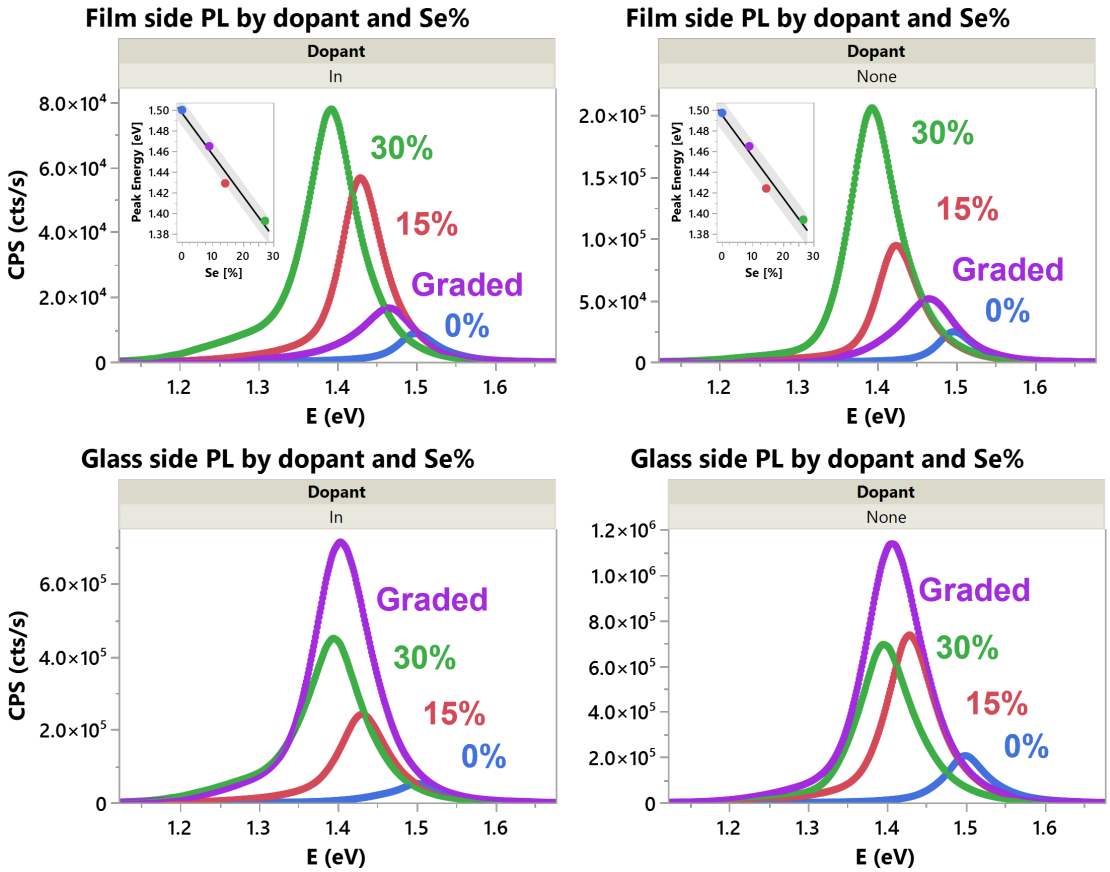

Figure 3.13: PL measured with film side or glass side excitation for CST absorbers with various Se compositions. The PL peak energy is shown to shift with the calculated Se composition as expected from the bandgap bowing curve for CST. Graded Se devices show a larger bandgap from the film side where CdTe is expected to dominate.

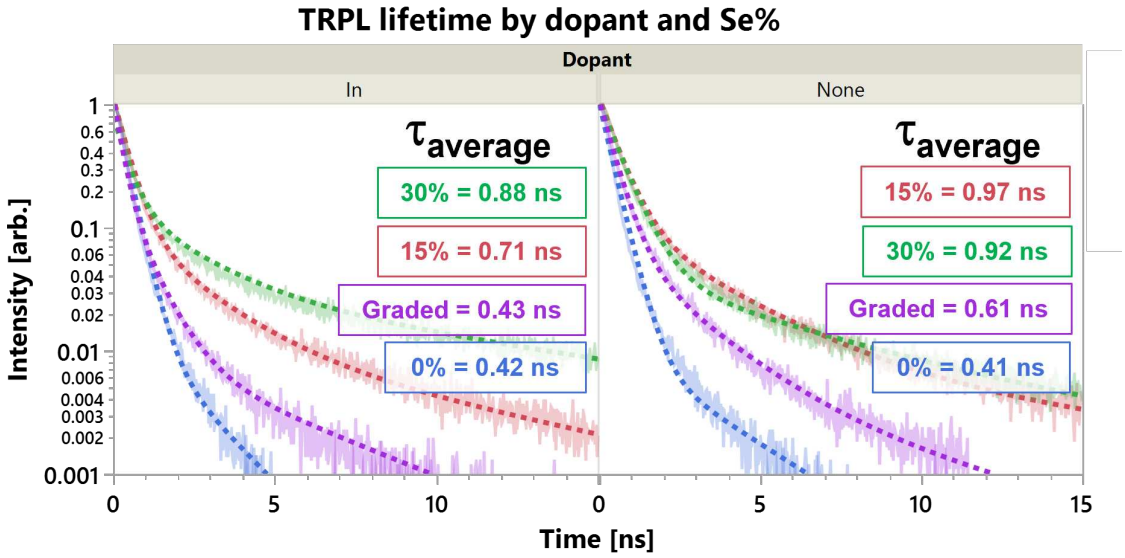

Figure 3.14: Lifetime calculated from TRPL measured with film side excitation is seen to increase with Se concentration. The inclusion of extrinsic In dopant appears to reduce the effective lifetime.

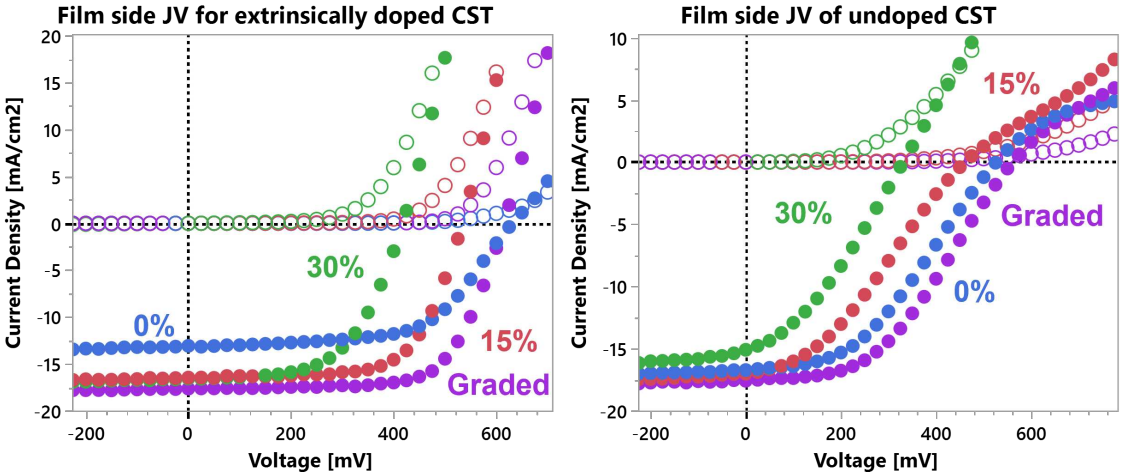

Figure 3.15: JV curves for extrinsically doped or intrinsic CST unitern devices with X = 0, 0.15, and 0.3 compared to a graded Se control device. The intrinsic devices all appear to show a rollover in forward bias, reasons for which are not clear.

bandgap of the graded Se device, which would increase V_{OC}, while the increased Se content in unitern devices would increase the density of donor defects and thus reduce FF.

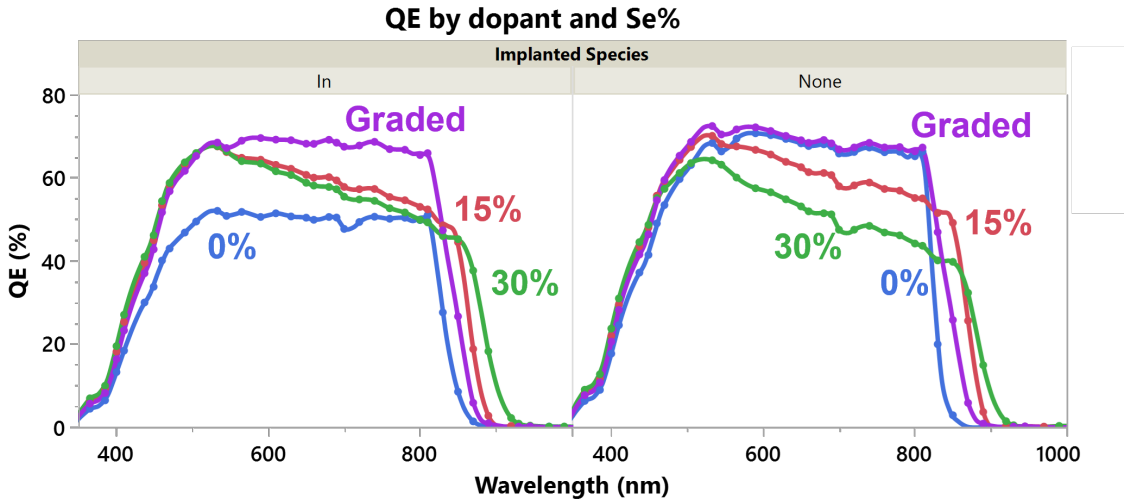

Figure 3.16: Example QE curves for extrinsically doped or intrinsic CST unitern devices compared to a graded Se control device.

Example QE curves with film-side excitation for each device is shown in Figure 3.16. Although the JV for intrinsic devices displayed problems at forward bias, the zero bias point appears well-behaved and thus the unbiased QE curves taken as representative of device behavior. The graded Se device, along with the CdTe device (X = 0) show a healthy QE curves which is flat around 70%. This is unlike the Se unitern devices (X = 0.15 and 0.3) which show a negative gradient for higher wavelengths. As this is a film-side measurements, higher wavelengths are absorbed deeper in the absorber, and thus further away from the depleted region expected to reside near the back contact in these devices. As the concentration of Se throughout the bulk of these absorbers is increased, the collection probability is reduced, which may stem from either a reduction in diffusion length at large due to additional defects from Se, or a consequence of the reduction in depletion width with high Se concentration as seen from CV analysis shown in Figure 3.17. This reason this is not seen for the graded Se device may be due to either the graded Se profile, which allows for a more uniform field across the bulk, or the fact that its depletion width is significantly larger than that of

the unitern absorbers (or a combination of these two properties), which is also true for the pure CdTe sample.

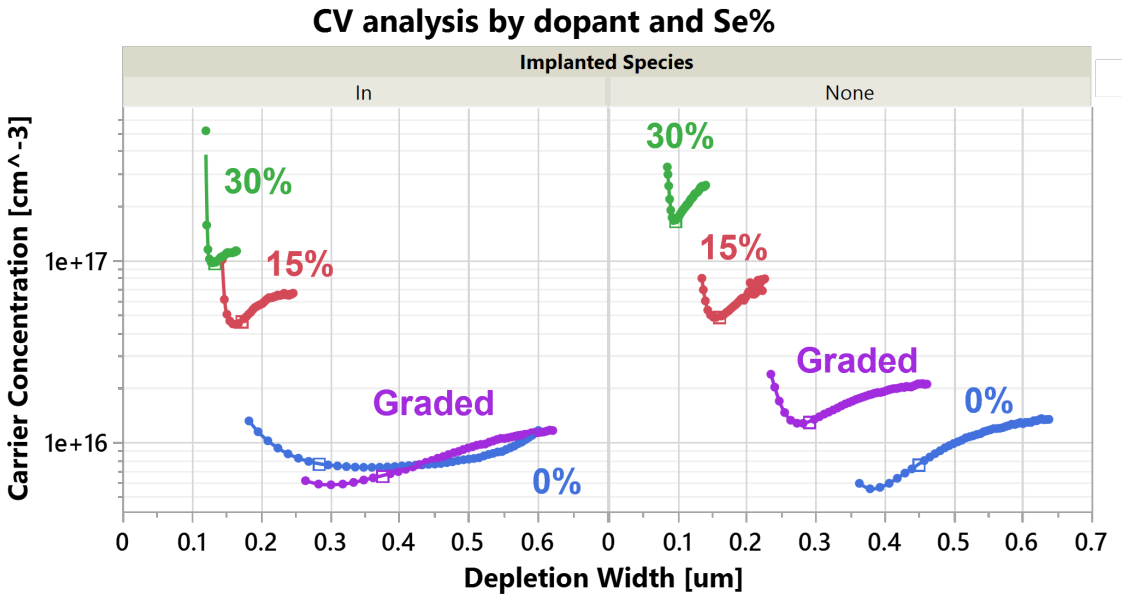

Figure 3.17: Example CV curves for extrinsically doped or intrinsic CST unitern devices compared to a graded Se control device.

CV of completed devices, shown in Figure 3.17 shows a strong correlation between the density of donor defects and the fraction of Se in the absorber, from less than 10^{15} cm^{-3} for 0% Se (CdTe) to > 10^{17} cm-3 for 30% Se for either the intrinsic CST or extrinsically doped CST devices. The fact that donor density is approximately the same for devices with similar Se content, independent of the use of an extrinsic dopant, indicates that intrinsic defects in CST are the primary source of donor defects.

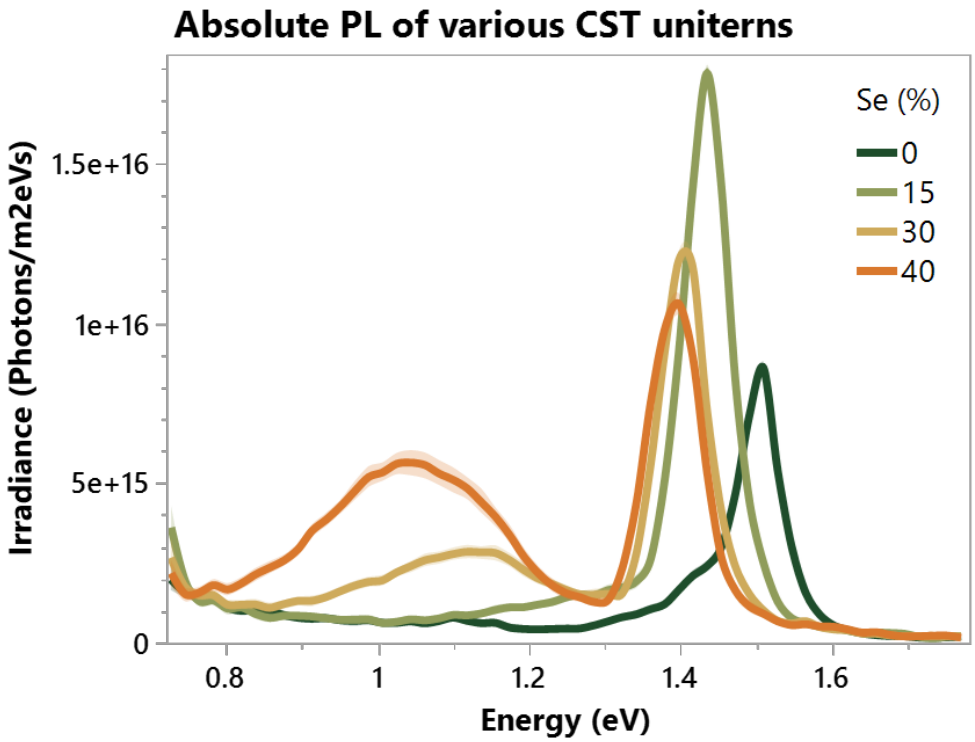

Figure 3.18: Absolute photoluminescence of unitern CST absorbers with various Se stoichiometries.

Absolute PL of devices with various Se stoichiometries is shown in Figure 3.18. The primary PL peak energy is shown to shift with the calculated Se composition as expected from the bandgap bowing curve for CST, while the intensity of the subgap peak is seen to increase with Se composition. However, the peak intensity is seen to decrease for higher Se concentrations, which is unexpected, and these absorbers were not further integrated into devices.

3.4 Conclusions

This study provides compelling evidence that CdSeTe (CST) absorbers exhibit n-type properties in the absence of intentional doping. This conclusion is supported by Kelvin probe force microscopy (KPFM) mapping, which revealed a built-in electric field peak and junction formation at the CST/ZnTe interface in CST devices without any intentional doping. This was reinforced through observations of similar junction formation in CST devices when extrinsically doped n-type with aluminum (group-III element) and contrasted by junction formation observed at the FTO/CST

interface in devices when CST was extrinsically doped p-type with arsenic or phosphorus (group-V elements). Given that the ZnTe layer is p-type doped, these results are characteristic of np-junction formation through contact with an n-type CST layer when CST is undoped or doped with some group-III element such as aluminum. These results are consistent with the hypothesis that the large vapor pressure of Se in the CdSeTe system would result in a relative abundance of Se vacancies, which themselves are intrinsic donor defects and may be further substituted by a group-III element to act as an extrinsic donor defect, both converting CST n-type.

Comparing performance between devices consisting of an undoped CST or extrinsically doped CST absorber provided insight into the consequences and potential leverages of an undoped CST platform. The device performance difference can be generally understood by considering the electric field as a function of depth across the device (E(x)) measured from KPFM compared to an expected charge generation profile (G(x)) based on the illumination direction. When these two profiles overlap, as is the case here for p-type CST devices illuminated from the glass side or n-type CST devices illuminated from the film side, the performance peaks. While this alone may be a trivial result, it highlights the problems underlying group-V dopant activation in CST. Se alloying in CdSeTe alters the defect chemistry to favor donor formation, altering the junction quality and compensating group-V doping efforts.

A key finding of this chapter was the dominant role of selenium (Se) composition and distribution in determining the donor defect density within CST. Devices with higher uniform Se concentrations—so-called *unitern* absorbers—exhibited significantly increased donor densities ($> 10^{17}$ cm^{-3} at 30% Se) compared to absorbers with a graded Se profile ($< 10^{16}$ cm^{-3}). Interestingly, while the use of group-III dopants (aluminum or indium) were intended act as extrinsic donor defects, their influence was minimal compared to the intrinsic effects induced by Se alloying. Capacitance-voltage profiles showed negligible changes in carrier concentration upon doping, with the only significant changes resulting from the change in Se profiles, further reinforcing the idea that intrinsic defect formation is the primary determinant of conductivity in CST. The charge concentration and shallowness of the depletion width (and thus strength of the electric field) in

devices is correlated to the concentration of Se in the CST absorbers. These results point toward Se-related intrinsic defects, potentially selenium vacancies (V_{Se}), as a major source of donor defects in CST films. This was further supported by the observation of an increasing sub-bandgap peak emission with increasing Se content, suggesting an increasing density of defect states.

Another critical insight from this work was the importance of Se distribution (graded vs. uniform) in mitigating donor defect impacts. Graded Se profiles, typically achieved through bilayer CdSe/CdTe deposition and post-deposition annealing, were shown to suppress donor defect formation and promote better charge collection. The graded Se profile has two native benefits vs the uniform ternary profile, especially in the context of p-type doping. The bandgap gradient creates a built-in electric field across the absorber depth to enhance charge pair separation while the reduction in Se concentration towards the back of the device promotes a more favorable defect chemistry for acceptor defect formation. While the charge collection probability was roughly uniform as a function of wavelength (and thus charge generation depth) for devices with no Se (CdTe only) or a graded Se profile, devices with a uniform Se concentration demonstrated a diffusion limited collection probability (decreasing probability with charge generation further from junction) despite having nominally longer carrier lifetimes. This indicates that the intrinsic donor defects associated with Se are prone to act as recombination centers and greatly limit the effective diffusion length of charges in CdSeTe. It is also plausible that Se alloying introduces localized potential fluctuations that limit quasi-Fermi level separation, and thus open-circuit voltage.

Future work should focus on quantifying the formation energies of Se-related point defects under varying processing conditions, modeling the impact of Se gradients on band structure and junction dynamics, and exploring passivation strategies to suppress unwanted donor defect formation while enhancing group-V dopant activation.

Chapter 4

Large Bandgap CdSe

4.1 Introduction

While photovoltaic devices based on CdTe continue to improve, single junction solar cells are approaching maximum efficiencies. Meanwhile, the demand for clean renewable energy across the globe continues to grow. One way to address this demand is through the implementation of tandem solar cells. This can allow PV modules to theoretically improve output efficiency (η) upwards of 15% (η_{Max}(Single junction) $\approx$ 32% $\rightarrow$ η_{Max}(Two junction) $\approx$ 47%) provided an ideal pairing of high and low bandgap materials.

The structure for high efficiency two-junction devices consists of a bottom-cell with $E_g \approx$ 1.1eV and peaks when paired to a top-cell of $E_g \approx$ 1.7eV. While the bottom cell may be composed of mature technologies such as silicon (Si) or copper indium gallium selenide (CIGS), there is a lack of mature PV technologies with a large bandgap.

As discussed previsouly, $CdSe_XTe_{1-X}$ has a bandgap dependent on the concentration of Se, up to pure CdSe with $E_g \approx$ 1.7eV for X = 1 (CdSe). Thin-film CdSe is routinely grown during the processes of alloying CdTe to $CdSe_XTe_{1-X}$ in modern record CdTe-based cells using methods such as close-space sublimation (CSS) or vapor transport deposition (VTD). This provides a low-cost introduction of tandem top-cells based on CdSe to industrialization without need for development of fabrication processes from the ground up. These properties make CdSe an attractive material for application in tandem PV devices, but in order to be paired with mature bottom-cell technologies it is important to first understand the limitations of single junction CdSe devices.

This chapter will review the development of CdSe absorbers into single junction devices to understand current limiting factors that can be expected to translate to tandem structures. First, the general properties of CdSe absorbers will be reviewed, establishing requirements for materials used within the device stack. Following this, the process of engineering CdSe devices will

be reviewed to determine the best-known method for making solar cells from CdSe. Finally, an evaluation of the factors limiting device performance will be undertaken, leading to a conclusion with recommendations for future work in this subject.

4.2 CdSe Absorbers

CdSe as an optoelectronic material has been researched for more than half a century, including rudimentary CdSe tandem devices [42–44]. Due in part to the emergence of CdSe as a critical layer within record $CdSe_{1-X}Te_X$ [45], interest in CdSe as a tandem candidate has grown in recent years [46–48]. In this section, the properties of CdSe absorbers grown via close space sublimation (CSS) at Colorado State University will be reviewed alongside generally relevant materials properties used to inform the engineering of devices. This will establish the properties of CdSe absorbers which are relevant to the integration of devices, and will be used to inform the discussion of device performance in Section 4.3.

4.2.1 Deposition of CdSe at Colorado State University

CdSe absorbers, deposited at CSU with close-space sublimation (CSS) using the Advanced Research Deposition System (ARDS), were grown from a single source of stoichiometric CdSe powder as the source material. The deposition conditions for CdSe thin films were determined by examining the vapor pressure curve for CdSe [49], as shown in Figure 4.1, noting that at the operating point of ≈40mTorr we require temperatures in excess of 500°C to sublime CdSe.

When CdSe is heated above a suitable vapor-pressure temperature, the source powder decomposes into gaseous cadmium and selenium, shown by the reversible reaction in Figure 4.1. In CSS, the substrate (TCO-coated glass) is held at a temperature below the vapor-pressure temperature of CdSe, which allows the sublimed vapor to recondence onto the substrate without excessive re-evaporation. In this work, the substrate temperature was held at 475°C, while the source was held at 575°C (ΔT = 100°C), schematically shown for the ARDS system in Figure 4.2.

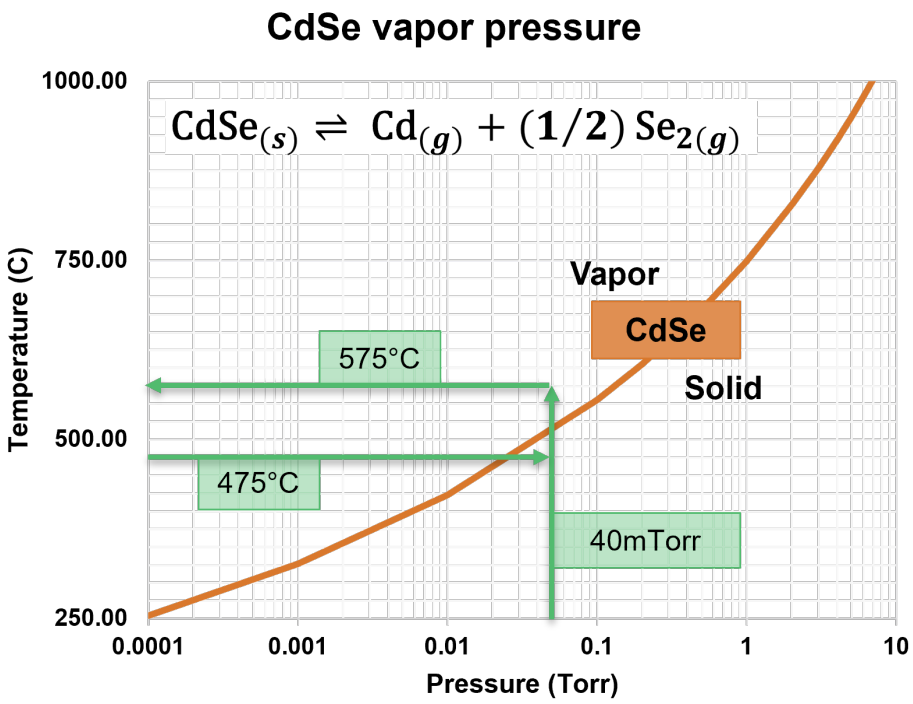

Figure 4.1: Vapor saturation pressure of CdSe as a function of temperature. The green arrows indicate the operating point of the ARDS (≈40mTorr) and the source and substrate temperatures, where the source is held at 575°C and the substrate is held at 475°C.

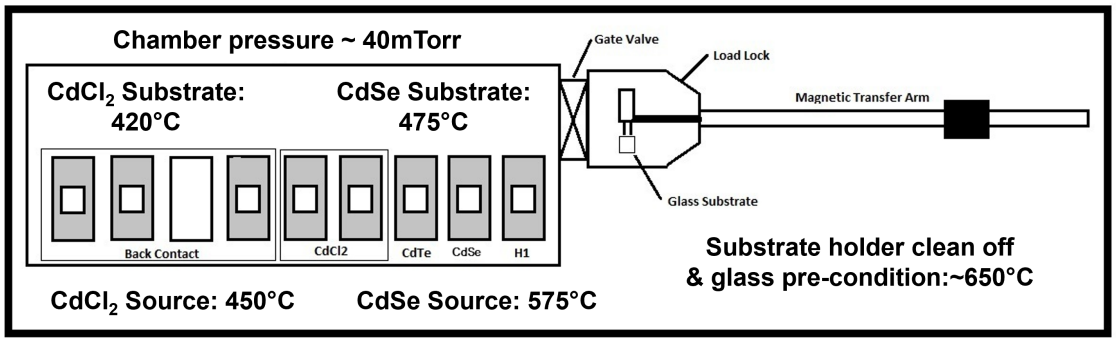

Figure 4.2: Diagram of the ARDS configuration with source and substrate temperatures for CdSe and $CdCl_2$ indicated.

The thickness and stoichiometry of as-deposited CdSe absorbers were determined by x-ray fluorescence (XRF), shown in Figure 4.3. This reveals that the deposition of CdSe is linear with time (rate ≈ 1 μm/s) and that thinner absorbers tend to have a reduced Se content. This may be a result of Se off-gassing from the substrate during cooldown, where the thicker absorber is able to retain a greater concentration of Se in bulk.

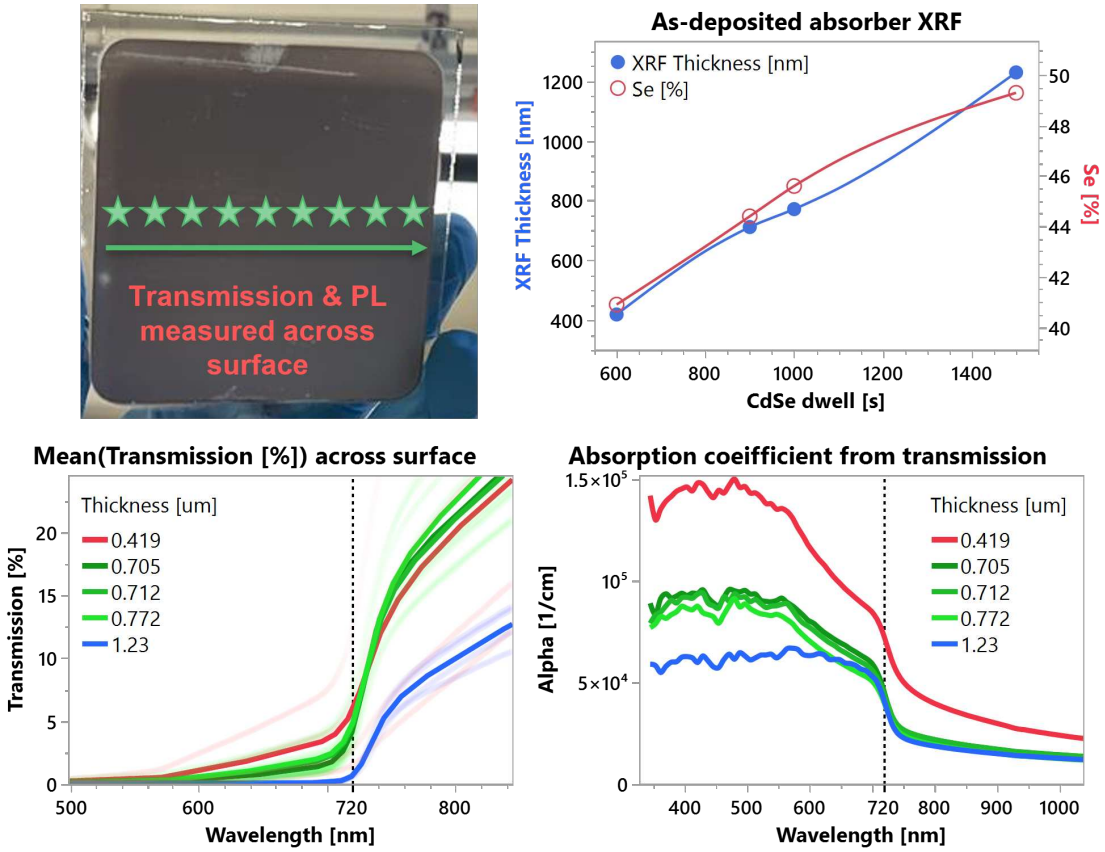

Figure 4.3: Transmission, XRF, and PL measurments were measured across the surface of CdSe absorbers as indicated in the photo of a CdSe absorber. XRF data shows a linear growth rate (1μm/s) with increased Se content for thicker absorbers. Transmission data indicates a large bandgap of 1.7eV and absorption coefficient >10^4 cm^{-1} for E>E$_g$.

The bandgap of as-deposited absorbers was determined via transmission measurements across the surface of the absorber using a UV-Vis spectrometer, also shown in Figure 4.3. This shows that the peak absorption onset for any thickness occurs near 720nm ($\approx$1.7eV), which is consistent with the expected bandgap of CdSe. The transparency of photons above the bandgap is also seen

to decrease with increasing absorber thickness. The absorption coefficient for these films was calculated from the transmission spectra, and was found to be >10^4 cm^{-1} for E > E_g, indicating that >90% of photons may be absorbed within the first micron of the absorber.

Following the initial deposition, various post-processing conditions to promote recrystallization and passivation of grain boundaries were evaluated using $CdCl_2$ heat treatment (CHT), similar to CST devices [50, 51]. First, CHT was explored using CSS in the ARDS, where $CdCl_2$ was sublimed onto the CdSe surface and allowed to diffuse into the CdSe film. This process reduces the melting point of CdSe, allowing recrystallization during the cooling period and resulting in increased grain size and PL peak emission, as shown in Figure 4.4.

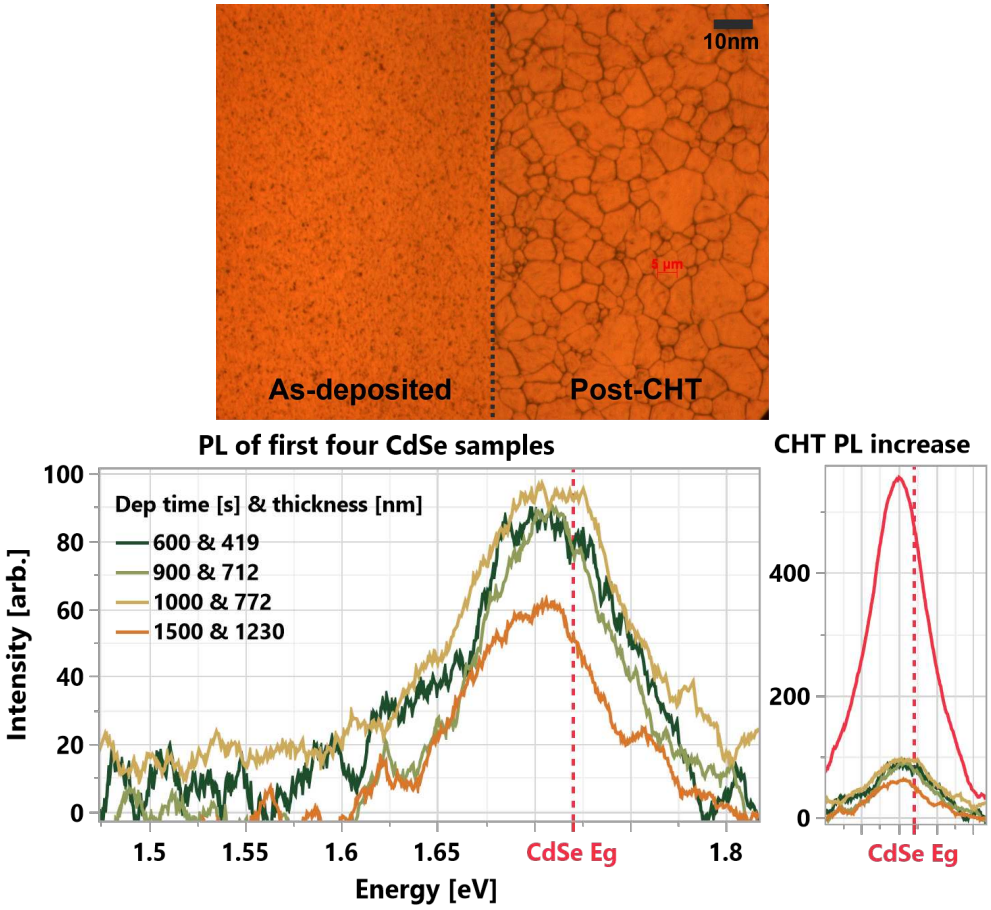

Figure 4.4: Optical microscopy of CdSe surface demonstrates the growth in grain size resulting from the CHT process. PL measurements of as-deposited absorbers demonstrates peak emission close to the expected bandgap of 1.7eV. PL emission is increased following the CHT process, as indicated by the red curve in the right-hand figure.

However, plane-view and cross-sectional SEM imaging of absorbers which received a CHT from the ARDS, shown in Figure 4.5, reveal a rough surface with voids and stacking faults which may be prone to shunting / recombination of charges. To combat this, a wet CHT process, similar to that used for CST absorbers, was explored. The same absorber was given this wet CHT, with results shown to the right in Figure 4.5. This process resulted in a smoother surface, with larger grains and no voids or stacking faults.

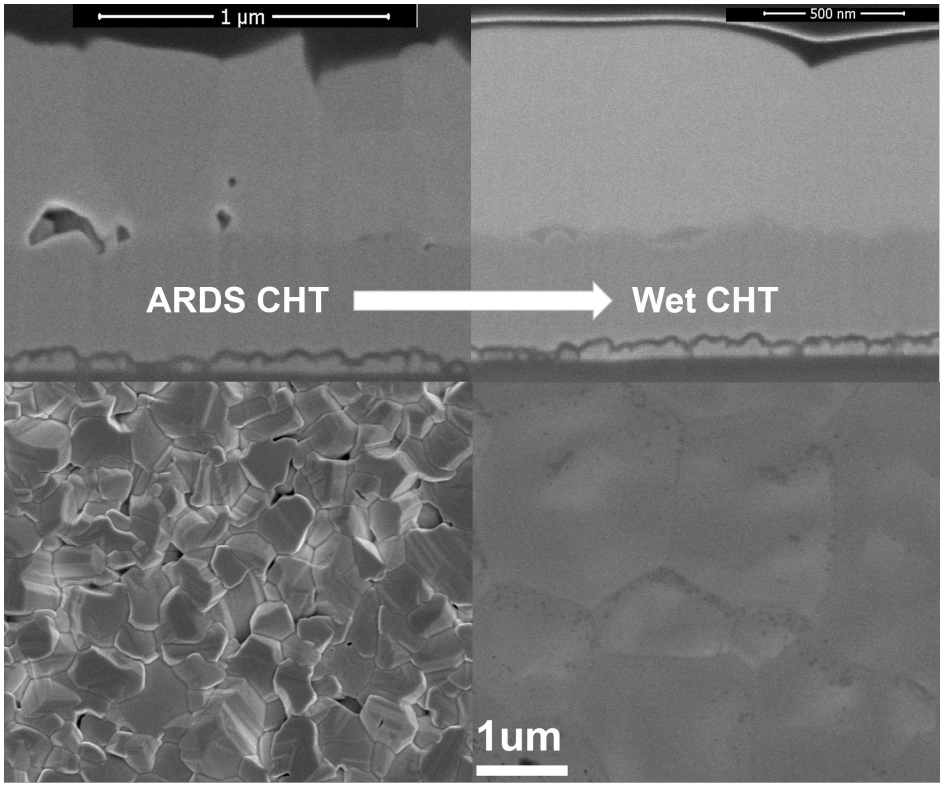

Figure 4.5: Cross-section and plane view SEM imaging of CdSe absorbers with CHT from the ARDS (left) and wet CHT (right). The ARDS CHT process results in a rough surface with voids and stacking faults, while the wet CHT process results in a smoother surface with larger grains and no voids or stacking faults.

The wet CHT process was then evaluated without any ARDS CHT processing on a number of the absorbers grown at CSU. Cross-sectional SEM of absorbers with a wet CHT step, imaged following integration into completed devices and shown in Figure 4.6, reveals that the wet CHT process alone is sufficient to grow large grains with a low density of defects. Additionally, the thickness measured from XRF in Figure 4.3 is found to be consistent with the cross-sectional

thickness given some degree of surface roughness. Devices made from CdSe absorbers with either the ARDS CHT, wet CHT, or a combination of the two processes showed that the ARDS CHT alone did indeed result in shunted devices, as indicated by the dark JV curves.

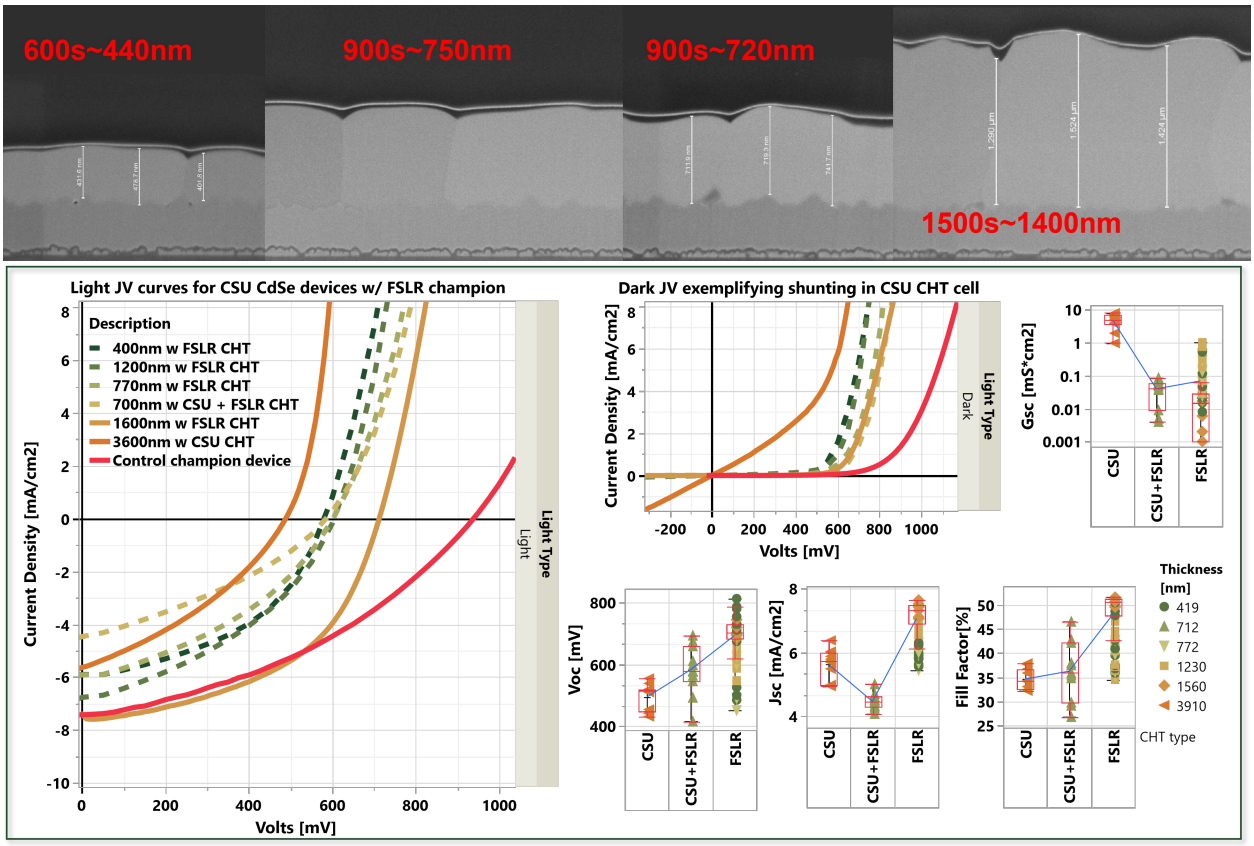

Figure 4.6: Cross-sectional SEM of CdSe absorbers with a wet CHT step. The thickness of the absorber is found to be consistent with the XRF measurements, and the surface is smooth with large grains and low density of defects. JV curves for devices with either ARDS CHT, wet CHT, or a combination of the two processes are shown below. The ARDS CHT alone (solid orange curve, refered to as CSU CHT) resulted in shunted devices, while any use of the wet CHT process resulted in devices without shunting, eximplified by the exponential difference in short-circuit conductance (G_{SC}) in the dark.

Time of flight secondary ion mass spectroscopy (ToF-SIMS) was used to map the distribution of elements (arbitrary counts) along a 20 by 20 μm square area on a representative CdSe absorber from First Solar following a wet CHT process, shown in Figure 4.7. Low background levels of sulfer and tellurium are seen (total counts three orders of magnitude less than Se) likely due to the historic use of these elements within First Solar's VTD process. Cl is seen to primarily accumulate

along grain boundaries, as expected from a chlorine passivation process, but some Cl is noted within grains and concentrated around areas where oxygen is most abundent.

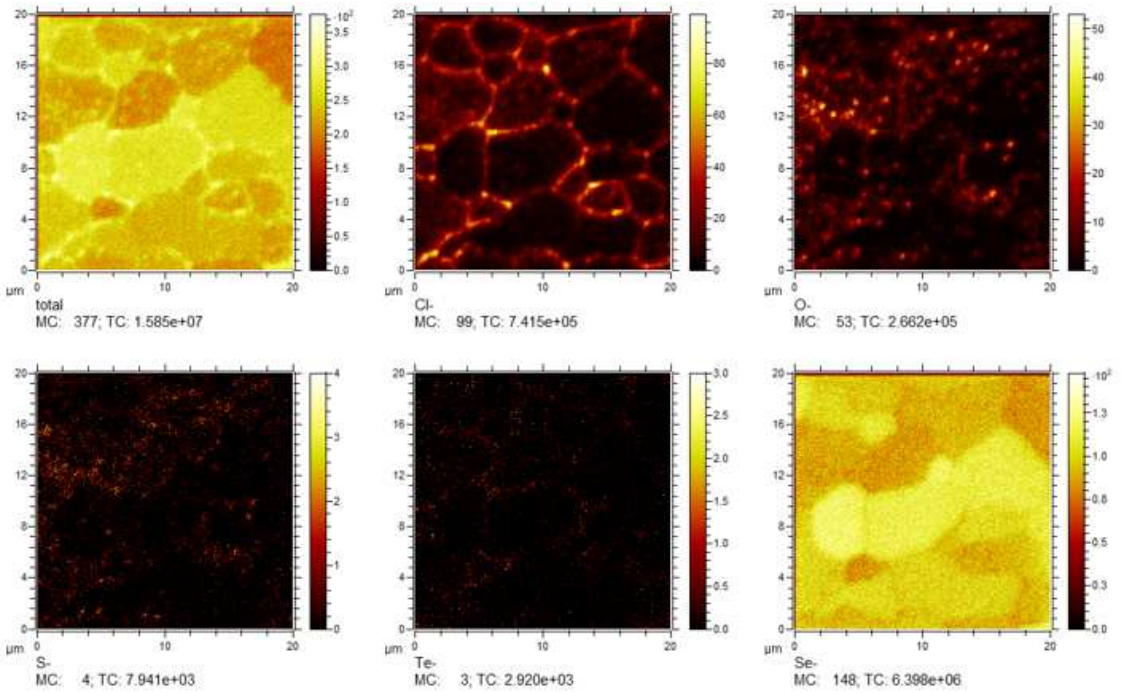

Figure 4.7: 2D mapping of Cl, O, S, Te, and Se from ToF-SIMS for a CdSe sample grown by VTD at First Solar.

The PL emission and TRPL lifetime of the absorbers grown at CSU following a wet CHT process is shown in Figure 4.8. The PL emission is found to be about two orders of magnitude greater than that of the as-deposited absorbers, with peak emission at 1.72 eV following CHT. The slightly reduced peak emission for as-deposited absorbers may be due to an increased density of defects which results in non-ideal absorption/emission. This is also seen through an increase in TRPL lifetime, indicating that the CHT process has reduced the density of defects and recombination centers within the lattice.

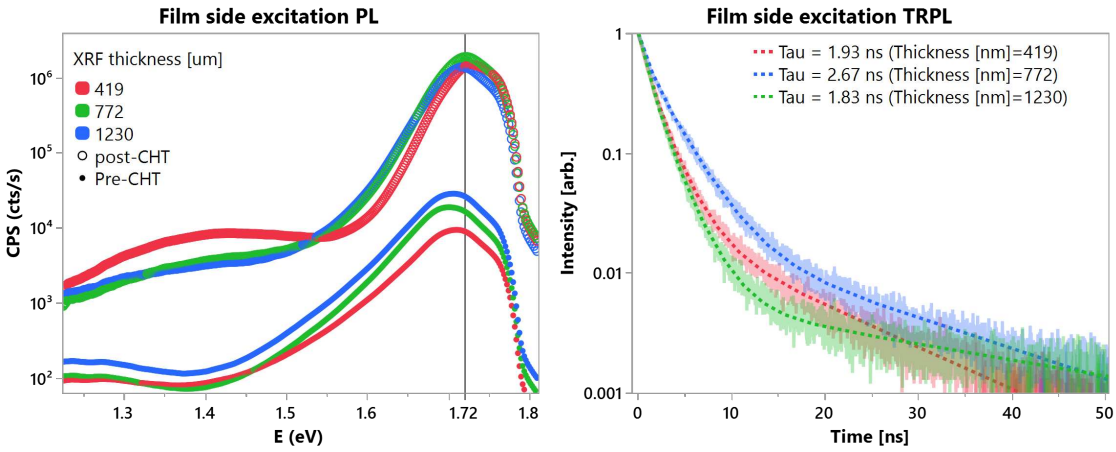

Figure 4.8: PL and TRPL measured on CdSe absorbers with various thickness. Subgap emission is noted to increase following the CHT process and appears to be greater in thinner absorbers. Lifetimes before CHT were in the picosecond regime and not shown in the figure.

These optoelectronic properties demonstrate that the CdSe absorbers grown at CSU have an ideal bandgap of ≈1.72 eV for tandem top-cell applications. As-deposited absorbers have low PL emission and lifetime in the picosecond range before a CHT step, indicating lattice disorder which may result in a high rate of recombination. Following CHT, an increase in grain size from submicron to > 5 microns on average results in PL emission increasing by ≈2 orders of magnitude and lifetimes increasing from the picosecond range to upwards of 3 ns.

4.3 CdSe Device Fabrication

This section will review the process of engineering devices using CdSe absorbers fabricated at First Solar with similar optoelectronic properties as the CdSe absorbers discussed above. The general requirements for materials used as charge transport and contact layers will be discussed in regard to the understood properties of CdSe absorbers and how that influences the development of high efficiency devices. This will lead to a review of the results of devices fabricated from First Solar CdSe absorbers before examining identical devices developed from the absorbers grown at CSU.

4.3.1 General Requirements for CdSe Device Fabrication

Given that CdSe absorbers are intrinsically n-type, and transparent conductive oxides (TCOs) used are all n-type, the formation of a pn-junction requires the deposition of some p-type layer onto the CdSe surface. This approach leads to the formation of a depleted region near the back of CdSe device, further from the glass side. Therefore, it is desirable to evaluate semi-transparent p-type transport layers and contact layers to facilitate excitation through the film side, allowing charge generation to occur within this depleted region.

To do so, wet solution coating of organic hole transporting layers (oHTLs) was explored, similar to work which has been done with CdSe by other institutions [48, 52, 53]. oHTLs are known to have high transparency in the visible region and can be simply deposited from solution [54], avoiding additional heating steps which may induce defect formation in the CdSe absorber. In this work, oHTLs were applied via spin-coating from liquid solution without additional additives to the solution following the CHT step. Evaporation of excess solvent and film solidification were achieved via an open-air hot plate anneal, schematically shown in Figure 4.9.

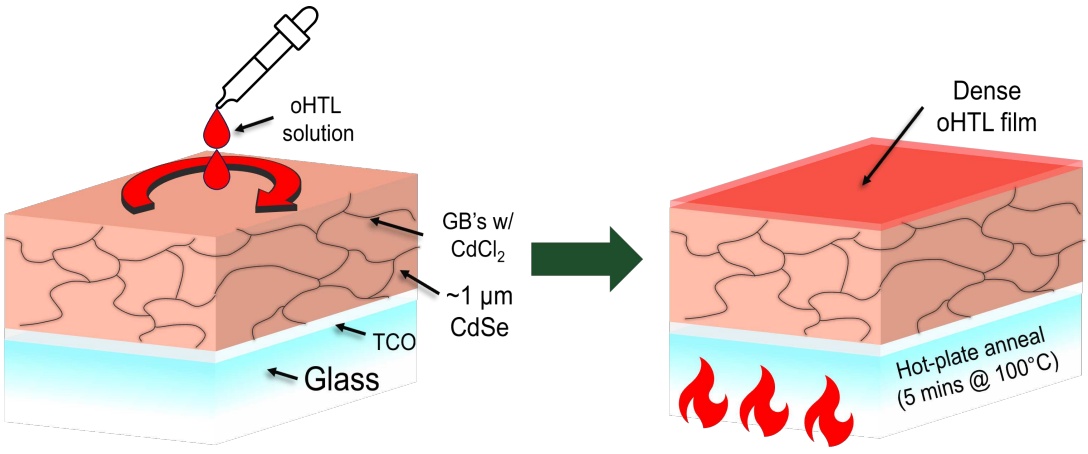

Figure 4.9: Schematic of the oHTL deposition process. The CdSe absorber is coated with a solution of oHTL and then placed on a hot plate to evaporate excess solvent and solidify the film.

Through this work, it was found that the oHTL poly(triaryl amine) (PTAA) provided the most consistently reproducible devices with diode rectification in the dark and photoconductivity when contacted with thin, semi-transparent 10nm gold (Au). PTAA is a well known organic semiconduc-

tor with a bandgap of ≈3.3eV and a valence band (or highest occupied molecular orbital (HOMO)) energy of ≈5.1eV, which is near the measured work function of CdSe absorbers seen through Kelvin probe force microscopy (KPFM). This however results in a large conduction band offset which will help to reduce electron conduction into PTAA, but also results in large valence band offset between CdSe and PTAA (> 1 eV) which may hinder hole conduction as well. Two other well known oHTLS, PEDOT:PSS and Spiro-OMeTAD, have similar optoelectronic properties as PTAA, but required solution additives, such as surfactants or organic dopants, to achieve similar performance to PTAA, making their application more convoluted and prone to reproducibility issues.

Evaluation of the concentration of PTAA solutions used for coating showed shunting for devices with concentrations less than 10 mg/mL, likely due to insufficient surface coverage of lower concentration solutions. Additionally, it was found that PTAA as an oHTL by itself results in devices with low efficiencies and particularly large voltage deficits, likely due to the large valence band offset between CdSe and PTAA. To address this, a novel approach using high a work-function transition metal oxide (TMO) between CdSe and the metallic contact, both with and without the oHTL layer.

TMOs, molybninum oxide (MoO_3) in this case, are deposited to the CdSe or CdSe/oHTL surface using a thermal evaporation process in an inert environment ($\approx 10^{-5}$ Torr nitrogen). MoO_3 has been appreciated as a viable hole transport layer in the organic and perovskite PV community [55,56]. An evaluation of the impact of changing TMO thickness revealed that an optimal thickness of 5nm, as measured by a quartz crystal monitor during thermal evaporation, provided the most consistently reproducible devices, where thinner layers (<5 nm) resulted in shunting and thicker layers (>5 nm) resulted in a large increase in series resistance [57].

Finally, a metallic contact composed of thermally evaporated gold (Au) was selected due to the large work function of Au (WF = 5.1 eV). This is done in the same vacuum evaporation system as TMO deposition, without breaking vacuum, to prevent oxidation of the TMO layer. The Au layer thickness was optimized to 10nm, which was found to be the best tradeoff between increased

transparency and reduced conductivity seen with reduced Au thickness. The JV results of devices with combinations of PTAA, MoO_3, and Au are shown in Figure 4.10.

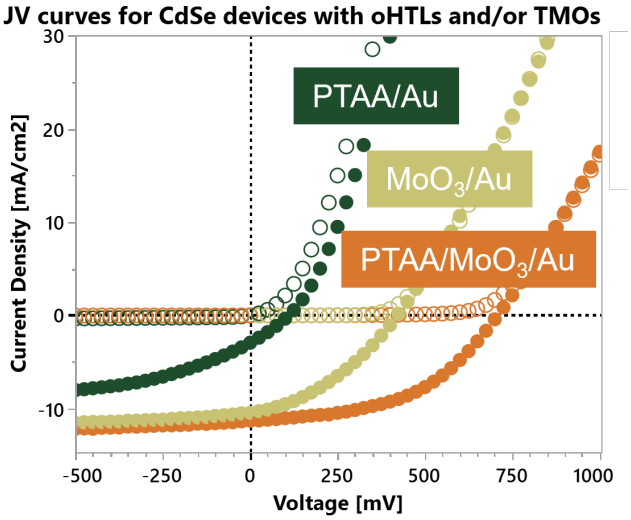

Figure 4.10: J-V measurments of CdSe devices with various oHTL and TMO layers. Best results are seen with the bilayer structure of PTAA/MoO_3 (orange), while devices with only PTAA (green) or MoO_3 (gold) show a large current and/or voltage deficit.

Devices using MoO_3 as an HTL without PTAA show increased performance with large gains in V_{OC} and J_{SC}. The surface work function of devices increased when MoO_3 is incorporated, from ≈5.1 eV for Au alone to ≈5.3 eV with MoO3/Au, which is correlated to a decreased dark saturation current (J_0) and thus increased V_{OC}. While these devices show an increase in performance, there is still a large V_{OC} deficit >1 V, possibly due to poor contact selectivity. MoO_3 had been selected as an HTL candidate due to the alignment of its conduction band with the CdSe valence band–which may be a reason why J_{SC} is seen to increase–but this does little to prevent recombination at the interface. Each sample shows equivalent ERE, 0.18±0.01%, but vastly different V_{OC}, likely a consequence of poor charge selectivity at the PTAA/Au or MoO3/Au interfaces alone.

The combination of PTAA as oHTL and MoO3/Au as a bilayer contact structure produces the largest V_{OC} near 750 mV and a slightly increased J_{SC}. This indicates that the large work function of the MoO_3 layer helps to mitigate the energy offset and potential chemical reactions between CdSe/PTAA and PTAA/Au respectively [58], while the PTAA layer may act as a passiva-

tion layer occupying dangling bonds at the CdSe surface and reducing interface trapping between CdSe/MoO_3.

The devices presented above were based on roughly 1 μm thick CdSe absorbers, and a clear difference in performance was noted for excitation from the glass-side vs film-side, which indicates poor diffusion lengths and trap mediated recombination in the bulk. The low J_{SC} seen in these devices is understood to be due in part to the semi-transparency and parasitic absroption of the Au, MoO_3 and PTAA layers.

4.3.2 CdSe Devices with Varied Absorber Thickness

The absorbers described in Section 4.2 were used to fabricate devices with various thicknesses to evaluate the effect of absorber thickness on device performance. Devices were fabricated using the previously described structure of FTO/CdSe/PTAA/MoO_3/Au, with absorber thicknesses ranging from ≈0.4 to 1.2 um. These devices were analyzed with JV under 1 sun excitation using typical AM1.5G spectrum from either the film-side or glass-side and with QE from the glass-side. Unfortunately, film-side QE measurements were not collected for these devices. JV results from each side are shown in Figure 4.11.

These measurements show a clear trend in J_{SC} with thickness, where current is inversely proportional to absorber thickness under glass-side excitation, but proportional to thickness under film side excitation. V_{OC} is seen to exceed 800 mV for the thinnest absorber from film-side excitation and decrease linearly with increasing absorber thickness. Glass-side V_{OC} does not have a trend with device thickness and is likely convoluted by non-ideal charge generation and transport in this configuration. The losses in J_{SC} from film-side excitation are likely due to the increased transparency for thinner devices, where devices less than 1 μm thick showed a transmission of roughly 5% at E_g which exponentially decreased with increasing photon energy. However, the low current from glass-side excitation may be explained by low charge mobilities in CdSe. While it is difficult to empirically measure carrier mobility in polycrystalline CdSe, it is expected that the mobility of charges in CdSe is < 1 $\frac{cm^2}{Vs}$. The large absorption coefficient (>10^4 cm^{-1}) of CdSe results in a

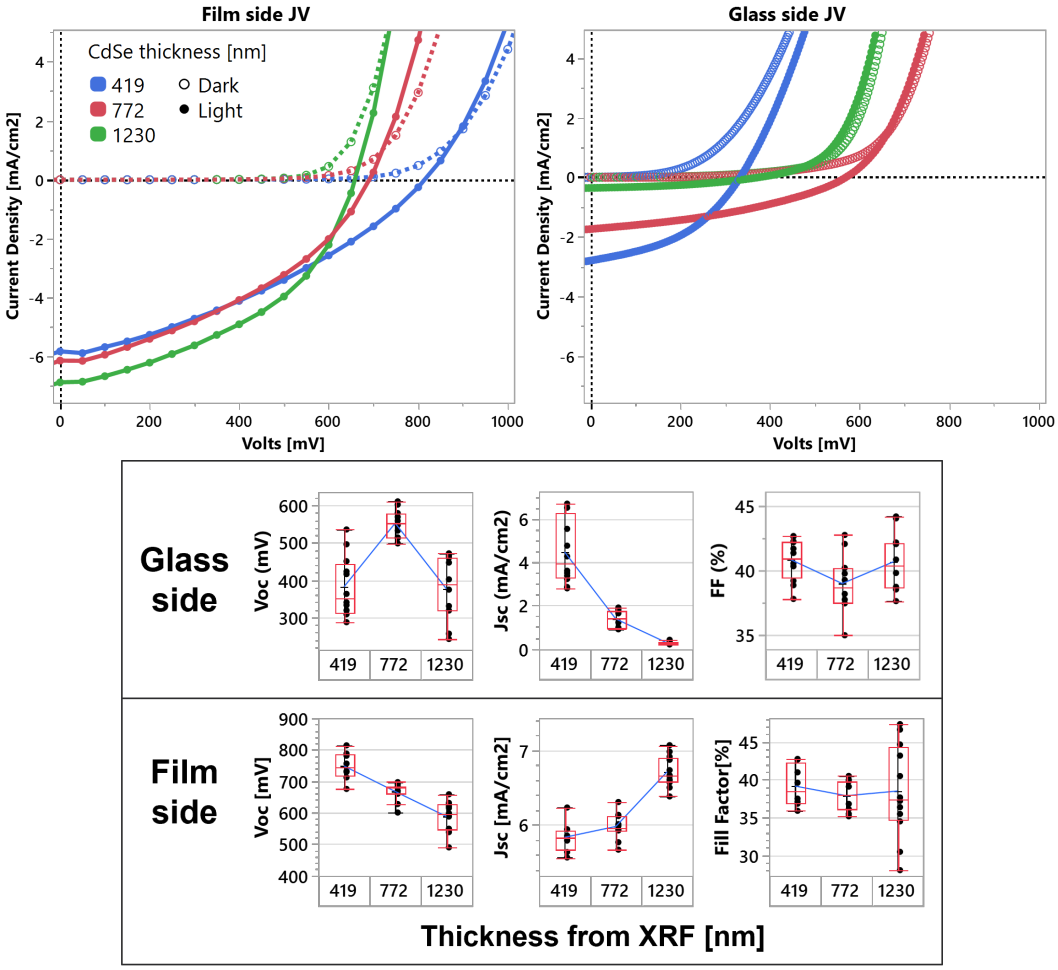

Figure 4.11: JV measurments of CdSe devices with various thickness with either film side or glass side excitation. The current is shown to be inversely proportional to thickness under glass side excitation, likely due to low diffusion lengths in CdSe, while proportional to thickness under film side excitation, likely due to an increased transparency for near bandgap photons as seen from Figure 4.3.

majority of photons being absorbed and generating charges within the first 100 nm from excitation incidence, which results in a majority of charges to be generated outside the depleted region. Thus, the current will be dominated by diffusion mediated charge transport, which is highly limited by carrier mobility, rather than drift transport.

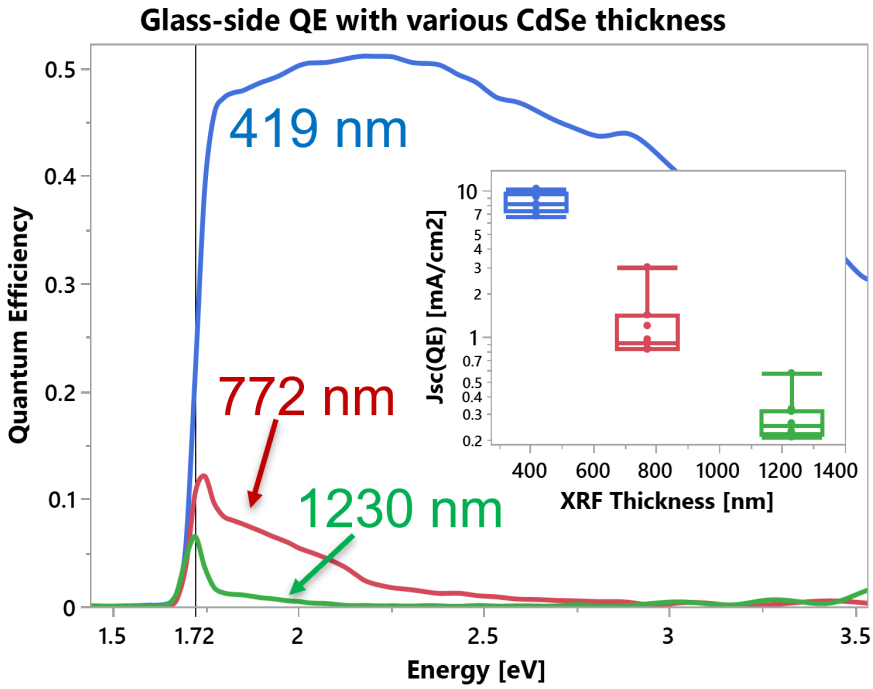

Figure 4.12: QE measured from glass-side for each device. J_{SC}(QE) calulated through integration of the QE is shown as an inset figure and demonstrates a similar trend to those seen in JV measurments.

This is further supported by glass-side QE meaurements of each device, shown in Figure 4.12. While QE tends to increase with decreasing thickness, all devices show a slope in QE which decreases with increasing photon energy. This is indicative of diffusion limited current collection, where the collection probability for charges decreases the farther they are generated from the junction that is expected to form at the back of the device. The increase in QE seen near 1.72 eV, which is the expected bandgap of these absorbers, occurs due to deep absorption which generates charges within the depleted region at that point, increasing collection probability. The extent of band tailing for each absorber was determined through a fit to the band edge from QE and is found to be

<20 meV on average of all thickness, indicating minimal lattice disorder within CdSe absorbers that were grown at CSU and subsequently given a wet CHT.

4.4 Voltage Losses in CdSe Devices

In the previous section, CdSe devices fabricated from absorbers grown at CSU were shown to be able to achieve moderately large V_{OC} up to 800mV when absorber thickness was reduced to around 500 nm. However, this is still a large deficit considering the bandgap of CdSe (ΔV_{OC} = E_g/q - V_{OC} $\approx$ 900 mV). In this section, the fundamental voltage limits of CdSe absorbers will be discussed before reviewing calculated voltage losses in various devices based on non-ideal absorption and bulk / interfacial recombination.

4.4.1 Fundamental Voltage Limits of CdSe

The Shockley-Queisser (SQ) limit defines the maximum theoretical efficiency of a solar cell based on its bandgap. For CdSe with a bandgap of about 1.7 eV, the SQ limit for the open-circuit voltage (V_{OC}^{SQ}) is approximately 1.4 V [59], which represents the maximum V_{OC} attainable in a device considering the principle of detailed balance. However, this principle considers the absorber to be perfectly absorptive, where no photons are absorbed for $E_{ph} < E_g$ and that all photons are absorbed for $E_{ph} > E_g$. This can be represented by a step function (Heaviside function) with

$$\alpha(E) = \begin{cases} 1 & E_{ph} > E_g \\ 0 & E_{ph} < E_g \end{cases} \tag{4.1}$$

where α(E) is the absorptivity of the material. Using this assumption, V_{OC}^{SQ} can be determined simply through the diode equation as follows:

$$
\begin{aligned}
V_{OC}^{SQ} &= A\frac{kT}{q}\ln\left(\frac{J_{SC}^{SQ}}{J_0}\right) \\
J_{SC}^{SQ} &= q\int_{E_g}^{\infty}\phi_{AM1.5G}(E)dE \\
J_0 &= q\int_{E_g}^{\infty}\phi_{BB}(E,T)dE \\
\therefore V_{OC}^{SQ} &= A\frac{kT}{q}\ln\left(\frac{q\int_{E_g}^{\infty}\phi_{AM1.5G}(E)dE}{q\int_{E_g}^{\infty}\phi_{BB}(E,T)dE}\right)
\end{aligned}
\tag{4.2}
$$

where A is the ideality factor, k is Boltzmann's constant, T is temperature, q is the fundamental charge, J_{SC} is the short-circuit current density, J_0 is the dark saturation current density and $\phi_{AM1.5G/BB}$ is the terrestrial solar spectrum and black body flux respectively. The limits of integration are set such that α(E) = 1.

In real devices however, the absorptivity is not a step function, and non-ideal absorption can occur due to various defects or impurities in the material. This is typically represented by an Urbach tail [23, 60], otherwise referred to as band tailing [61–64], and may be attributed to the formation of potential fluctuations within the absorber bulk as a result of lattice disorder [35, 36]. This is typically represented by an exponentially decaying modulation to $\alpha(E < E_g)$ as

$$
\alpha(E < E_g) = \alpha_0(E)e^{-\frac{E-E_g}{E_U}} \tag{4.3}
$$

where α_0 is material absorptance and E_U is defined as the Urbach energy which can be considered an approximation of the level of disorder within an absorber material. Single crystal absorbers typically have E_u on the order of 10meV, while polycrystalline absorbers have been shown to have a large range of E_u anywhere from 15 - 100s of meV [65]. This ultimately leads to a reduction in V_{OC}^{SQ} to the so-called radiative voltage (V_{OC}^{RAD}), which is the maximum V_{OC} achievable in a device considering non-ideal absorptance or radiative recombination and is defined as

$$
V_{OC}^{RAD} = A\frac{kT}{q}\ln\left(\frac{q\int_{E_g}^{\infty}\alpha(E)\phi_{AM1.5G}(E)dE}{q\int_{E_g}^{\infty}\alpha(E)\phi_{BB}(E,T)dE}\right) \tag{4.4}
$$

where $\alpha(E)$ is the real absorptance of the material, which is a function of both E_g and E_U. This is shown in Figure 4.13 where various degrees of band tailing are represented by increased E_U with indicated losses in V_{OC}^{RAD}. This shows that a critical loss in V_{OC}^{RAD} occurs when E_U approaches and exceeds thermal voltage at room temperature (kT = 26 meV). It should be noted that increased E_U has little impact on J_{SC}, as the AM1.5G spectrum is relatively flat near E_g, but J_0 is heavily impacted as the blackbody spectrum at room temperature increases exponentially with decreasing energy.

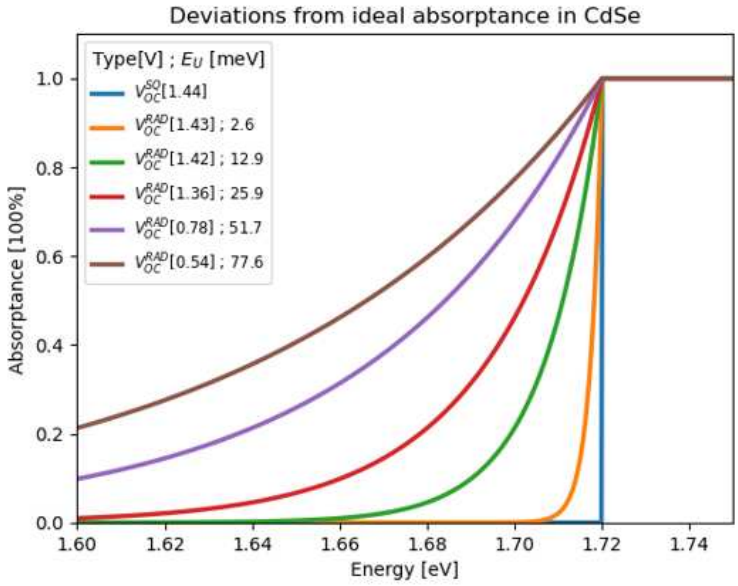

Figure 4.13: Calculated radiative open-circuit voltage (V_{OC}^{RAD}) for CdSe as a function of the Urbach energy (E_U), which is a measure of the extent of the band tailing in the density of states.

This provides a framework for understanding the losses in V_{OC} seen in CdSe devices. For comparison, V_{OC}^{SQ} for CdTe ($E_g \approx 1.5$ eV) and CdSeTe ($E_g \approx 1.4$ eV) is 1.21 and 1.12 V respectively [59]. This indicates that CdSe devices have the potential to achieve higher open-circuit voltages than CdTe devices, where high V_{OC} is understood to be a critically limiting factor in CdSeTe based photovoltaics.

4.4.2 Calculated Voltage Losses in CdSe Devices

CdSe absorbers in this section were grown at First Solar using vapor transport deposition, identical to that discussed in Chapter 2 and Chapter 3 but without any CdTe layer. After various optimizations in the post-deposition annealing step, absorbers with thickness around 500 nm were shown to achieve a high V_{OC} over 900 mV, with JV and QE shown in Figure 4.14. These devices were fabricated using the previously described structure of FTO/CdSe/PTAA/MoO_3/Au.

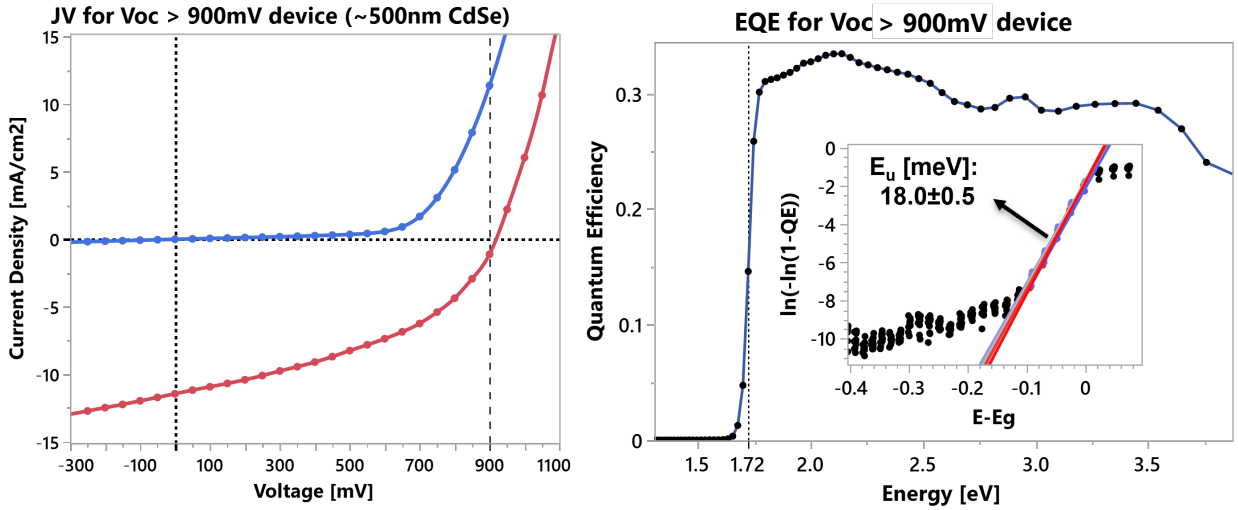

Figure 4.14: Film-side JV and glass-side QE measurements for CdSe device fabricated from thin absorbers grown by VTD at First Solar. Inset of QE curves show E_U fit to the bandedge.

A fit to the band edge of the QE presented results in a calculated E_U = 18.5±0.5 eV for 12 cells across the device. This is similar to the small E_U shown for devices fabricated from CdSe absorbers grown at CSU, indicating an inherent low disorder in CdSe absorbers possibly due to the fact that they are intrinsically n-type with no extrinsic doping (E_U less than 20 meV was also shown for intrinsic CdSeTe absorbers in Chapter 3). Such E_U results in a loss of approximately 30 mV and results in $V_{OC}^{RAD} \approx 1.39$ V.

Beyond radiative losses due to band tailing, non-radiative losses and contanct selectivity must be considered. It has been appreciated that non-radiative voltage losses (ΔV_{OC}^{nr}) are a primary factor for reduced V_{OC} seen in CdTe based solar cells [66], where non-radiative losses can be

accounted for through a measurment of the external radiaitve efficicny (ERE). ERE accounts for photons emitted per photons absorbed within the material, and is typically represented by

$$\text{ERE} = e^{\frac{q \cdot iV_{OC}}{kT}} \cdot \frac{\int \alpha(E)\phi_{BB}(E,T)dE}{\int \alpha(E)\left(\phi_{exc}(E) + \phi_{BB}(E,T)\right)dE} \tag{4.5}$$

where iV_{OC} is the implied V_{OC}, which is a measure of the quasi-Fermi level splitting (qFLS), and ϕ_{exc} is the excitation spectrum used during measurement. This can be rearranged to solve for iV_{OC} as

$$iV_{OC} = V_{OC}^{RAD} - \frac{kT}{q}|ln(\text{ERE})| \tag{4.6}$$

where ERE is represented as a percentage. ERE was measured for devices at First Solar using a similar apparatus as that which has been previously described [67] composed of a 532nm laser which is chopped before being split to a power meter and the sample under test, with emission collected by a Si detector and analyzed by a lock-in amplifier referenced by the chopper. The resulting ERE was found to be approximately 4 X 10^{-3}% for the high V_{OC} sample shown in Figure 4.14, which is similar to ERE values measured for many other CdSe samples. This leads to a calculated iV_{OC} of approximately 1.26 V with non-radiative voltage losses of 144 mV (ΔV_{OC}^{nr} = kTln(ERE) $\approx$ -144 mV).

The remaining voltage deficit is typically attributed to contact selectivity [68, 69] which is defined as the ratio between V_{OC} and the ideal V_{OC} (S = V_{OC} / iV_{OC}). This would lead to a calculated S = 0.71 (71%) which indicates that the remaining voltage deficit may be due to poor contact selectivity at any of the CdSe/PTAA/MoO_3/Au interfaces. In the next section, these results will be further reinforced through absolute photoluminescence (PL) measurements of CdSe absorbers, which will be used to determine the real absorptance spectrum and to provide insight into what factors may be contributing to poor contact selectivity.

4.4.3 Absolute Photoluminescence of CdSe Absorbers

To empirically determine voltage limits in CdSe, absorptance for CdSe thin-films was determined through the method of absolute photoluminescence [70] making using to a spectrally calibrated system with coupled Si and indium gallium arsenide (InGaAs) detectors with a spectral range down to roughly 0.8 eV. The PL spectrum for a CdSe thin-film of roughly 600 nm thickness is shown in Figure 4.15. This spectrum, showing the same 1.7 eV peak emission and 1.4 eV defect emission seen in various other CdSe devices, also reveals the presence of a large defect peak near 1.1 eV which was previously unseen due to the sensitivity limits of Si detectors. Before determining the impact that these defect states have on CdSe, the qFLS is estimated via Wurfel's generalized Planck law [71] whereby a linear fit to the high energy side of the PL emission gives a slope proportional to the device temperature and an intercept which is the qFLS. Doing so reveals that T = 323 K, which gives confidence to the results as they were measured at room temperature, and iV_{OC} = 1.14 V for this film, which is $\approx$ 150 mV less than the iV_{OC} calculated from ERE of the 900 mV device. This is likely due to the presence of the deep defect near 1.1 eV which was not accounted for in the measurement of ERE, thus we can assume that the iV_{OC} calculated from the PL spectrum is a more accurate representation of the qFLS in CdSe. Additionally, the PL quantum yield (PLQY) for this sample was determined to be 2 x 10^{-4}%, which is lower than the ERE measured by an order of magnitude.

From the above calculated iV_{OC} and T, $\alpha(\lambda)$ is calculated for photons with E < E_g through a reorganization of the generalized Planck law as

$$\alpha(E) = I_{PL}(E)\frac{h^3c^2}{2\pi E^2}\left[\exp\left(\frac{E - iV_{OC}}{kT}\right) - 1\right] \tag{4.7}$$

where I_{PL}(E) is the PL spectrum, h is Planck's constant, and c is the speed of light. The resulting absorptance spectrum is also shown in Figure 4.15 in red. With this spectrum, we estimate the Urbach edge energy through a linear fit to the band edge over 70 mV (1.65-1.72 eV). This Urbach edge energy is determined to be $\approx$ 16 meV, well below thermal energy and indicates high quality absorbers. Using the E_U from the absorptance spectrum above results in $V_{OC}{}^{RAD}$ = 1.4 V

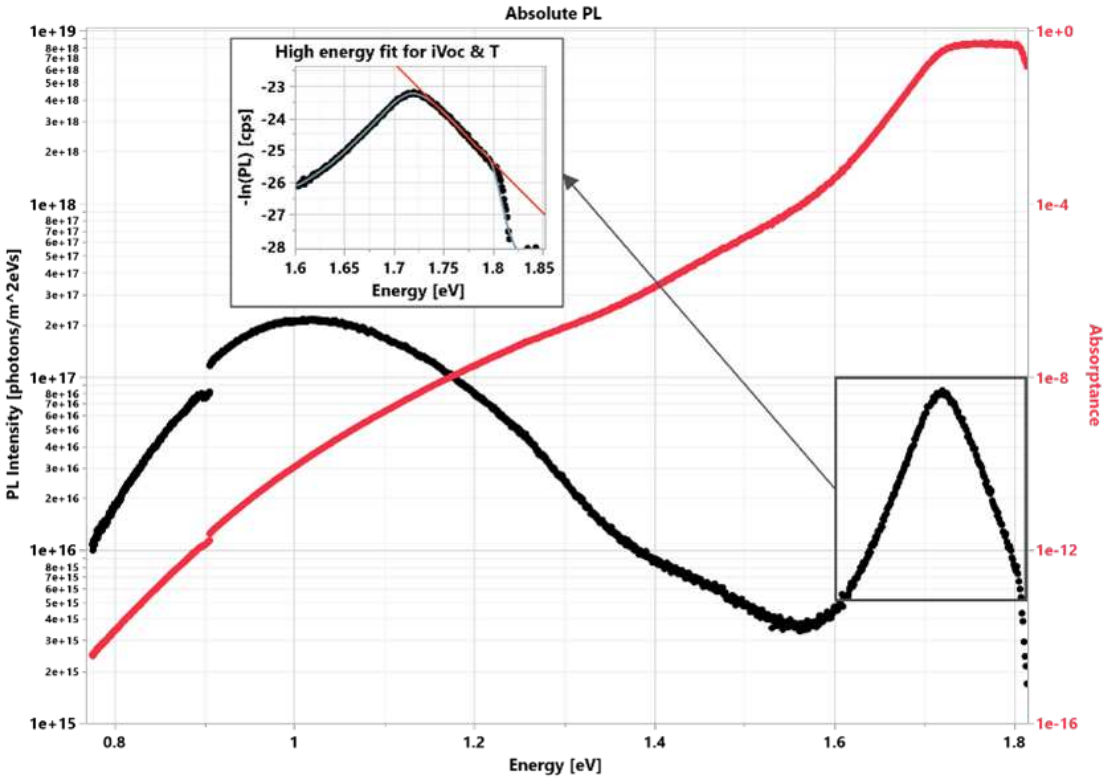

Figure 4.15: Absolute photoluminescence spectrum of CdSe thin films. The spectrum shows the presence of a large defect peak near 1.1 eV, as well as a smaller defect peak near 1.4 eV. The peak emission at 1.7 eV is consistent with the bandgap of CdSe. Quasi-Fermi level splitting (qFLS), also known as the implied V_{OC}, is determined from the slope of the high energy side of the PL emission.

for a 600-nm CdSe samples. Using this along with the PLQY (which can be substituted for ERE when using absolute PL) results in a calculated iV_{OC} = 1.17 V, which is in close agreement with the value determined from the fit to the high energy side of the PL spectrum. This indicates that non-radiative recombination is more significant than radiative recombination in these devices, but that the so-called contact selectivity is the primary limiting factor to V_{OC}. This analysis was done on a CdSe absorber rather than a completed device, and the presence of deep defect states indicates that certain recombination processes are occurring within the CdSe bulk. To determine how these defect states impact device performance, temperature and intensity dependent PL and TRPL were performed on the same sample in addition to a second sample with a different thickness. The results of these measurements are shown in the following section.

4.4.4 Temperature and Intensity Dependent Measurements of CdSe

Two CdSe absorbers with different thicknesses were analyzed using temperature and intensity dependent PL and TRPL to determine the impact of defects on device performance. Sample S2 was a roughly 600 nm thick absorber, which is the absorber shown in Figure 4.15 and discussed previously, and sample S1 was a 1.2 μm thick absorber. Both samples were grown with the same VTD process as described previously on TCO coated glass and received a wet CHT prior to analysis. The PL spectrum measured under 1 sun excitation with a 633 nm He-Ne laser at room temperature for both samples and at 4 K (achieved with a closed loop He crystat) for S1 is shown in Figure 4.16. These samples show a peak at the expected bandgap of $\approx$ 1.7 eV in addition to the two defect peaks at 1.4 eV (D1) and near 1.1 eV (D2), as was previously seen in Figure 4.15. PLQY for these samples was determined to be 2 X $10^{-}4$ and 5 X 10^{-5} for S1 and S2 respectively. Absorptance spectra for each sample calculated using equation (4.7) is shown as an inset in the room temperature PL spectrum. A fit along the bandedge of the absorptance results in $E_U \approx$ 11.5 meV for S1 and 15.8 eV for S2, indicating that the thinner absorber does have some degree of additional disorder, possibly due to a larger concentration of selenium vacancies as was indicated by the reduction of Se seen in XRF analysis of absorbers grown from CSU in Figure 4.3. Nonetheless,

both absorbers show a low E_U which is consistent with the low E_U seen in other CdSe absorbers and indicates that these absorbers are of high quality. In fact, the 11.5 meV E_U is among the lowest values reported for polycrystalline semiconductors [72], only surpassed by certain single crystal absorbers [73–75], and speaks to the merits of CdSe.

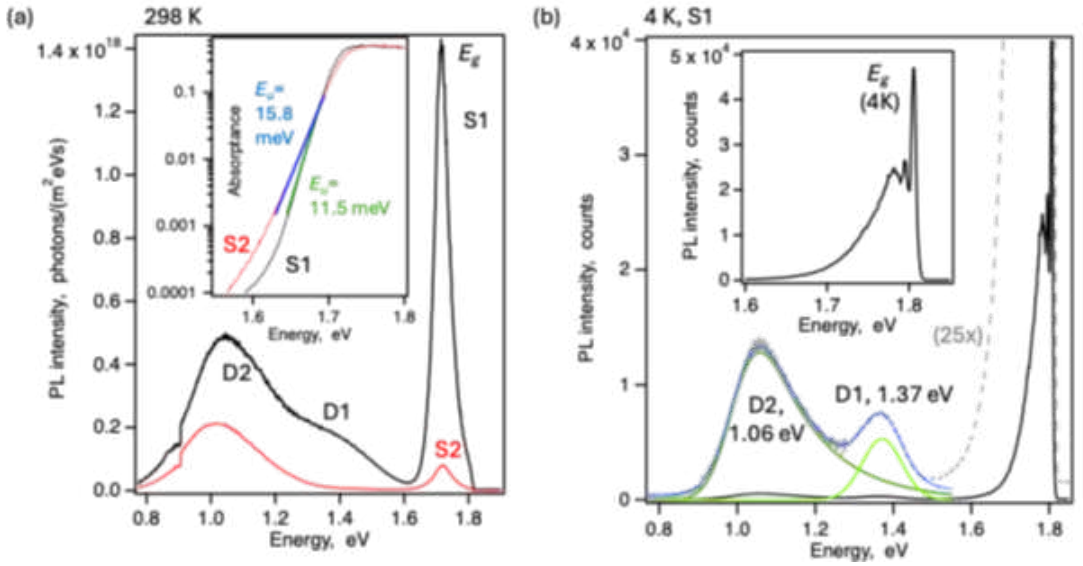

Figure 4.16: Absolute photoluminescence spectrum of CdSe thin films at (a) room temperature with an inset of the calculated absorptance spectrum and (b) at 4 K for the thicker sample S1 with inset of the near bandgap region.

The low temperature (4 K) PL spectrum for S1 (1.2 μm sample) provides insight into the dynamics of defect states. At low temperature, D1 and D2 become more distinctly separated, where deconvolution of the full spectrum shows D1 peaks at 1.37 eV and D2 peaks at 1.06 eV. Defects near this energy have previously been ascribed to selenium vacancies (V_{Se}) and oxygen substitution of Se (O_{Se}) respectively [76], both of which are possible here considering the high vapor pressure of Se and the presence of oxygen during the CHT process. The FWHM of D2 has a small shift from 258 meV at room temperature to 213 meV at 4 K while D1 narrows significantly from 366 meV to 119 meV, indicating that D1 is likely a shallow defect as broadening of the defect peak at low temperature can be attributed to increased defect to band transitions. The temperature dependence for these defects is shown in Figure 4.17 from 4 K to 300 K where PL excitation used

here was with a 442 nm He-Cd laser. Defect D1 is shown to roughly double in intensity up to 100 K before quenching, where an Arrhenius fit to this data results in a thermal activation energy (E_a) of 130±20 meV, which is in close agreement to that shown previously for a defect at 1.35 eV [76] and provides further insight into the assignment as a shallow defect. Defect D2 however was determined to have an activation energy of 800 meV, indicating it is likely a midgap defect state near the midgap.

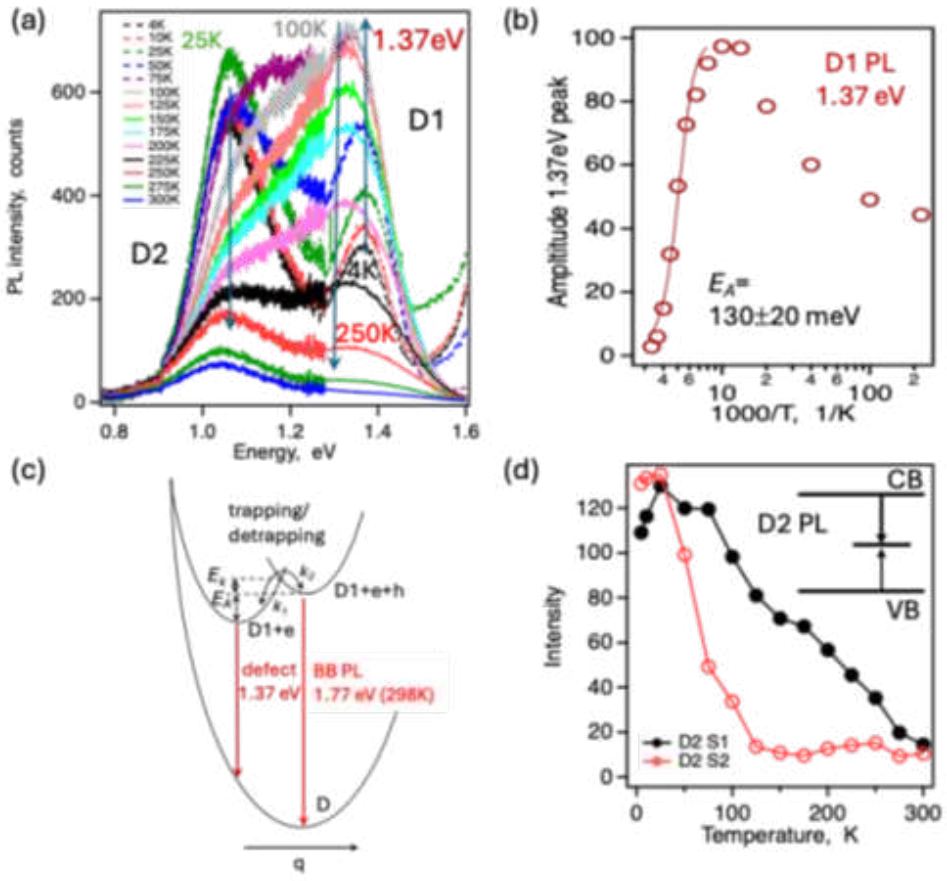

Figure 4.17: Results of defect emission measurements. (a) Temperature dependent subgap emission for sample S1. (b) Fitting of the thermal quenching of defect D1 at high temperatures to determine E_a. (c) Schematical configuration diagram demonstrating hole capture by defect D1. (d) Defect emission intensity as a function of temperature assigning D2 as a midgap defect.

To further understand these assignments and the kinetics of trapping by these defect states, intensity and temperature dependent TRPL, shown in Figure 4.18 was performed for S2 using a

450 nm ytterbium-doped potassium gadolinium tungstate (KGW:Yb) laser with 300 fs pulses at 1.1 MHz.

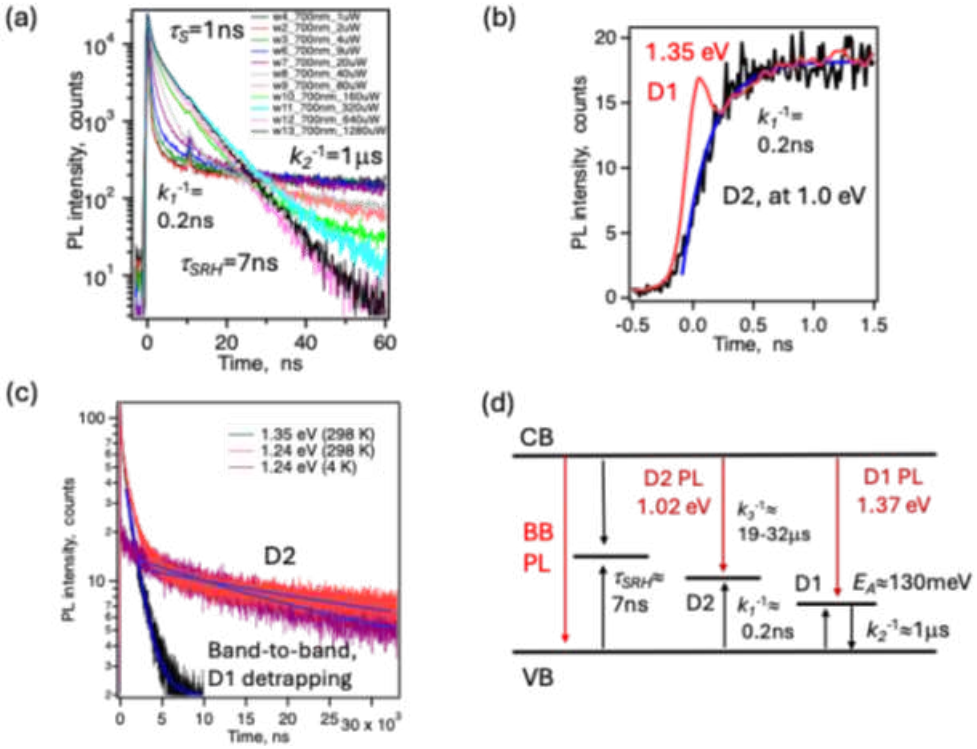

Figure 4.18: Intensity dependent carrier dynamics determined from TRPL. (a) CdSe bandgap TRPL over a range of fluences. Inverse rate constants shown indicate the fast initial decay (k_1), the long quenched lifetime resulting from trapping (k_2) and the single exponential lifetime after trap saturation (t_{SRH}) (b) Quenching of PL intensity for traps D1 and D2 with same rate as quick bandgap TRPL (c) TRPL for defect D1 and D2 at room temperature and 4 K. (d) A schemattic band diagram representing trapping dynamics relative to the conduction and valence bands.

First, the bandgap TRPL (measured at 700 nm) shows an initial fast decay of 0.2 ns and a slow tail decay of 1 μs (inverse rate constants $k_{1/2}^{-1}$) with low fluence injection. The fast decay rate is shown to match the quenching rate in PL emission for both defects D1 and D2, indicating that this fast decay is due to trapping at these defect sites. Given that CdSe absorbers are n-type (majority carriers are electrons) it is likely that these defects reside closer to the valence band than the conduction band, as low fluence dynamics are dominated by minority carriers (holes). As the fluence is increased, these defect sites become saturated and the bandgap lifetime approaches a single exponential decay with a lifetime of 7 ns which is assigned to Shockley-Reed-Hall (SRH) recom-

bination at an arbitrary midgap state for the bare absorber films. The density of traps is estimated to be roughly 5-50 X 10^{17} cm^{-3} based on the fluence at which the bandgap decay approaches single exponential and thus the trap states are saturated (fluence = 6 X 10^{13} photons per cm per pulse).

TRPL for defects at room temperature is shown for both D1 (measured at 1.35 eV) and D2 (measured at 1.24 eV due to sensitivity of Si detector) and at 4 K for D2. Defect D1 shows a single exponential decay with a lifetime of 1 μs which matches the slow tail lifetime from bandgap emission, which is attributed to hole emission from D1 to the valence band. D2 however showed a longer lifetime of about 25 +/- 7 μs at room temperature and 4 K, which is typical for deep trap states and is unlikely to contribute to photocurrent. These results are summarized by use of four rate constants as such: k_1 for quick carrier capture from the valence band to trap states D1 and D2, k_2 for hole emission from trap D1 to the valence band, k_3 for slow electron capture from the conduction band to trap D2, and $k_{SRH} = \tau_{SRH}$ to describe SRH recombination dynamics.

As discussed previously, the majority of voltage deficit in CdSe devices was attributed to low contact selectivity. The dynamics of charge trapping described here helps to understand why this may be so. The change in initial TRPL decay at the CdSe bandgap indicates that the surface recombination velocity is less than 10^4 cm^{-3}, indicating that recombination at the interfaces between CdSe and transport layers is likely less dominate than bulking trapping due to τ_{SRH} lifetimes around 7 ns. This can be shown through analysis of the impact that trapping has on diffusion lengths in CdSe absorbers. Hole mobilities in CdSe are estimated to be upwards of 25 $\frac{cm^2}{Vs}$ which can be used with the measured τ_{SRH} of 7 ns to determine minority carrier diffusion length with $L_d = \sqrt{D_h \tau_{SRH}}$ where $D_h = \frac{kT}{q}\mu_h$. This results in a diffusion length up to 700 nm but does not account for trapping from the valence band to states D1 and D2. To account for this, the reduction in carrier mobility is determined by

$$\mu_{trap} = \mu_h \left[1 + \frac{N_t}{N_v} exp\left(\frac{E_a}{kT}\right)\right]^{-1} \tag{4.8}$$

where N_t is the density of traps, N_v is the density of states in the valence band, and E_a is the activation energy for trapping [40]. This results in a reduction in μ_h by roughly 30X leading to a

reduction in diffusion length down to L_d = 150 nm at most. This greatly limits the collection for carriers at contacts in CdSe and is exemplified in reduction for collection probability in QE, where QE measured from the glass-side was seen to decrease exponentially with increasing thickness, and even 400 nm thick CdSe devices show a reduced collection probability for higher energy photons which generate charges further from the junction under glass-side excitation.

4.5 Conclusions

CdSe absorbers grown by close-space sublimation at CSU and by vapor transport deposition at First Solar were shown to have large bandgaps near 1.7 eV and high absorption coefficients greater than 10^4 cm^{-3}, making CdSe and ideal candidate for tandem top cell applications. Regardless of the deposition technique, CdSe absorbers tend to have sharp band edges and high radiative efficiency, resulting radiative and non-radiative voltage losses less than 200 mV, which would indicate the potential to achieve high V_{OC} near 1.2 V. However, subgap emission near 1.4 eV, in addition to around 1.1 eV seen with use of InGaAs detectors, was also seen in CdSe absorbers regardless of deposition technique. This indicates some inherent defects within CdSe which may act as a limiting factor to device performance.

Through development of devices making use of organic hole transport layers and high work function transition metal oxides with thin semi-transparent metallization, V_{OC} upwards of 900 mV was achieved with efficiencies approaching 5%. This was seen to occur as absorber thickness was reduced to near 500 nm, but also resulted in a loss in J_{SC} due to partial transparency for photons with energies close to the bandgap. The roughly 300 mV difference between expected voltage and measured voltage was attributed to poor contact selectivity, which was shown to be a symptom of trap related diffusion length limitations with trap states on the order of 10^{17} cm^{-3} resulting in low diffusion lengths less than 200 nm. It is for this reason that thinner CdSe devices were able to achieve larger voltages, but a careful balance must be struck between the increase in V_{OC} and the loss in J_{SC}. In order to further the development of CdSe based photovoltaics, more work must

be done to reduce the density of trap states which have been attributed to selenium vacancies and oxygen substituting selenium sites.

CdSe remains a promising candidate for tandem top cell applications, with V_{OC} greater than 900 mV reported here and J_{SC} greater than 85% of the theoretical maximum [77] having been reported by other institutions making use of proper transparent back contacts such as ITO. Combining these two factors together may be a pathway towards furthering device efficiency. However, the use of organic hole transport layers has been ubiquitous in modern CdSe devices [47, 48, 53], which has resulted in limited fill factors typically less than 50%. This is a strong indication that more work needs to be done in switching to inorganic hole transport layers, which should have lower bulk resistivity and thus greater charge mobilities than organic materials.

Chapter 5

Conclusions and Future Work

CdTe remains a critical technology in the renewable energy sector, accounting for a majority of PV manufacturing in the US. As CdTe based PV continues to mature, device architectures are becoming increasingly complex, which has led to many factors that may be competing with each other to allow for further advancements. This thesis has generally focused on the role of Se in CdTe based devices in conjunction with a variety of dopants. The use of Se alloying in CdTe devices allows a modulation of the energy band levels in $CdSe_XTe_{(1-X)}$ (CST), where the optical bandgap can be reduced from roughly 1.5 eV to 1.4 eV when X $\approx$ 0.3 ($CdSe_{0.3}Te_{0.7}$: 30% Se and 70% T) and further increased to roughly 1.7 eV when x = 1 (CdSe : 100% Se and 0% Te). This allows CST manufacturing to provide for both ideal single junction devices and fill the role of yet-to-be-realized mature tandem top-cell devices.

5.1 Group-V Doped CST Summary

The use of group-V doping in CdTe PV was investigated to understand factors which may be limiting their success. First, an examination of the annealing parameters used during the chlorine passivation was performed to determine the best conditions to produce high efficiency (20%) devices. Absorbers consisting of a bilayer of thin CdSe and thick CdTe were ex-situ doped with arsenic (As) through wet solution deposition onto the CdTe surface prior to a chlorine anneal step. By holding the concentration of dopant in solution (As in this case) constant and varying the annealing environment and crucible, secondary ion mass spectroscopy (SIMS) analysis revealed that dopant concentration in the bulk was reduced during anneals with potential oxygen exposure, indicating that interactions between oxygen and group-V dopants may be a factor limiting successful doping. Devices with similar concentrations of oxygen and group-V dopant in the bulk were limited to roughly 10% efficiency at best. Through iterative work in removing oxygen content and cleaning crucibles used during annealing, devices with efficiencies greater than 15% were

achieved, with J_{SC} near 30 mA/cm^2 approaching the theoretical maximum. However, these devices had a low dopant activation ratio less than 0.5%, resulting in a moderately low fill factor of roughly 70% and V_{OC} about 750 mV. By reducing the concentration of group-V dopant in the ex-situ solution based process roughly 12X, the density of acceptors was seen to stabilize around 1-5 X 10^{16} cm^{-3} while the activation ratio was found to increase up to 2.5%. Doing so enabled device efficiencies to approach 20% through increased fill factor of roughly 80% and V_{OC} around 850 mV. This provided insight into the factors which were previously limiting device performance due to overdoping, where excessive incorporation of dopants into CdTe increases the probability of compensating defect formation, leading to increased bandtail states that reduce voltage.

A novel method to increase group-V dopant activation intended to prevent oxidation of group-V dopants through use of oxygen getters was presented. In this work, the same bilayer CdSe/CdTe absorbers were used with phosphorus ex-situ doping. Phosphorus was selected for this work, rather than arsenic, as the probability for phosphorus oxidation is greater than that of arsenic and the use of phosphorus doping has allowed for the most recent record efficiencies with V_{OC} slightly above 900 mV. As such, there is much interest in understanding factors which limit continued improvement with P-doped CST. Elements with a greater probability of oxidation relative to phosphorus, in particular silicon (Si) and aluminum (Al), were ion implanted into the back of CST to a depth of 200±100 nm prior to ex-situ doping and chlorine annealing. Ion implantation allowed the introduction of oxygen getters into the CdTe bulk in their ionic form, where they are free to reduce oxidation of phosphorus. Indeed, SIMS analysis of as-implanted absorbers indicated successful getter incorporation, and following absorber annealing and device integration, devices with oxygen getters were shown to have a reduced concentration of phosphorus oxide throughout the bulk. This translated to a moderate increase in dopant activation from roughly 0.4% to 2.1% with Si as an oxygen getters and 0.6% to 3.5% with Al as an oxygen getter, where P-doped CST has tended to have dopant activation less than 1%. However, this did not improve device performance in practice, indicating that while the methodology of reducing group-V oxides can increase activation, the process of ion implantation needs to be reevaluated and refined.

To further understand what factors may be contributing to compensating defect formation, devices made from intrinsic CST absorbers were evaluated. In this case, intrinsic CST absorbers were compared to absorbers which were n-type doped (Al) and p-type doped (P or As). These absorbers were all given the same chlorine anneal and devices were integrated using a p-type ZnTe buffer and transparent back contact structure. Scanning kelvin-probe force microscopy (KPFM) was used to determine the location of the peak field strength, and thus the location of pn-junction within each device. This revealed that the intrinsic CST device has a pn-junction formed between the CST and p-type ZnTe, just as the Al-doped devices, while the group-V doped devices were found to have a pn-junction between the n-type TCO and CST, as is expected for a p-type CST. This showed that CST is intrinsically n-type, unlike CdTe which tends to be intrinsically p-type.

Through complimentary superstrate and substrate JV and QE analysis, intrinsic CST devices were shown to perform best in substrate mode, where excitation is incident on the film side resulting in a majority of charge generation to occur within the depleted region formed by the CST/ZnTe interface. It was also shown that carrier lifetimes are increased in n-type CST absorbers relative to p-type absorbers when injection is from the film-side, likely due to quick separation of charge pairs generated within the depleted region. The collection probability in QE measured from the film-side was flat over a large range of energies for the intrinsic absorber, but showed a negative gradient toward high energies for the Al-doped device, indicating ex-situ n-type doping limited collection probability. Additionally, the Urbach energy for all ex-situ doped devices was larger than the intrinsic device, which showed $E_U < 20$ meV. This all results in intrinsic devices with efficiencies approaching 8% from the film-side. Most interestingly however, CV analysis showed that the charge concentration between the Al-doped and intrinsic CST absorbers was nominally identically, bringing to question what the source of donor defect formation in these n-type absorbers was. To understand this, intrinsic CST devices with uniform concentrations of Se at various levels (X=0, 0.15, and 0.3) were compared to those with a graded Se concentration. This revealed that the concentration of donor states in intrinsic CST increases from less than 10^{16} for X = 0 to greater

than 10^{17} when X = 0.3, indicating that Se itself is a major contributor to n-type conversion and may be a source of defects which compensate the use of group-V dopants.

5.2 Future Work in Group-V Doped CST

The use of oxygen getters for group-V dopant activation requires greater attention to determine if it is a viable method for increasing group-V dopant activation. For one, the use of ion implantation in this work was performed with limited number of elements to act as oxygen getters and with limited evaluation in changing the processing parameters of the implantation itself and post-processing conditions. Additionally, the use of SIMS to determine the distribution of oxide species needs further attention to understand the extent to which various oxide species are forming under differing process conditions. Beyond this, alternative methods of oxygen gettering should be explored which are not as prohibitive and potentially destructive as ion implantation.

Greater detail in the way in which dopant activation is determined, and it's impact on device performance, should be addressed as well. SIMS analysis for quantification of dopant concentration provides information on a small region of the absorber bulk, while CV analysis is assumed to provide information on the charge concentration within the depleted region of a full device. Yet, the electric fields measured on the cross-section of devices in scanning kelvin-probe force microscopy has been seen to fluctuate around the depleted region, particular in the case of phosphorus doping [78]. A more accurate accounting may be made through a 3D mapping of the distribution of dopants throughout the bulk with methods such as atom probe tomography combined with more accurate mappings of the distribution of charge carriers within the depleted region.

While it has been somewhat appreciated by the CdTe community recently, the intrinsic n-type nature of CST absorbers deserves greater attention, both in regard to its impact on group-V doping activation and for its potential to be used as an n-type absorber layer itself. The p-type conversion process in CdTe photovoltaics has posed many problems over the years, not the least of which is the stagnation of progress in increasing V_{OC}. The largest voltages reported (greater than one volt) have been from the single crystal community using n-type CdTe which was doped with indium and

made use of CdMgTe buffer layers. In this work, 7% efficient devices with J_{SC} around 17 mA/cm^2 were achieved using graded Se absorbers with a concentration gradient reducing towards the back interface. As such, the lifetimes measured from the film-side for intrinsic devices were quite low (less than 1 ns) albeit larger than that of the p-type absorbers. Work to reverse the Se gradient, increasing from the back to the front of the devices instead, may afford n-type CdTe devices further increased carrier generation and carrier lifetimes within the depleted region, both of which should translate to an increased J_{SC} and V_{OC} for such devices.

5.3 CdSe Device Summary

CdSe growth at CSU using close-space sublimation (CSS) was explored through deposition of CdSe at thicknesses ranging from roughly half a micron to 1.5 microns. Analysis of the absorption onset and peak emission of these absorbers showed a large bandgap of $\approx$ 1.7 eV for all thicknesses, which is ideal for use as a tandem top-cell. As with CdTe based absorbers, CdSe was seen to benefit from a chlorine treatment which increased grain sizes, peak emission, and carrier lifetime. However, unlike CdTe, CdSe is highly n-type and has a deep ionization potential with the valance band reside around 6 eV. This required an intensive evaluation of materials for device integration which allow both the formation of a pn-junction and are semitransparent to allow film-side excitation. Ultimately, the use of organic hole transporting materials, namely PTAA, and transition metal oxides, namely MoO_3, were shown to result in the best device performance with efficiency approaching 5% and V_{OC} greater than 750 mV. The absorbers grown at CSU were integrated into devices with this structure and shown to have V_{OC} up to 800 mV as absorber thickness decreased. It was seen that both radiative and nonradiative losses in these absorbers was quite low (less than 200 mV combined) and that the largest loss from ideal V_{OC} (roughly 1.4 V here) was attributed to poor carrier selectivity. This provided insight into the potential that thicker absorbers were losing voltage due to diffusion length limitations, which was supported by the observation of voltage-dependent current collection in these devices.

Through iterative work in decreasing the absorber thickness and optimizing the annealing processes with VTD deposited CdSe from First Solar, CdSe devices were shown to achieve V_{OC} greater than 900 mV. However, this represents only 64% of its theoretical maximum. To further understand factors contributing to poor contact selectivity temperature and intensity dependent PL/TRPL measurements were explored. This work identified two subgap defects at roughly 1.4 and 1.1 eV, which have historically been associated with selenium vacancies and oxygen substituting selenium respectively. Evaluation of flueance dependent TRPL at the CdSe bandgap showed a quick quenching of carrier lifetime with decay time of 0.2 ns and extended tail lifetime of 1 μs. This was attributed to trapping by the 1.4 eV defect, which was shown to be a shallow defect with activation energy of roughly 130 meV, and TRPL analysis of CdSe at the 1.4 eV defect demonstrated the same 0.2 ns lifetime. By identifying the flueance at which the bandgap lifetime approached a single exponential decay, and thus trap stats were saturated, the density of traps in a 500 nm thick CdSe absorber was determined to be on the order of 10^{17} cm^{-3}. This all resulted in the determination of low diffusion lengths less than 150 nm in CdSe absorbers, where quick trapping in the picosecond scale and slow detrapping in the microsecond scale limits mobility. This is one reason why thinner devices may be able to perform better and were able to achieve V_{OC} greater than 900 mV.

5.4 Future Work in CdSe Devices

Continued research into the development of devices based on n-type CdSe is warranted, as the current use of organic hole transport layers is one factor which may be limiting the ultimate efficiency. Organic semiconductors are known to be more resistive than inorganic semiconductors and can have stability and reproducibility issues. One inorganic p-type candidate material is $ZnSe_XTe_{1-X}$, which has a tunable band structure based on the Se fraction similar to that of CST. Alternatively, the use of dopants in the organic semiconductor may allow for greater conductivity and reduce recombination at the interface. Additionally, the use of more a more transparent back contact in place of the thin Au contact may allow for less current loss due to surface reflection.

The absorber fabrication process also deserves attention in order to reduce the formation of trap states which currently limit the mobility of charges in CdSe and greatly reduce the efficiency of devices. Recent work in doping CdSe with Te ($CdSe_{0.95}Te_{0.05}$) demonstrated increased carrier lifetimes and enabled efficiencies to increase by roughly 1% [77]. By use of a device structure consisting of PEDOT:PSS/CuI/ITO in place of the PTAA/ MoO_3/Au shown here, J_{SC} of 18.8% (84% of the theoretical maximum) was shown, but a low V_{OC} of only 470 mV was achieved. This indicating that CdSe absorbers have the potential to achieve high currents, which was a problem presented in this work, but there may be a trade-off between J_{SC} and V_{OC} which needs to be further explored. This is particularly important for the development of tandem devices, where the tandem module J_{SC} is limited by the top cell and the V_{OC} is the sum of the top and bottom cell.

Bibliography

[1] Xin Lan, Pieter Tans, Kirk Thoning, and NOAA Global Monitoring Laboratory. Trends in globally-averaged CO_2 determined from NOAA global monitoring laboratory measurements, 2023.

[2] NASA. Measuring global temperature. https://science.nasa.gov/earth/measuring_global_temperature/, 2025.

[3] U.S. Energy Information Administration. Annual energy outlook 2025, 2025.

[4] National Renewable Energy Laboratory. Best Research-Cell Efficiency Chart. https://www.nrel.gov/pv/cell-efficiency.html, May 2025.

[5] John Y. W. Seto. The electrical properties of polycrystalline silicon films. *Journal of Applied Physics*, pages 5247–5254, 1975.

[6] C. H. Swartz, M. Edirisooriya, E. G. LeBlanc, O. C. Noriega, P. A. R. D. Jayathilaka, O. S. Ogedengbe, B. L. Hancock, M. Holtz, T. H. Myers, and K. N. Zaunbrecher. Radiative and interfacial recombination in CdTe heterostructures. *Applied Physics Letters*, page 222107, 2014.

[7] W. Shockley and H. J. Queisser. Detailed Balance Limit of Efficiency of P-n Junction Solar Cells. *J. Appl. Phys.*, page 510, 1961.

[8] Elisa Artegiani, Mauro Leoncini, Marco Barbato, Matteo Meneghini, Gaudenzio Meneghesso, Marco Cavallini, and Alessandro Romeo. Analysis of magnesium zinc oxide layers for high efficiency CdTe devices. *Thin Solid Films*, pages 22–25, 2019.

[9] Amit H. Munshi, Jason M. Kephart, Ali Abbas, Tushar M. Shimpi, Kurt L. Barth, John M. Walls, and Walajabad S. Sampath. Polycrystalline CdTe photovoltaics with efficiency over 18% through improved absorber passivation and current collection. *Solar Energy Materials and Solar Cells*, pages 9–18, 2018.

[10] Francesco Bittau, Christos Potamialis, Mustafa Togay, Ali Abbas, Patrick J.M. Isherwood, Jake W. Bowers, and John M. Walls. Analysis and optimisation of the glass/TCO/MZO stack for thin film CdTe solar cells. *Solar Energy Materials and Solar Cells*, pages 15–22, 2018.

[11] Graham Lane Maxwell. Characterization and modeling of $CdCl_2$ treated CdTe/CdS thin-film solar cells. Master's thesis, Colorado State University, 2010.

[12] Amit H. Munshi, Jason M. Kephart, Ali Abbas, Adam Danielson, Guillaume Gelinas, Jean-Nicolas Beaudry, Kurt L. Barth, John M. Walls, and Walajabad S. Sampath. Effect of $CdCl_2$ passivation treatment on microstructure and performance of CdSeTe/CdTe thin-film photovoltaic devices. *Solar Energy Materials and Solar Cells*, pages 259–265, 2018.

[13] S.H. Demtsu and J.R. Sites. Effect of back-contact barrier on thin-film CdTe solar cells. *Thin Solid Films*, pages 320–324, 2006.

[14] J. Perrenoud, L. Kranz, C. Gretener, F. Pianezzi, S. Nishiwaki, S. Buecheler, and A. N. Tiwari. A comprehensive picture of Cu doping in CdTe solar cells. *Journal of Applied Physics*, page 174505, 2013.

[15] Akira Nagaoka, Santosh K. Swain, and Amit H. Munshi. Review on Group-V Doping in CdTe for Photovoltaic Application. *IEEE Journal of Photovoltaics*, pages 1–17, 2024.

[16] E Colegrove, J-H Yang, S P Harvey, M R Young, J M Burst, J N Duenow, D S Albin, S-H Wei, and W K Metzger. Experimental and theoretical comparison of Sb, As, and P diffusion mechanisms and doping in CdTe. *Journal of Physics D: Applied Physics*, page 075102, 2018.

[17] Dmitry Krasikov, Da Guo, Samuel Demtsu, and Igor Sankin. Comparative study of As and Cu doping stability in CdSeTe absorbers. *Solar Energy Materials and Solar Cells*, page 111012, 2021.

[18] Tursun Ablekim, Santosh K. Swain, Wan-Jian Yin, Katherine Zaunbrecher, James Burst, Teresa M. Barnes, Darius Kuciauskas, Su-Huai Wei, and Kelvin G. Lynn. Self-compensation in arsenic doping of CdTe. *Scientific Reports*, pages 45–63, 2017.

[19] Intuon Chatratin, Baoying Dou, Su-Huai Wei, and Anderson Janotti. Doping Limits of Phosphorus, Arsenic, and Antimony in CdTe. *The Journal of Physical Chemistry Letters*, pages 273–278, 2023.

[20] A. T. Mathew, H. Lott, E. Colegrove, M. R. Young, D. Kuciauskas, C. A. Wolden, and M. O. Reese. Arsenic activation and compensation in single crystal CdTe bilayers. *Journal of Applied Physics*, page 115702, 2025.

[21] G. Kartopu, O. Oklobia, D. Turkay, D. R. Diercks, B. P. Gorman, V. Barrioz, S. Campbell, J. D. Major, M. K. Al Turkestani, S. Yerci, T. M. Barnes, N. S. Beattie, G. Zoppi, S. Jones, and S. J. C. Irvine. Study of thin film poly-crystalline CdTe solar cells presenting high acceptor concentrations achieved by in-situ arsenic doping. *Solar Energy Materials and Solar Cells*, pages 259–267, 2019.

[22] Deng-Bing Li, Canglang Yao, S. N. Vijayaraghavan, Rasha A. Awni, Kamala K. Subedi, Randy J. Ellingson, Lin Li, Yanfa Yan, and Feng Yan. Low-temperature and effective ex situ group V doping for efficient polycrystalline CdSeTe solar cells. *Nature Energy*, pages 715–722, 2021.

[23] V. Sa-Yakanit and H. R. Glyde. Urbach Tails and Disorder. *Comments Condens. Matter Phys.*, page 35, 1987.

[24] J. Chantana, Y. Kawano, T. Nishimura, A. Mavlonov, and T. Minemoto. Impact of Urbach Energy on Open-Circuit Voltage Deficit of Thin-Film Solar Cells. *Sol. Energy Mater. Sol. Cells*, page 110502, 2020.

[25] Joeson Wong, Stefan T. Omelchenko, and Harry A. Atwater. Impact of Semiconductor Band Tails and Band Filling on Photovoltaic Efficiency Limits. *ACS Energy Letters*, pages 52–57, 2021.

[26] M. A. Hernández-Fenollosa, D. P. Halliday, K. Durose, M. D. Campo, and J. Beier. Photoluminescence studies of CdS/CdTe solar cells treated with oxygen. *Thin Solid Films*, pages 176–180, 2003.

[27] H. Zhao, Alvi Farah, D. Morel, and C.S. Ferekides. The effect of impurities on the doping and V_{OC} of CdTe/CdS thin film solar cells. *Thin Solid Films*, pages 2365–2369, 2009.

[28] Craig L. Perkins, Brian McCandless, Deborah L. McGott, Matthew O. Reese, and Wyatt Metzger. Oxidative segregation of Group V dopants in CdTe solar cells. In *2019 IEEE 46th Photovoltaic Specialists Conference (PVSC)*, pages 0169–0172, 2019.

[29] James F. Ziegler, M. D. Ziegler, and J. P. Biersack. SRIM – The stopping and range of ions in matter (2010). *Nuclear Instruments and Methods in Physics Research Section B: Beam Interactions with Materials and Atoms*, pages 1818–1823, 2010.

[30] Y. Zhao, M. Boccard, S. Liu, J. Becker, X. H. Zhao, C. M. Campbell, E. Suarez, M. B. Lassise, Z. Holman, and Y. H. Zhang. Monocrystalline CdTe Solar Cells with Open-Circuit Voltage over 1 V and Efficiency of 17%. *Nat. Energy*, page 16067, 2016.

[31] Deborah L. McGott, Steven W. Johnston, Chun-Sheng Jiang, Tuo Liu, Darius Kuciauskas, Stephen Glynn, and Matthew O. Reese. Investigation of Sub-Bandgap Emission and Unexpected n-Type Behavior in Undoped Polycrystalline $CdSe_xTe_{1-x}$. *Advanced Science*, page 2309264, 2024.

[32] X. Zheng, E. Colegrove, J. N. Duenow, J. Moseley, and W. K. Metzger. Roles of bandgrading, lifetime, band alignment, and carrier concentration in high-efficiency CdSeTe solar cells. *Journal of Applied Physics*, page 053102, 2020.

[33] A. R. Bowman, J. F. Leaver, K. Frohna, S. D. Stranks, G. Tagliabue, and J. D. Major. Spatially resolved photoluminescence analysis of the role of Se in $CdSe_xTe_{1-x}$ thin films. *Nature Communications*, page 8729, 2024.

[34] Bérengère Frouin, Thomas Bidaud, Stefano Pirotta, Tursun Ablekim, John Moseley, Wyatt K. Metzger, and Stéphane Collin. Quantitative assessment of selenium diffusion and passivation in CdSeTe solar cells probed by spatially resolved cathodoluminescence. *APL Materials*, page 031135, 2024.

[35] U. Rau and J. H. Werner. Radiative Efficiency Limits of Solar Cells with Lateral Band-Gap Fluctuations. *Appl. Phys. Lett.*, page 3735, 2004.

[36] Nathan Rosenblatt, James Hack, Chungho Lee, Yong-Hang Zhang, and Wyatt K. Metzger. Impacts of band edge fluctuations on CdSeTe solar cell performance and models. *APL Materials*, page 111117, 2024.

[37] Joel N. Duenow, James M. Burst, David S. Albin, Matthew O. Reese, Søren A. Jensen, Steven W. Johnston, Darius Kuciauskas, Santosh K. Swain, Tursun Ablekim, Kelvin G. Lynn, Alan L. Fahrenbruch, and Wyatt K. Metzger. Relationship of Open-Circuit Voltage to CdTe Hole Concentration and Lifetime. *IEEE Journal of Photovoltaics*, pages 1641–1644, 2016.

[38] J. M. Burst, J. N. Duenow, D. S. Albin, E. Colegrove, M. O. Reese, J. A. Aguiar, C.-S. Jiang, M. K. Patel, M. M. Al-Jassim, D. Kuciauskas, S. Swain, T. Ablekim, K. G. Lynn, and W. K. Metzger. CdTe solar cells with open-circuit voltage breaking the 1 V barrier. *Nature Energy*, pages 1–8, 2016.

[39] Akira Nagaoka, Kensuke Nishioka, Kenji Yoshino, Darius Kuciauskas, and Michael A. Scarpulla. Arsenic doped Cd-rich CdTe: Equilibrium doping limit and long lifetime for high open-circuit voltage solar cells greater than 900 mV. *Applied Physics Express*, page 081002, 2019.

[40] Darius Kuciauskas, Marco Nardone, Alexandra Bothwell, David Albin, Carey Reich, Chungho Lee, and Eric Colegrove. Why Increased CdSeTe Charge Carrier Lifetimes and Radiative Efficiencies did not Result in Voltage Boost for CdTe Solar Cells. *Advanced Energy Materials*, page 2301784, 2023.

[41] Deborah L. McGott, Brian Good, Brian Fluegel, Joel N. Duenow, Colin A. Wolden, and Matthew O. Reese. Carrier lifetime as a function of Se content for $CdSe_xTe_{1-x}$ films grown on Al_2O_3 and MgZnO. In *2021 IEEE 48th Photovoltaic Specialists Conference (PVSC)*, pages 1301–1303, 2021.

[42] Commission of the European Communities and E. Rickus. Photovoltaic Behaviour of CdSe Thin Film Solar Cells. In W. H. Bloss and G. Grassi, editors, *Fourth E.C. Photovoltaic Solar Energy Conference*, pages 831–835. Springer Netherlands, 1982.

[43] R. R. Potter, J. R. Sites, and S. Wagner. Current-voltage response of tandem junction solar cells. *Journal of Applied Physics*, pages 5269–5272, 1982.

[44] N. G. Patel, C. J. Panchal, K. K. Makhija, P. G. Patel, and S. S. Patel. Fabrication and characterization of ZnTe/CdSe thin film solar cells. *Crystal Research and Technology*, pages 247–252, 1994.

[45] R. Mallick, X. Li, C. Reich, X. Shan, W. Zhang, T. Nagle, L. Bok, E. Bicakci, N. Rosenblatt, D. Modi, R. Farshchi, C. Lee, J. Hack, S. Grover, N. Wolf, W.K. Metzger, D. Lu, and G. Xiong. Arsenic-Doped CdSeTe Solar Cells Achieve World Record 22.3% Efficiency. *IEEE Journal of Photovoltaics*, pages 510–515, 2023.

[46] Sathyaharish Jeedigunta. *Development Of Cadmium Selenide As An Absorber Layer For Tandem Solar Cells*. PhD thesis, Department of Electrical Engineering, University of South Florida, Tampa, FL, 2004.

[47] Kanghua Li, Xuke Yang, Yue Lu, Jiayou Xue, Shuaicheng Lu, Jiajia Zheng, Chao Chen, and Jiang Tang. Fabrication and Optimization of CdSe Solar Cells for Possible Top Cell of Silicon-Based Tandem Devices. *Advanced Energy Materials*, page 2200725, 2022.

[48] Ebin Bastola, Adam B. Phillips, Abasi Abudulium, Vlad Kornienko, Zulkifl Hussain, Manoj K. Jamarkattel, Tamanna Mariam, Prabodika N. Kalurachchi, Jared Friedl, Dipendra Pokhrel, Kara B. Kile, Zhaoning Song, Yanfa Yan, Michael Walls, Randy J. Ellingson, and

Michael J. Heben. Cadmium Selenide (CdSe) as an Active Absorber Layer for Solar Cells with V_{OC} Approaching 750 mV. In *2023 IEEE 50th Photovoltaic Specialists Conference (PVSC)*, pages 1–6, 2023.

[49] W. J. Wösten. THE VAPOR PRESSURE OF CADMIUM SELENIDE. *The Journal of Physical Chemistry*, pages 1949–1951, 1961.

[50] Suman Kumari, G. Chasta, R. Sharma, N. Kumari, and M. S. Dhaka. Phase transition correlated grain growth in CdSe thin films: Annealing evolution to cadmium chloride activation. *Physica B: Condensed Matter*, page 414422, 2023.

[51] S.L. Patel, Himanshu, S. Chander, A. Purohit, M.D. Kannan, and M.S. Dhaka. Understanding the physical properties of $CdCl_2$ treated thin CdSe films for solar cell applications. *Optical Materials*, pages 42–47, 2019.

[52] Jared D. Friedl, Ramez Hosseinian Ahangharnejhad, Adam B. Phillips, and Michael J. Heben. Material Requirements for CdSe Wide Bandgap Solar Cells. In *2021 IEEE 48th Photovoltaic Specialists Conference (PVSC)*, pages 1548–1552, 2021.

[53] Laila Parvin Poly. *A Study of Cadmium Selenide Solar Cells*. PhD thesis, Department of Electrical and Computer Engineering, Iowa State University, 2022.

[54] A review on organic hole transport materials for perovskite solar cells: Structure, composition and reliability. *Materials Today*, pages 518–547, 2023.

[55] M. Kröger, S. Hamwi, J. Meyer, T. Riedl, W. Kowalsky, and A. Kahn. Role of the deep-lying electronic states of MoO_3 in the enhancement of hole-injection in organic thin films. *Applied Physics Letters*, page 123301, 2009.

[56] Hao Hou, Wenxuan Wang, Qian Kang, Jianqiu Wang, Zhihao Chen, Yafei Wang, Yong Cui, Yue Yu, Ji Zhu, Hui Yan, and Jianhui Hou. Undoped MoO_X with oxygen-rich vacancies as hole transport material for efficient indoor/outdoor organic solar cells. *Nano Energy*, page 110173, 2024.

[57] Taylor Hill, Sachit Grover, and James Sites. Widegap CdSe Solar Cells with V_{OC} >750mV. In *2023 IEEE 50th Photovoltaic Specialists Conference (PVSC)*, pages 1–6, 2023.

[58] Chathuranganie A. M. Senevirathne, Jun Tae Song, Dai Semba, Takato Saito, Kentaro Imaoka, Yuki Fujita, Telugu Bhim Raju, Pangpang Wang, Sunao Yamada, and Toshinori Matsushima. Role of Metal Oxide Interlayers in Preventing Gold Migration in Perovskite Solar Cells. *Solar RRL*, page 2400705, 2025.

[59] Sven Rühle. Tabulated values of the Shockley–Queisser limit for single junction solar cells. *Solar Energy*, pages 139–147, 2016.

[60] M. V. Kurik. Urbach rule. *physica status solidi*, pages 9–45, 1971.

[61] W. Sritrakool, V. Sa-yakanit, and H. R. Glyde. Band Tails in Disordered Systems. *Phys. Rev. B: Condens. Matter Mater. Phys.*, page 1199, 1986.

[62] S. John, C. Soukoulis, M. H. Cohen, and E. N. Economou. Theory of Electron Band Tails and the Urbach Optical-Absorption Edge. *Phys. Rev. Lett.*, page 1777, 1986.

[63] Piet Van Mieghem. Theory of band tails in heavily doped semiconductors. *Reviews of Modern Physics*, pages 755–793, 1992.

[64] Max Hilaire Wolter, Romain Carron, Enrico Avancini, Benjamin Bissig, Thomas Paul Weiss, Shiro Nishiwaki, Thomas Feurer, Stephan Buecheler, Philip Jackson, Wolfram Witte, and Susanne Siebentritt. How band tail recombination influences the open-circuit voltage of solar cells. *Progress in Photovoltaics: Research and Applications*, pages 702–712, 2022.

[65] T. D. Subha, R. Thandaiah Prabu, S. Parasuraman, and Atul Kumar. Role of Urbach energy in controlling voltage output of solar cells. *Optical and Quantum Electronics*, page 794, 2023.

[66] Arthur Onno, Carey Reich, Siming Li, Adam Danielson, William Weigand, Alexandra Bothwell, Sachit Grover, Jeff Bailey, Gang Xiong, Darius Kuciauskas, Walajabad Sampath, and

Zachary C. Holman. Understanding what limits the voltage of polycrystalline CdSeTe solar cells. *Nature Energy*, pages 400–408, 2022.

[67] Yuan Zhao, Xin-Hao Zhao, and Yong-Hang Zhang. Radiative Recombination Dominated Monocrystalline CdTe/MgCdTe Double-Heterostructures. *IEEE Journal of Photovoltaics*, pages 690–694, 2017.

[68] Uwe Rau and Thomas Kirchartz. Charge Carrier Collection and Contact Selectivity in Solar Cells. *Advanced Materials Interfaces*, page 1900252, 2019.

[69] Arthur Onno, Christopher Chen, Priyaranga Koswatta, Mathieu Boccard, and Zachary C. Holman. Passivation, conductivity, and selectivity in solar cell contacts: Concepts and simulations based on a unified partial-resistances framework. *Journal of Applied Physics*, page 183103, 2019.

[70] Susanne Siebentritt, Thomas Paul Weiss, Mohit Sood, Max Hilaire Wolter, Alberto Lomuscio, and Omar Ramirez. How photoluminescence can predict the efficiency of solar cells. *Journal of Physics: Materials*, page 042010, 2021.

[71] P. Würfel and W. Ruppel. The chemical potential of luminescent radiation. *Journal of Luminescence*, pages 925–928, 1981.

[72] Esma Ugur, Martin Ledinský, Thomas G. Allen, Jakub Holovský, Aleš Vlk, and Stefaan De Wolf. Life on the Urbach Edge. *The Journal of Physical Chemistry Letters*, pages 7702–7711, 2022.

[73] S. R. Johnson and T. Tiedje. Temperature Dependence of the Urbach Edge in GaAs. *J. Appl. Phys.*, page 5609, 1995.

[74] A. V. Subashiev, O. Semyonov, Z. Chen, and S. Luryi. Urbach Tail Studies by Luminescence Filtering in Moderately Doped Bulk InP. *Applied Physics Letters*, page 181914, 2010.

[75] T. Yamada, T. Aharen, and Y. Kanemitsu. Near-Band-Edge Optical Responses of CH3NH3PbCl3 Single Crystals: Photon Recycling of Excitonic Luminescence. *Physical Review Letters*, page 057404, 2018.

[76] M. J. S. Brasil, P. Motisuke, F. Decker, and J. R. Moro. Infrared photoluminescence at deep centres in polycrystalline CdSe layers. *Journal of Physics C: Solid State Physics*, pages 31–41, 1988.

[77] Jiayou Xue, Xuke Yang, Xiaoqing Bao, Liuchong Fu, Sen Li, Menglin Huang, Jun Wang, Haisheng Song, Shiyou Chen, Chao Chen, Kanghua Li, and Jiang Tang. Improved Carrier Lifetimes of CdSe Thin Film via Te Doping for Photovoltaic Application. *ACS Applied Materials & Interfaces*, pages 17858–17866, 2023.

[78] Chun-Sheng Jiang, Rouin Farshchi, Timothy Nagle, Dingyuan Lu, Gang Xiong, Lorelle M. Mansfield, and Matthew O. Reese. Microelectronic Structure and Doping Nonuniformity of Phosphorus-Doped CdSeTe Solar Cells. *ACS Applied Materials & Interfaces*, 2025.